Thin layer effects on horizon attributes: analysis beyond amplitude tuning, Viola carbonate reservoir, Morrison NE field, Kansas

by

Muhammed Jallow

B.S., Federal University of Technology, Akure, 2018

A THESIS

submitted in partial fulfillment of the requirements for the degree

MASTER OF SCIENCE

Department of Geology
College of Arts and Sciences

KANSAS STATE UNIVERSITY
Manhattan, Kansas

2024

Approved by:

Major Professor
Dr. Abdelmoneam Raef

Copyright

Abstract

Three-dimensional seismic reflection data has revolutionized the oil and gas industry by enabling vital insights into stratigraphy, geologic structures, and reservoir properties in sedimentary basins worldwide. However, accurately identifying prospects, delineating hydrocarbon reservoirs, and understanding their properties rely on the quality and resolution of seismic data. The increase or decrease of seismic attributes, caused by thin-layer tuning "geometrical effect" interference between adjacent reflectors of geological layers, adversely impacts the utility of seismic attributes in reservoir characterization. Thus, distinguishing seismic attribute anomalies diagnostic of petrophysical properties from geometric effects poses significant challenges and uncertainties. Traditionally, seismic data tuning correction has focused primarily on amplitude attributes, neglecting the impact on other crucial attributes, such as frequency, which reservoir geometry can also affect. This narrow scope limits the effectiveness of conventional methods in providing a holistic understanding of subsurface properties.

This study presents an effective data-driven method to isolate and remove thickness (tuning) effects on seismic horizon attributes. The proposed approach employs three distinct methods: statistical, deterministic wedge model, and machine learning, each offering unique insights into the tuning phenomenon. CO_2 sequestration/enhanced oil recovery injection can be associated with reservoir seismic time-thickness changes that affects the seismic response due to the mixing with and displacement of hydrocarbon oil, changes in subsurface reservoir pressure, and fluid composition distribution. The response of thin layer effects on seismic attributes offers enormous potential in monitoring CO_2 sequestration and enhanced oil recovery programs. The analysis of detuned seismic attributes of the Viola reservoir in Morrison NE field, reveals promising areas for future well placement. Areas characterized by structural highs, substantial

thicknesses, and persistently low amplitudes after detuning hold significant potential for hydrocarbon production.

Table of Contents

List of Figures vii
List of Tables xiii
List of Equations xiv
Acknowledgements xv
Dedication xvi
Chapter 1 - Introduction 1
1.1 Problem Statement 3
1.2 Previous Study 5
Chapter 2 - Geological Setting and Background 7
2.1 Study Area 7
2.2 Stratigraphic Setting 7
Maquoketa Shale 7
Viola Limestone 10
Simpson Formation 10
Arbuckle Group 11
2.3 Hagood's (2019) Stratigraphic Analysis 11
2.4 Seismic Resolution and Tuning 13
2.5 Seismic Attributes and Tuning 15
2.6 Machine Learning and Tuning 18
Chapter 3 - Data and Methods 20
3.1 3D Seismic Data 20
3.2 Geophysical Well Logs 21
3.3 Seismic Wavelet Extraction 21
3.4 1D Synthetic Modeling and Well-to-seismic tie 25
3.5 Seismic Attributes Extraction 25
3.6 Deterministic Wedge Model Approach 31
3.7 Deterministic and Statistical Tuning Analysis 37
3.8 Mineral Composition Profile 39
3.9 Supervised Machine Learning for Tuning Analysis 45

Gradient Boosting 47
Random Forest 49
XGBoost.. 51
Chapter 4 - Results and Discussion 53
4.1 Synthetic Wedge Models 53
4.2 Composite Amplitude Cross plots 58
4.3 Statistical and Deterministic Tuning Analysis.. 59
4.4 Mineral Composition Profiles & Victor's (2020) Ultrasonic Measurements 61
4.5 Amplitude Regression Analysis.. 66
4.6 Detuned Seismic Attributes 66
4.7 Maximum Tuning Error Prediction Using Supervised Machine Learning.................. 73
Target Label from Statistical Correction 73
Target Label from Wedge Model Approach Correction.. 76
Chapter 5 - Conclusion 81
References... 83
Appendix A - Extracted Seismic Attributes.. 87
Appendix B - RHOmaa-Umaa Cross-plots... 89
Appendix C - Synthetic wedge models... 92

List of Figures

Figure 1.1: Instantaneous Phase cross section across Stephens1 along with its synthetic. The viola limestone thickens and splits (seismic doublet) into two peaks named Viola Top (black line) and Viola C (red line) around the well. The Arbuckle (black dashed line) is a strong peak with a consistent instantaneous phase. Phase angles are represented by the color bar on the right. 4

Figure 2.1: Anadarko Basin map. The red star indicates the approximate location of the study area within Clark County, Ks. (Modified after Ball, 1991). 8

Figure 2.2: Southern Clark County map. The wells were drilled in the Morrison NE fields represented by the black circle (KGS, 2014). 8

Figure 2.3: Stratigraphic column of the study area and four distinct lithofacies within the Viola (modified after Cole, 1975). 9

Figure 2.4: Idealized cross-section (N-S) of the paleotopographic traps in the Viola limestone (modified after Richardson 2013). 9

Figure 2.5: The "B" Zone highlighted in blue along the depth track is where slower Vp velocities and higher neutron porosity values are present, corresponding with the cherty Dolomite. A, B, and C zones are highlighted in green, blue, and red. The green highlighting along the right log track depicts porosity above 15% (Hagood et al., 2019). 12

Figure 2.6: Cored section of cherty Dolomite in the Viola Ls. from Rich C #7 at depths 5818.5' (left) and 5822' (right). Dolomite (Dol) can be seen replacing the Chert (Chrt) (Hagood et al., 2019). 12

Figure 2.7: Thin section photomicrographs of cherty Dolomite. A) plain polarized light (PPL) and B) cross polarized light (XPL) image at 5818.5'. C) PPL and D) XPL image at 5818.5' displaying hydrocarbons (HC) inside the porosity of siliceous grains. E) PPL and F) XPL image at 5822' displaying the replacement of chert (Chrt) with Dolomite (Dol) (Hagood et al., 2019). 13

Figure 2.8: Seismic data for approximately the same location. (A) 2D conventional seismic line from 1985, (B) seismic line in the 3D high-resolution (P-Cable) cube from 2014 (modified after Faleide et al., 2019). 14

Figure 2.9: Instantaneous Phase and Instantaneous Frequency in 3D view. 17

Figure 3.1: Stephens Ranch 3D seismic volume in a 3D view. 20
Figure 3.2: Frequency wavelet extraction process with an extraction time range of 69ms to 118ms around 10 seismic traces.................. 22
Figure 3.3: Extracted wavelets for Hardens1, Stephens1, and Stephens3 23
Figure 3.4: Extracted wavelets for Stephens4, Stephens5, and Stephens7. 24
Figure 3.5: The seismic well tie (A) shows the Viola peak reflector (black arrow), Simpson trough reflector (red arrow), Arbuckle peak reflector (green arrow), and a Synthetic (B) 1-D trace model obtained from Stephens1. 26
Figure 3.6: Amplitude map (a) of the Viola Limestone top. Amplitude values are represented by the color bar on the left. 27
Figure 3.7: Reflectivity Strength (b) of the Viola Limestone top. Reflectivity Strength values are represented by the color bar on the left. 28
Figure 3.8: Instantaneous Frequency (c) of the Viola Limestone top. Instantaneous Frequency values are represented by the color bar on the left. 29
Figure 3.9: Instantaneous Phase (d) of the Viola Limestone top. Phase angles are represented by the color bar on the left. 30
Figure 3.10: (a) A three-layer wedge model. (b) The constructive interference between the side lobes and main reflections produces brighter reflections, as seen in the zero-offset synthetic seismogram displayed in normal polarity. (c) The amplitude of the synthetic extracted along the top of the Viola reservoir. (d)The convolved Ricker wavelet of 38.5Hz. 32
Figure 3.11: Deterministic tuning curve (a) of Hardens1 and the extracted wavelet (b) from the seismic around the well used for modeling. 33
Figure 3.12: Deterministic tuning curve (c) of Hardens1 and the extracted average wavelet (d) from the seismic used for modeling. 33
Figure 3.13: Shows the amplitude response (green stars) obtained from the wedge models rescaled to match the composite amplitude (red dots) scales of the seismic amplitude horizon. 34
Figure 3.14: Shows the amplitudes (blue) and the interpolated amplitudes (orange) values for Hardens1. 36
Figure 3.15: Shows the thicknesses and the interpolated thickness values for Hardens1. 36

Figure 3.16: Cross-plot of the base amplitudes of the Viola Limestone against its top amplitudes demonstrating approximate proportionality. 38

Figure 3.17: Cross-plot of the composite amplitude of the seismic horizons against the Isochrone thickness (ms) colored by the instantaneous frequency. 38

Figure 3.18: RHOmaa-Umaa chart shows the basic plan of the crossplot found in logging service company chartbooks. 41

Figure 3.19: Cross-plot of RHOmaa-Umaa values for Stephens8 (S8) colored by the density(a) and the reservoir depth (b) interval. The shallow part (green arrow) of the Viola reservoir for S8 consist majorly of Cherty dolomite (Quartz & Dolomite) while the deeper part (black arrow) consists mainly of Limestone (Calcite). 43

Figure 3.20: Mineral composition profile for Stephens8 (S8) at the reservoir depth interval of interest. The black dashed line is the sonic log, which shows how velocity varies with lithology. 43

Figure 3.21: Supervised machine learning workflow for maximum tuning error prediction. 46

Figure 3.22: Gradient boosted trees for regression (geeksforgeeks.org) 48

Figure 3.23: Random Forest regression architecture (geeksforgeeks.org). 50

Figure 3.24: General structure of XGBoost (Kalyani et al., 2019). 51

Figure 4.1: Wedge models show the change in seismic response of the amplitude (a) and instantaneous phase (b) at or below tuning, indicated by the vertical dashed lines. The time thickness (c) ranges from 0.5ms to about 28ms. The increase (red arrow), decrease (green arrow) of the seismic response and the Viola top (black arrow) are highlighted. 54

Figure 4.2: Wedge models show the change in seismic response of the amplitude envelope (a) and instantaneous frequency (b) at or below tuning, indicated by the vertical dashed lines. The time thickness (c) ranges from 0.5ms to about 28ms. The increase (red arrow), decrease (green arrow) of the seismic response and the Viola top (black arrow) are highlighted. 55

Figure 4.3: Wedge models for Stephens4 (A) and Stephens5 (B) and their corresponding amplitudes extracted from the viola top in a 20ms window. The isochron displays the time thickness (ms). Peaks (red arrows) and trough (black arrow) are highlighted. 56

Figure 4.4: Deterministic tuning points for Stephens3 (a) and Stephens7 (b). The peaks (P1 & P2), trough (T), tuning baseline (TB), and the actual thickness (AT) of the reservoir were extracted for all the wells. 57

Figure 4.5: A cross-plot of the composite amplitude of the seismic horizons vs. thickness (ms) colored by the instantaneous frequency attribute. (b) Extracted wavelet from the seismic.. 58

Figure 4.6: Deterministic tuning curve modeled with the average wavelet extracted from the seismic. Shows the underestimation (black arrow) and overestimation (blue arrow) of thickness beyond tuning. The amplitude abruptly deviates from the baseline (green arrow) with tuning. 59

Figure 4.7: Composite amplitude cross plot showing wells (H1, S1, S3, S4, S5, S7 & S8) with fitted trends on the global set (green trend), untuned sets (black trend), and statistical curve enveloping the tuned sets (blue curve). 60

Figure 4.8: Mineral composition profile for well S1, S3, and S4 at the reservoir depth interval. The normalized sonic log (black dashed line) shows the velocity response with changing mineralogy (lithology). 63

Figure 4.9: Mineral composition profile for well S5, S7, and S8 at the reservoir depth interval. The normalized sonic log (black dashed line) shows the velocity response with changing mineralogy (lithology). 64

Figure 4.10: P-wave velocities are taken at sonic frequencies (wireline logging) and ultrasonic frequencies (Lab compression testing) in the Rich C-7 well and core. The blue box marks the Cherty Dolomite section, and the red one, the Muddy Dolomitic section (Victor et.al, 2020). 65

Figure 4.11: Density (DPHI) and neutron (NPHI) porosity logs compared to P-wave velocities from ultrasonic measurements obtained in the Rich C-7 Core (Victor et.al, 2020). 65

Figure 4.12: Regression analysis of the compensated neutron porosity against the original (a) and detuned (b) seismic amplitude. 67

Figure 4.13: Shows the original and corrected seismic attributes from the statistical method. Producing wells (black arrows), nonproducing wells (red arrows) and potential drilling zones (green arrows) are highlighted. 69

Figure 4.14: Well locations superimposed on the time structural map (a), detuned composite amplitude map (b), Original isochrone map (c), and Detuned isochrone map (d) highlighting the correlation between structural highs, high thicknesses, and well locations originally targeted for drilling. Producing wells (black arrows), nonproducing wells (red arrows) and potential drilling zones (green arrows) are highlighted. 70

Figure 4.15: Shows the original (a) and corrected seismic amplitude (b) from the deterministic wedge model approach. The maximum tuning error map (c) highlights the amplitude change. 71
Figure 4.16: Summary of the amplitude and instantaneous frequency responses for the Viola Limestone. Red arrow and blue arrow represent increase and decrease respectively. 72
Figure 4.17: Shows the maximum tuning error map of the statistical method (a) the deterministic wedge model method (b)........ 72
Figure 4.18: Displays the convergence behavior of the models, showcasing how MSE evolves across iterations for training and testing datasets (a & c). crossplots of the target labels (original maximum tuning error) against the predicted maximum tuning error (b & d) visualize the performance of the machine learning algorithms in predicting tuning errors. 74
Figure 4.19: Cross-plot of the target labels (original maximum tuning error) against the predicted maximum tuning error visualizes the performance of the Random Forest model in predicting tuning errors. 75
Figure 4.20: Displays the convergence behavior of the models, showcasing how MSE evolves across iterations for training and testing datasets (a & c). crossplots of the target labels (original maximum tuning error) against the predicted maximum tuning error (b & d) visualize the performance of the machine learning algorithms in predicting tuning errors. 77
Figure 4.21: Cross-plot of the target labels (original maximum tuning error) against the predicted maximum tuning error visualizes the performance of the Random Forest model in predicting tuning errors. 78
Figure 4.22: Feature importance score (a) and the Spearman correlation (b) between input features from the statistical correction approach. 79
Figure 4.23: Feature importance score (a) and the Spearman correlation (b) between input features from the wedge model correction approach. 80

Figure A. 1: Instantaneous phase attribute as an indicator of lateral continuity. It highlights detailed visualization of stratigraphic elements as consistent and continuous events (red arrows). The black arrow shows the Viola peak, and the phase angles are represented by the color bar to the right. 87

Figure A. 2: Instantaneous frequency as a thin bed indicator. It highlights locations (onset of tuning) where instantaneous frequencies jump or exhibit a negative sign caused by closely-arriving reflected wavelets (red arrows). The black arrow shows the Viola peak, and the frequency values are represented by the color bar to the right. 88

Figure B. 1: RHOmaa-Umaa cross-plot of Hardens1. 89
Figure B. 2: RHOmaa-Umaa cross-plot of Stephens1. 89
Figure B. 3: RHOmaa-Umaa cross-plot of Stephens3. 90
Figure B. 4: RHOmaa-Umaa cross-plot of Stephens4. 90
Figure B. 5: RHOmaa-Umaa cross-plot of Stephens5. 91
Figure B. 6: RHOmaa-Umaa cross-plot of Stephens7. 91

Figure C. 1: Wedge model configuration. Wells are duplicated to keep geology (velocity and density) constant while the thickness of the viola is varied. 92
Figure C. 2: (a) A three-layer wedge model. (b) The constructive interference between the side lobes and main reflections produces brighter reflections, as seen in the zero-offset synthetic seismogram displayed in normal polarity. (c) The amplitude of the synthetic extracted along the top of the Viola reservoir. (d)The convolved Ricker wavelet of 25Hz.

List of Tables

Table 3.1: RHOmaa and Umaa values for the three minerals as a coefficient matrix "C"........... 43
Table 3.2: Matrix multiplication between well log (RHOmaa &Umaa) and inverse matrix........ 43
Table 3.3: Mineral Proportion... 43

List of Equations

Equation 3.1: Relationship between horizon amplitude and normalized peak-trough amplitude. 35
Equation 3.2: Maximum amplitude tuning thickness 37
Equation 3.3: Volume of porosity..... 40
Equation 3.4: Bulk photoelectric absorption (U)..... 40
Equation 3.5: Bulk photoelectric absorption of mineral matrix (Umaa) 40
Equation 3.6: Density of the mineral matrix (RHOmaa)..... 40
Equation 3.7: Mineral composition profile equation (Python code)..... 42
Equation 3.8: Gradient boosting algorithm..... 47
Equation 3.9: Random Forest equation for averaging predictions of individual trees 49
Equation 3.10: XGBoost Objective function..... 52

Acknowledgements

I express my deepest gratitude to Dr. Abdelmoneam Raef, my thesis advisor, for his invaluable guidance, support, and expertise throughout this research. Your mentorship has been instrumental in shaping this work.

I am also immensely grateful to Dr. Brice LaCroix and Dr. Behzad Ghanbarian, members of my supervisory committee, for their insightful feedback, encouragement, and constructive criticism, which have enriched the quality of this thesis.

Special thanks to my esteemed course instructors, Dr. Claudia Adam and Dr. Karin Goldberg, for their dedication to teaching and profound impact on my academic journey.

I extend my heartfelt appreciation to Kansas State University for providing me with an enriching academic environment and countless opportunities for growth and learning.

I also acknowledge the Department of Geology, the K-State Graduate School, and the Society of Exploration Geophysicists for their generous financial support throughout my graduate school journey.

Lastly, I am grateful to all my friends, family, and colleagues who have supported me emotionally and intellectually throughout this academic endeavor. Your encouragement and understanding have been invaluable to me.

Dedication

To my mother, who gave me everything.

Chapter 1 - Introduction

The contribution of 3D seismic data to the oil and gas industry revolution cannot be overemphasized. Seismology is the best geophysical tool utilized in imaging the subsurface as it provides crucial insights and close representation of subsurface's stratigraphy, geologic structure, and sedimentology. However, to accurately delineate hydrocarbon reservoirs and understand their properties, the quality and resolution of the seismic data is of high importance. There are physical limitations on how resolution can be improved because the earth attenuates seismic signals in proportion to the number of wavelengths in the path, making it challenging to increase resolution (Schoenberger & Levin, 1978).

Seismic data processing techniques such as deconvolution and migration try to address the vertical and horizontal resolution issues but have limitations. Vertical resolution is crucial in reservoir characterization as it impacts seismic data interpretation by masking closely spaced geologic events. There is a limit to how close two reflections, one from the top and one from the bottom of a thin layer, can be without being separated. This limit depends on the bed thickness and causes tunning effects. In seismic data, tuning is a common occurrence associated with thin beds (thickness less than a wavelength) (Ralph & Neil, 1995). The brightening or dimming of seismic attributes because of constructive and destructive interference from closely spaced reflectors must be recognized to determine reservoir boundaries reliably and fidelity of amplitude in relation to reservoir properties.

This study focuses on applying tuning analysis to the Viola limestone, which is the producing formation in the Morrison NE field. The Viola limestone reservoir exhibits significant thickness variations due to the impact of differential past geological processes of weathering and erosion surface forming the upper boundary of this reservoir, making its seismic response susceptible to tuning effects. Understanding and mitigating these tuning effects is crucial for accurate reservoir characterization and reliable reservoir interpretation. The Viola limestone hydrocarbon traps occurs due to erosional paleotopographic relief, as reported by (Richardson, 2013), where dolomite facies were preserved. Herd field development demonstrated that selective preservation of dolomite porosity beneath an erosional unconformity underlying the Maquoketa Shale controlled the Viola production (Richardson, 2013). Thus, tuning analysis can drastically improve the interpretation workflows of the Morrison NE field. Tuning analysis helps recognize and distinguish between areas where seismic attribute anomalies are diagnostic of reservoir properties or geometric effects. Clear images of stratigraphic features that may not be visible using conventional attributes can be achieved by detuning.

Seismic attribute analysis can help identify good hydrocarbon reservoir properties such as structures, stratigraphic control, lithofacies, and porosity by extracting seismic attributes like relative acoustic impedance, root mean squared (RMS) amplitude, average energy, and attenuation. Instantaneous frequency and thin bed indicator can be used to indicate layer thickness. An interpreter can determine where strata are thickening or thinning by animating through a series of frequencies along an interpreted horizon (Chopra & Marfurt, 2008).

This study aims to evaluate the application of a robust, effective, data-driven, horizon-focused method for recognizing and removing tuning effects in seismic attributes. Composite seismic attributes were utilized to enhance reservoir-related properties at the expense of the embedding material (Brown, 1999). A data-driven approach that splits composite seismic attributes into three sets based on variability and regression was used to establish variability trends: statistical tuning, calibrating, and global variability trends. Linear trends were fitted to untuned and global sets, and a baseline trend was established to determine tuning error.

Additionally, this study explores the potential of machine learning techniques to automate the identification and removal of tuning effects on seismic attributes. This study revealed that Viola's decrease of instantaneous frequency values, associated with lower seismic amplitudes, indicates prolific hydrocarbon saturations. The data-driven method showed that anomalies were initially masked by tuning, giving rise to uncertainties.

1.1 Problem Statement

The Viola limestone reservoir of the Morrison NE field, Clark County, Kansas, exhibits high reservoir heterogeneities due to variable dolomitization. The reservoir thickness variation (Fig. 1.1) causes ambiguous seismic attribute anomalies. Since hydrocarbon exists and the target lithologies have thin beds, the tuning effect can lead to high, bright, or dim amplitudes, depending on the reservoir thickness, which can be confused with direct hydrocarbon indicators (DHI). Identifying and removing these effects is vital in accurately characterizing such reservoirs.

This research aims to evaluate the application of a robust, effective, data-driven horizon-focused method and machine learning techniques in recognizing and removing tuning effects in seismic attributes. Since the seismic response to tuning is ambiguous, the following objectives will be considered:

1) Utilize a simple wedge model case (pinch-out) to model tuning effects at well locations and predict time thickness and detuning.
2) Identify seismic attributes that are responsive to tuning effects and observe their uniformity.
3) Study the variation of the seismic attributes for producers and dry holes and how they vary with thickness.

Well: Stephens1

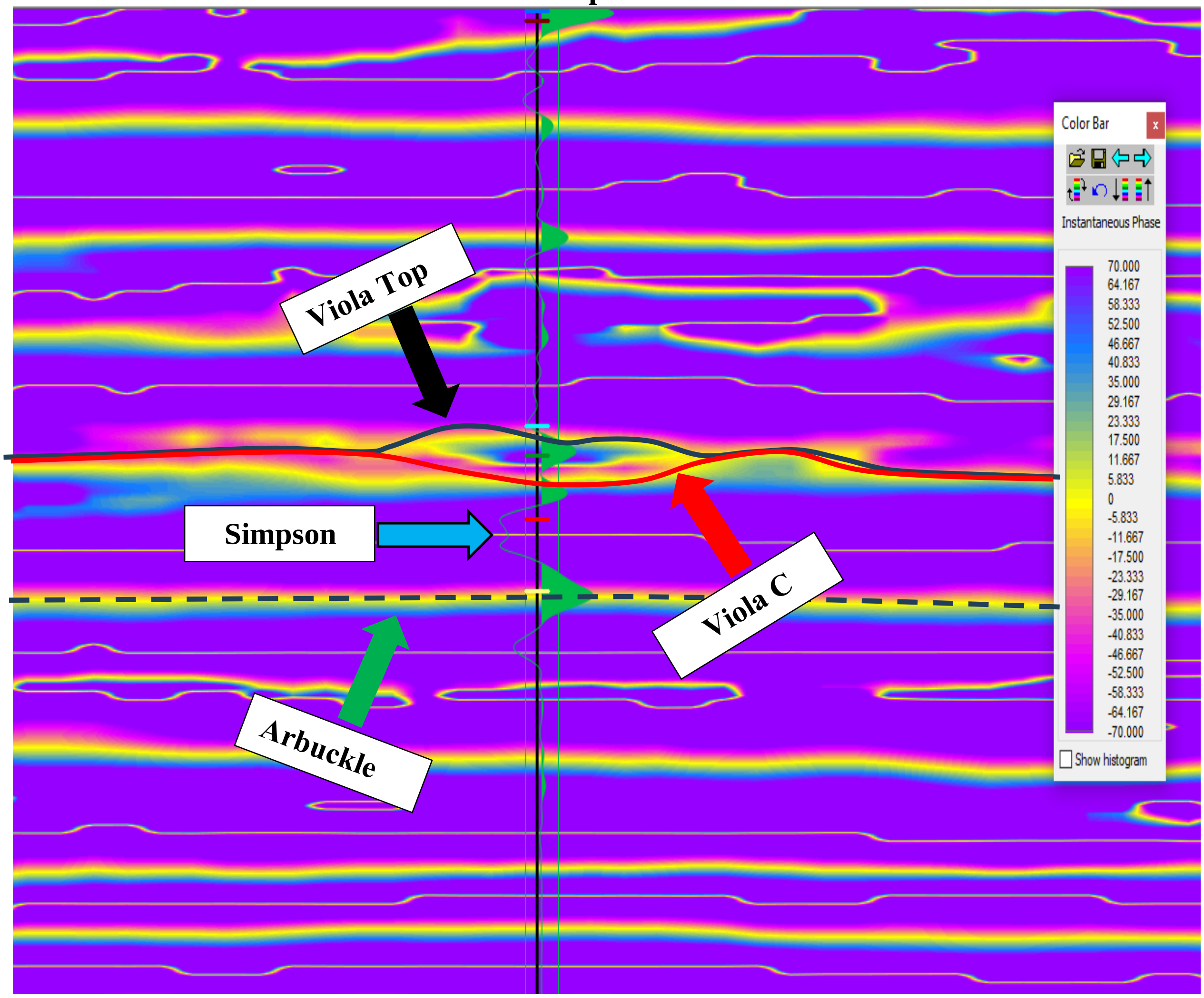

Figure 1.1: Instantaneous Phase cross section across Stephens1 along with its synthetic. The viola limestone thickens and splits (seismic doublet) into two peaks named Viola Top (black line) and Viola C (red line) around the well. The Arbuckle (black dashed line) is a strong peak with a consistent instantaneous phase. Phase angles are represented by the color bar on the right.

4) Identify potential zones for hydrocarbon production after the detuning of horizons.
5) Build machine learning models that can recognize tuning effects by predicting the waveform of a given seismic wavelet at different well locations.

1.2 Previous Study

Bornemann and Doveton (1983), conducted a comprehensive study on the lithofacies variation within the Viola Limestone in south-central Kansas, integrating core and cuttings studies with numerical analyses of wireline logs. Their analysis identified two primary lithofacies: a low-porosity limestone composed of crinoidal packstones and grainstones, and a moderately porous cherty dolomitic limestone representing dolomitized wackestones and mudstones. The study highlights the significance of fault trends associated with the Precambrian Central North American Rift System, which influenced Paleozoic depositional trends, diagenetic patterns, erosional history, and the localization of Viola oil field traps.

Raef et al. (2019) Integrated petrophysical and petrographic methods to better predict reservoir conditions in the Viola limestone due to the difficulties in understanding the reservoir-quality controls. The study established the primary reservoir quality control as dolomitization-induced porosity. The dolomitization controls were supported by comparing typical model trends for limestone and dolomite density-porosity with best-fit trends on well log values. In addition, the study presented an unsupervised ANN classification based on five seismic attributes consistent with the Ca–Mg ratio and the observed variation in sonic transit time (DT log) with porosity increase.

The viability of seismic attributes in characterizing the Viola reservoir facies was investigated by integrating ultrasonic laboratory data, well-logs, and fluid replacement modeling (Victor et.al, 2020). Ultrasonic rock physics measurements were utilized to determine core elastic properties and their relation to in situ values from well logs. Ultrasonic Poisson's ratio, bulk modulus, P-wave velocity, and shear modulus provide the same trend as sonic and density log variation in response to changes in lithofacies and porosity. Also, higher porosity correlated with higher chert, while lower porosity was associated with higher Calcite, confirming changes in lithology.

Chapter 2 - Geological Setting and Background

2.1 Study Area

The research area is in the Hugoton embayment of Kansas, an extension of the Anadarko basin (Fig. 2.1). This embayment is surrounded by elevated regions to the west by the Sierra Grande Arch, north by the Central Kansas Uplift, and east by the Pratt Anticline (Ball et al., 1991). The 3D seismic survey was conducted in Clark County, KS, in the state's southwest region, which led to the drilling of twelve wells in the Morrison Northeast field and Morrison field.

2.2 Stratigraphic Setting

The formations of interest within the Morrison NE field include the Maquoketa shale, Viola limestone, Simpson groups, and the Arbuckle group. The Middle Ordovician Viola limestone is the reservoir of interest bounded above and below by the Upper Ordovician Maquoketa shale and Middle Ordovician Simpson group, respectively. The Arbuckle creates a seismic signature that is easy to identify and helps map the relevant horizons. A stratigraphic column of the study area is displayed in Figure 2.3 below.

Maquoketa Shale

The Maquoketa shale is difficult to map but is an integral unit for the Morrison NE field**.** The Maquoketa is a dense shale in the study area ranging from cream to light grey, and it has no visible pores and an average thickness of about 20 to 25 feet. The Maquoketa thickens in the lows and thins over Viola's paleotopographic highs. According to (Richardson, 2013), the region's petroleum system is well protected by this dense, non-porous rock which acts as a seal.

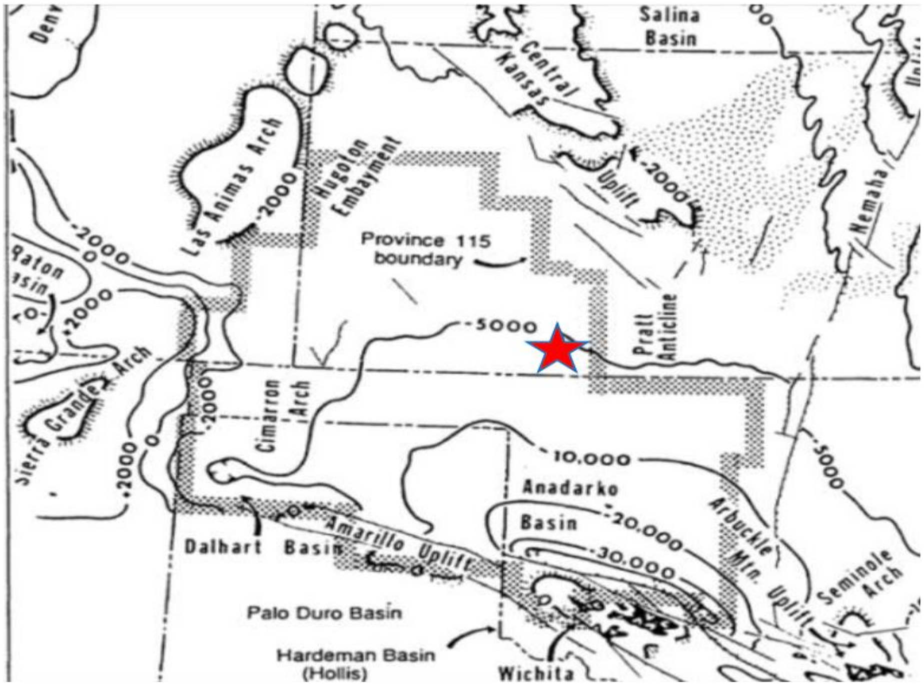

Figure 2.1: Anadarko Basin map. The red star indicates the approximate location of the study area within Clark County, Ks. (Modified after Ball, 1991).

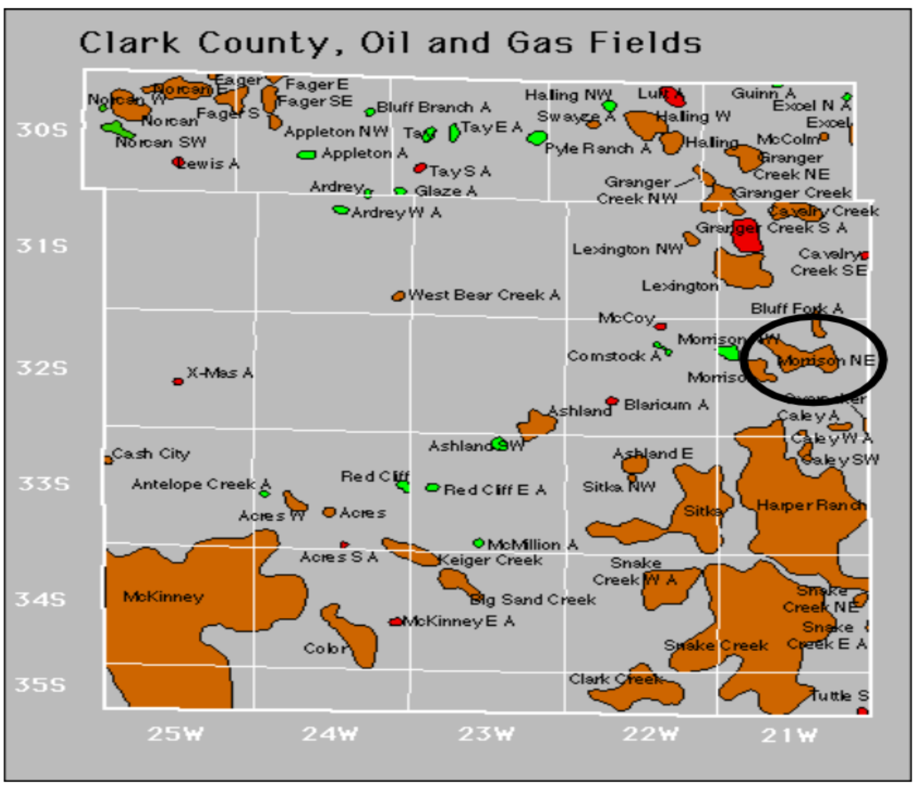

Figure 2.2: Southern Clark County map. The wells were drilled in the Morrison NE fields represented by the black circle (KGS, 2014).

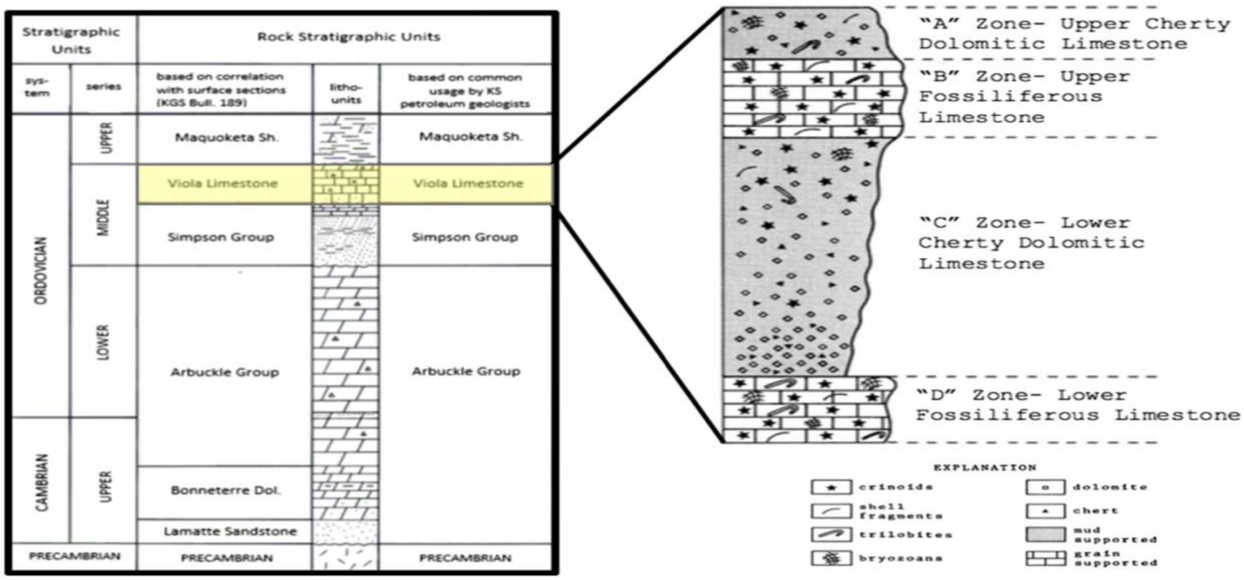

Figure 2.3: Stratigraphic column of the study area and four distinct lithofacies within the Viola (modified after Cole, 1975).

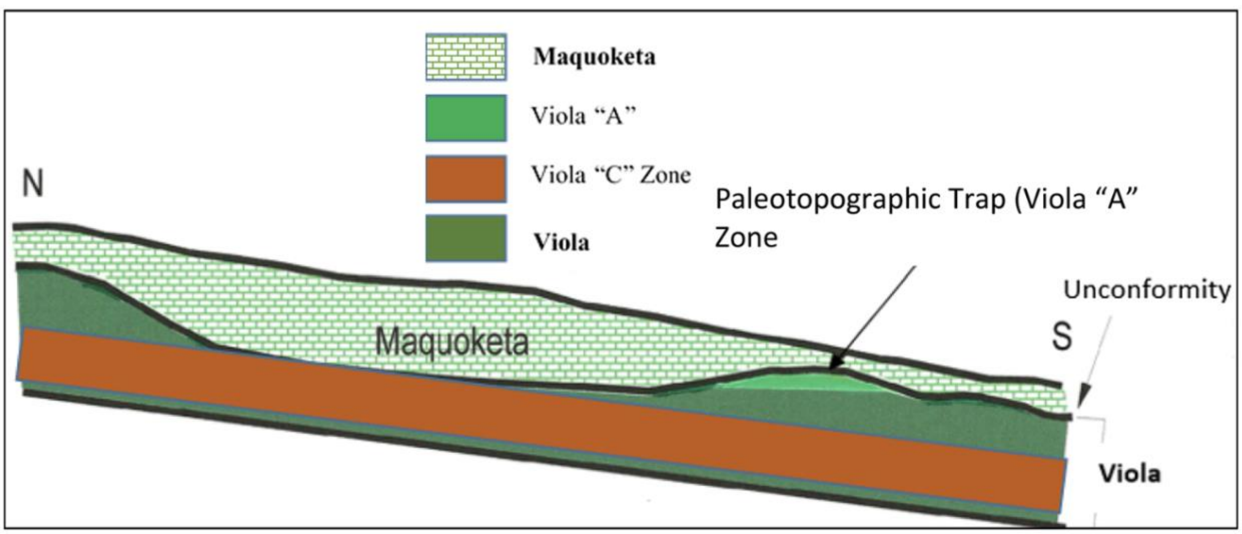

Figure 2.4: Idealized cross-section (N-S) of the paleotopographic traps in the Viola limestone (modified after Richardson 2013).

Viola Limestone

The Viola limestone is the reservoir of interest in the study area and consists of limestone, Dolomite, and chert. The Viola limestone was deposited in a warm tropical marine setting in the middle Ordovician period. The Viola varies between a fossiliferous limestone and a medium to coarse crystalline vuggy Dolomite, often containing scattered chert, with a total thickness of about 175–200 ft within the study area (Raef et al., 2019). Several erosion periods have reduced the formation's original thickness and areal extent. The Viola is separated from the overlying Maquoketa/Kinderhook section by an erosional unconformity representing about 20 Ma of no deposition and subaerial exposure, contributing to the formation of vugs that give the Viola its excellent permeability and porosity. Subaerial exposure is also responsible for generating the paleogeographic highs and lows within the Viola. This erosional unconformity produced a model of a paleotopographic trap within the Viola, as shown in Figure 2.4 above (Richardson, 2013).

Simpson Formation

The bottom of the Viola limestone is marked by the Middle Ordovician Simpson formation, which comprises three parts: the top is made of shale and limestone, the base is made of upper Simpson sand, and the top is made of lower Simpson sand. Between the two shale deposits that make up the Simpson Formation's top layer is a soft, chalky fossiliferous limestone with little porosity. The upper Simpson sand, composed of a fine-grained, poorly sorted, sub-rounded sandstone consisting primarily of Quartz with numerous shale inclusions, lies beneath this top portion. The upper sand also has a thick (60 feet) shale layer that is like what is found in the top part of the Simpson Formation.

Arbuckle Group

The Arbuckle group is of Cambrian-Ordovician age and exists only in the subsurface in Kansas (Franseen et al., 2004). The rocks that make up the Arbuckle Group are Dolomite, sandstone, and sandy or cherty Dolomite, and all these rocks may have excellent permeability and porosity. The Arbuckle Group consists almost entirely of shale, except for the shaly Simpson beds at the section's top (Cole, 1975). The Arbuckle creates a seismic signature that is easy to identify and helps map the relevant horizons of interest within the study area.

2.3 Hagood's (2019) Stratigraphic Analysis

Hagood (2019) Conducted a high-resolution facies study of the Viola "B" Zone using the Rich C-7 well of the Herd field in Comanche County, Kansas. This study identified five distinct facies: Cherty Dolomite, Intra-clastic Breccia, Intra-clastic Rudstone, Bioclastic Grainstone, and Muddy Dolostone (Fig. 2.5). The B Zone's productivity is linked to the high-porosity Cherty Dolomite, which is white to light gray chert with sponge spicules, laminations, and moderate bioturbation. It transitions upward to Rudstone with interbedded Breccia and Muddy Dolostone before transitioning to the primarily Muddy Dolostone-dominated C Zone. This highly porous unit exhibits vuggy porosity and partial replacement by gray Dolomite (Fig. 2.6). Dolomite also infills some chert dissolution vugs while hydrocarbon fills the remaining porosity between chert grains and dolomite rhombs (Fig. 2.7).

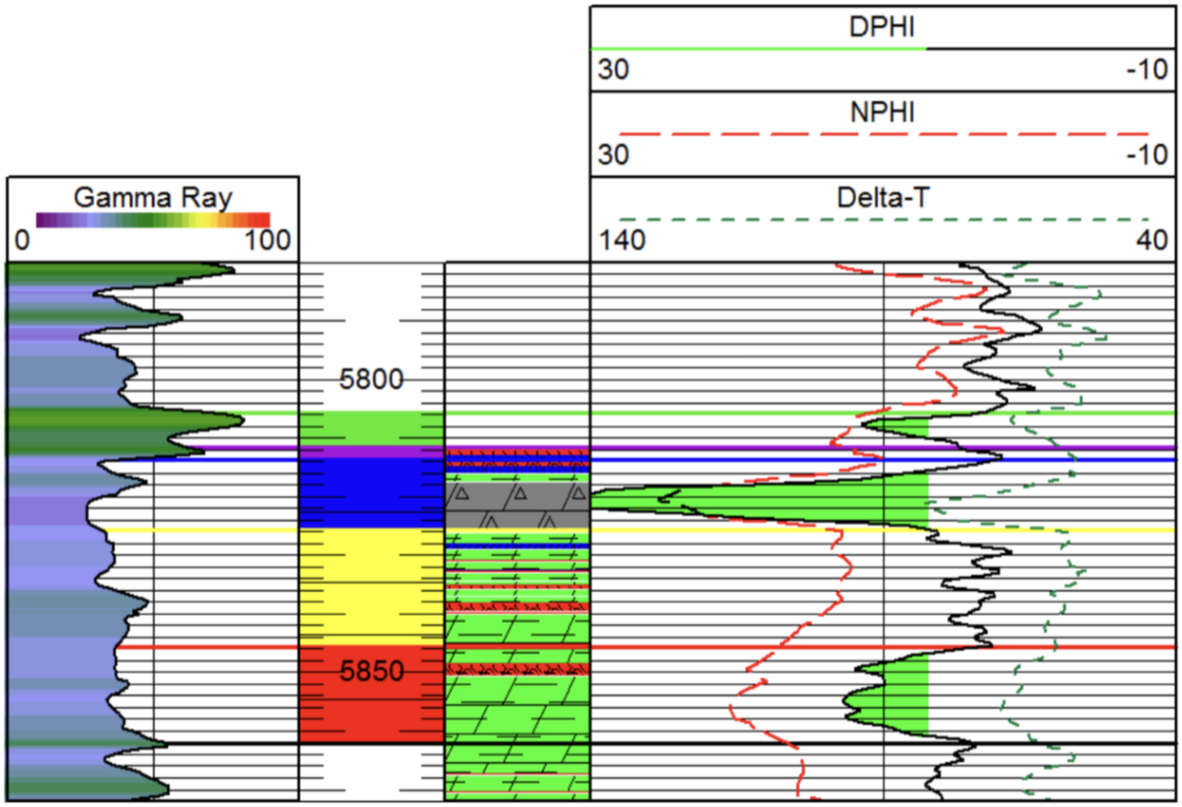

Figure 2.5: The "B" Zone highlighted in blue along the depth track is where slower Vp velocities and higher neutron porosity values are present, corresponding with the cherty Dolomite. A, B, and C zones are highlighted in green, blue, and red. The green highlighting along the right log track depicts porosity above 15% (Hagood et al., 2019).

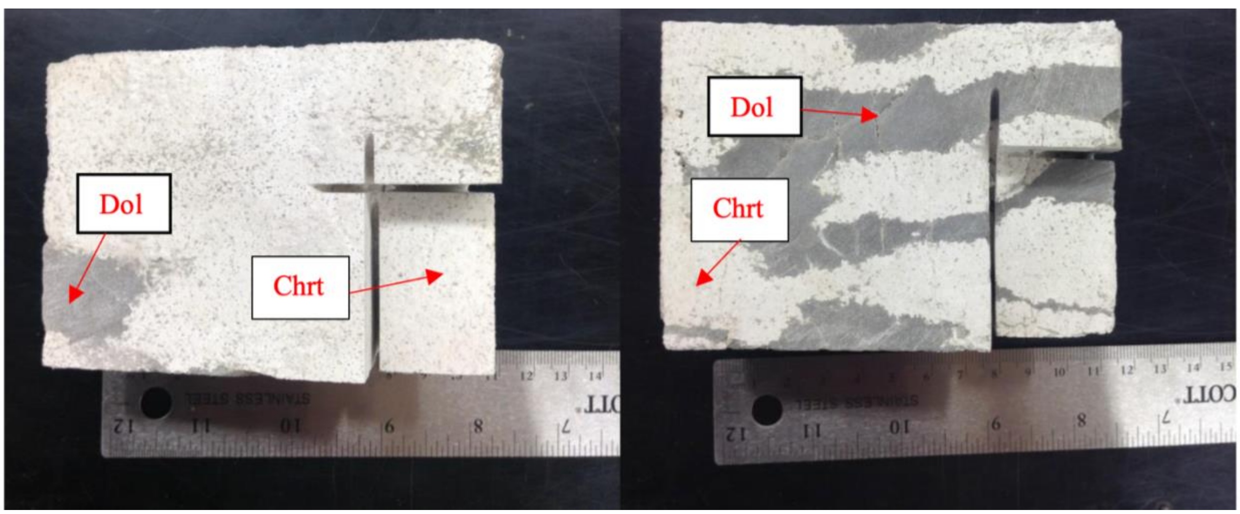

Figure 2.6: Cored section of cherty Dolomite in the Viola Ls. from Rich C #7 at depths 5818.5' (left) and 5822' (right). Dolomite (Dol) can be seen replacing the Chert (Chrt) (Hagood et al., 2019).

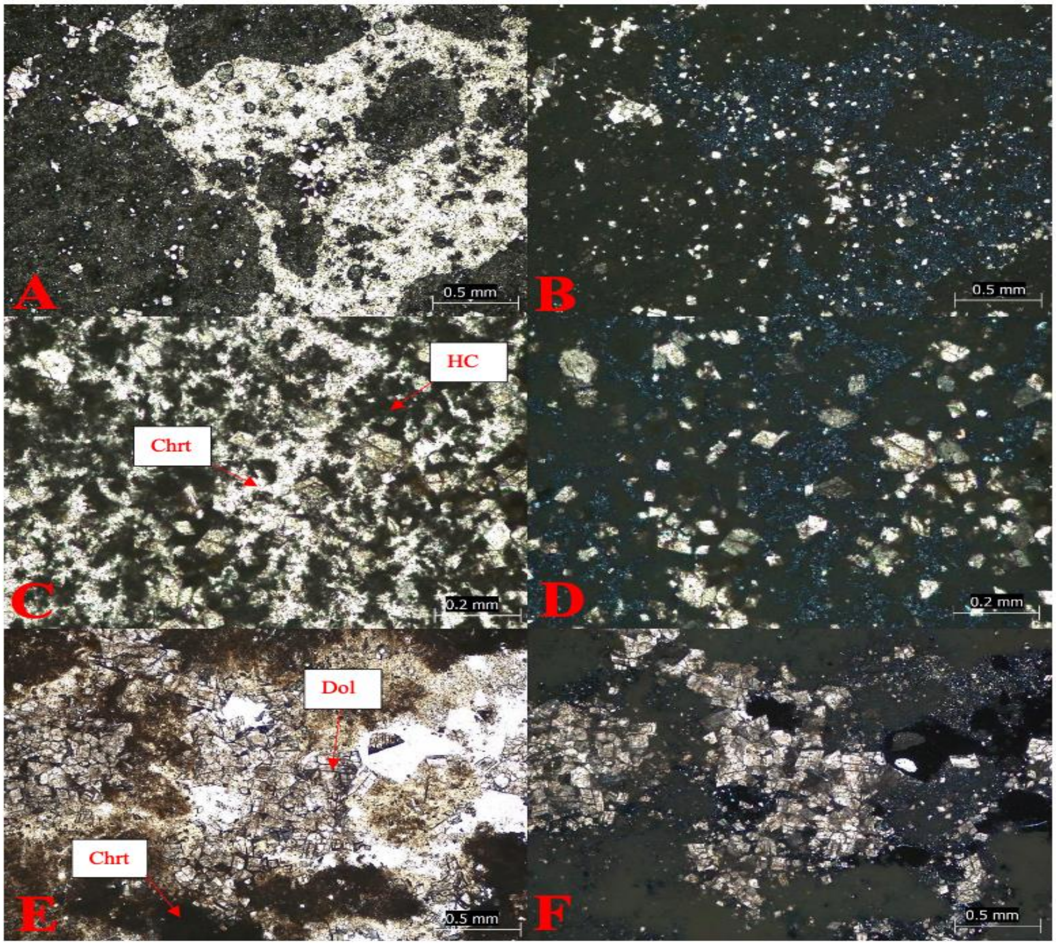

Figure 2.7: Thin section photomicrographs of cherty Dolomite. A) plain polarized light (PPL) and B) cross polarized light (XPL) image at 5818.5'. C) PPL and D) XPL image at 5818.5' displaying hydrocarbons (HC) inside the porosity of siliceous grains. E) PPL and F) XPL image at 5822' displaying the replacement of chert (Chrt) with Dolomite (Dol) (Hagood et al., 2019).

2.4 Seismic Resolution and Tuning

Seismic resolution and tuning are fundamental concepts in seismic exploration, playing a crucial role in interpreting reservoir geologic properties. These concepts are essential when analyzing seismic data to accurately identify and delineate hydrocarbon reservoirs.

Seismic resolution refers to distinguishing between separate features within the subsurface based on their seismic reflection responses. It measures the smallest detail that can be resolved in the seismic data. The bedrock of our knowledge regarding seismic vertical resolution stems from the pioneering research conducted by Ricker (1953), Widess (1973), and Kallweit and Wood (1982). Higher resolution enables identifying subtle geological features, giving geoscientists a clearer image of the subsurface. Various factors contribute to seismic resolution, including the frequency content of the seismic signal, the size of the subsurface features, and the velocity of the subsurface materials. The vertical resolution, defined as the limit of separability, in seismic data corresponds to a quarter of the wavelength ($\lambda/4$) (Brown, 2011). The limit of visibility (Brown, 2011), also known as detectability, may fluctuate based on the quality of seismic data. In instances where the seismic data has a high signal-to-noise ratio, the limit of visibility can shrink to as little as $\lambda/30$ (Brown, 2011). Regarding good quality 3D migrated seismic data, the horizontal resolution is typically around ($\lambda/2$) (Heron, 2011).

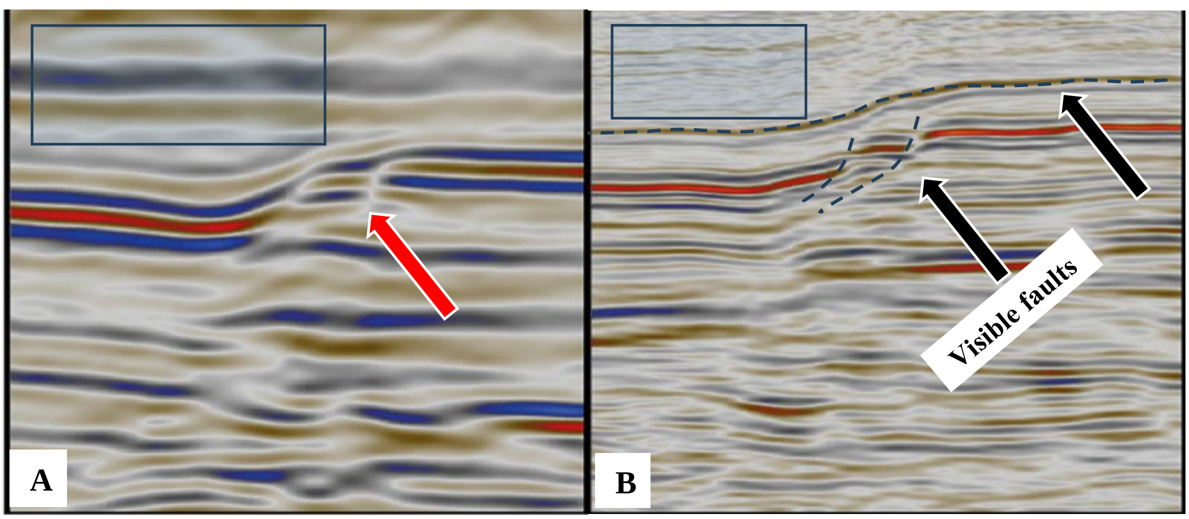

Figure 2.8: Seismic data for approximately the same location. (A) 2D conventional seismic line from 1985, (B) seismic line in the 3D high-resolution (P-Cable) cube from 2014 (modified after Faleide et al., 2019).

Depending on the processing techniques and acquisition parameters, seismic signatures from the same location can have different resolutions. For example, the highlighted box in the seismic line from 1985 (Fig. 2.8A) shows continuous and bright seismic reflections but a small number of reflections. In contrast, the seismic events (Fig. 2.8B) in the highlighted box are chaotic and less bright but with several reflections (more detailed), while other parts are bright and continuous. Two faults (Fig. 2.8B) can be seen easily, and the horizontal dashed line highlights the contrast in seismic stratigraphy.

On the other hand, tuning refers to the phenomenon that results in constructive or destructive interference between reflections from the layer's top and bottom of a thin bed, amplifying or attenuating the overall seismic response. Widess (1973) defines a "thin bed" as a bed whose thickness is substantially less than the dominant wavelength of the seismic pulse propagating through the bed. While processing seismic data, significant efforts are made to enhance seismic resolution using techniques like statistical deconvolution, inverse Q-filtering, and spectral whitening. However, these methods prove to be ineffective when the reservoir intervals to be characterized are thin. Practical seismic interpretation requires careful consideration of both resolution and tuning. Identifying tuning zones and accounting for their limitations are crucial for accurately assessing subsurface features, especially thin reservoirs.

2.5 Seismic Attributes and Tuning

Seismic attributes are measurable properties of seismic data, such as amplitude, dip, frequency, phase, and polarity which can be measured at one instant in time or over a time window and may be measured on a single trace, on a set of traces, or on a surface interpreted from seismic data (Schlumberger Oil Field Dictionary). A valuable seismic attribute is either directly responsive to the desired geological feature or reservoir property under investigation or enables us to characterize the structural or depositional setting, thereby allowing us to deduce certain features or properties of interest (Chopra & Marfurt, 2005).

In addition to the comprehensive understanding required for accurate reservoir delineation in the face of tuning effects, it is crucial to consider instantaneous seismic attributes. Instantaneous seismic attributes (Fig. 2.9) are values calculated individually for each sample at specific time or depth intervals, reflecting a continuous variation in properties across time and space (Roden et al., 2017). These attributes, such as instantaneous amplitude, phase, and frequency, provide valuable insights into subsurface structures and properties at specific moments in time. Unlike other seismic attributes that may be measured over a time window, instantaneous seismic attributes capture instantaneous variations in seismic data, offering a more detailed and dynamic view of the subsurface. Integrating instantaneous seismic attributes enhances our ability to characterize geological features and reservoir properties accurately.

The impact of tuning on various seismic attributes (brightening or dimming) is complex and demands a comprehensive understanding to ensure accurate reservoir delineation. Tuning can cause significant variations in seismic amplitude across a geological layer. As the thickness of the layer approaches the tuning thickness, the amplitude of the seismic reflections increases due to constructive interference. This phenomenon is particularly noticeable in bright spots, where hydrocarbon reservoirs exhibit high seismic amplitudes due to tuning effects (Taner et al., 1979). Conversely, tuning can also lead to amplitude attenuation in thin reservoirs or at the edges of thicker reservoirs, impacting the detectability of hydrocarbon accumulations.

Tuning alters the phase characteristics of seismic reflections, leading to phase reversals and polarity changes in seismic data. Near the tuning thickness, phase reversals occur due to the constructive interference of seismic waves, resulting in abrupt changes in seismic polarity. These phase changes can complicate seismic interpretation, especially in areas with complex geological structures or multiple reflections (Sheriff & Geldart, 1995).

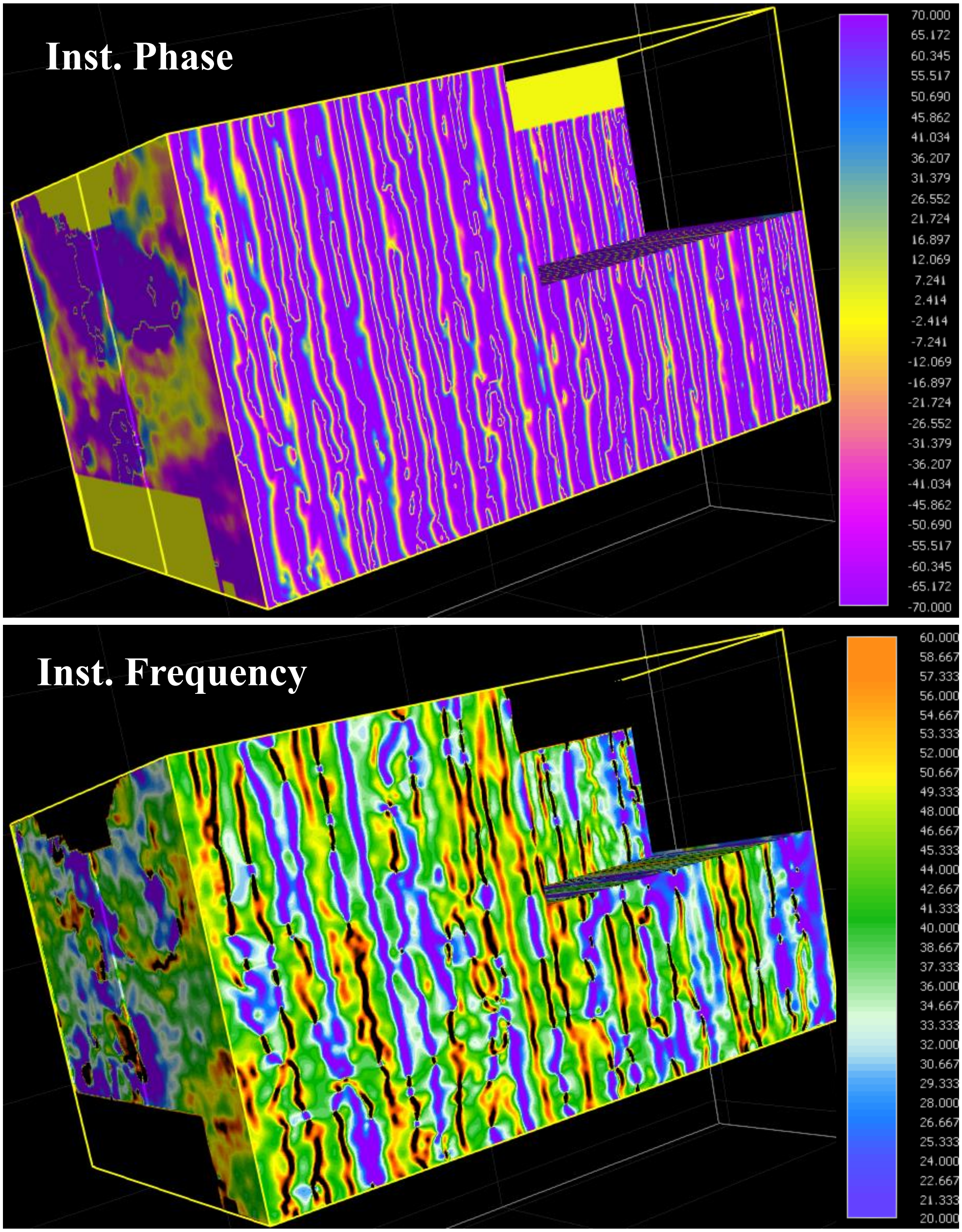

Figure 2.9: Instantaneous Phase and Instantaneous Frequency in 3D view.

Tuning affects the dominant frequency of seismic reflections from geological layers. Near the tuning thickness, the seismic signal experiences a peak in frequency, resulting in a narrower bandwidth of frequencies and a dominant peak at the tuning frequency. This phenomenon is observed in thin-bed reservoirs, where tuning enhances the resolution of seismic reflections and improves the identification of thin hydrocarbon-bearing intervals (Sheriff & Geldart, 1995).

2.6 Machine Learning and Tuning

By understanding and learning the geophysical relationship between seismic responses and corresponding indicators for reservoir thickness, machine learning models could automatically detect the locations of the top and base of reservoir bodies identified from seismic traces by precisely revealing the lithology distribution. For hydrocarbon exploration, seismic attributes provide valuable insights into seismic data for the characterization of reservoirs. Using either a single seismic attribute or a combination of seismic attributes, subtle geologic structures, stratigraphic features, thin beds, and spatial distributions of reservoir petrophysical properties can be delineated. The geometry, kinematics, dynamics, and statistics of the waveforms in seismic data are all reflected in the seismic attributes (Brown, 1996).

Machine learning models help recognize complex hidden data structures or patterns with various computational methods or concepts. Using machine learning algorithms on seismic data is an alternative strategy for conventional seismic interpretation. Through precise interpretation, these methods have the potential to expedite the process and provide experts with valuable assistance. Numerous supervised machine learning models, including Support Vector Machines (SVM), Decision Trees, Multilayer Perceptron Neural Networks (MLP), and Convolutional Neural Networks, have been investigated for seismic signal classification tasks. Predefined labels, which result from human interpretation of seismic data, are used in these algorithms to train models and improve their ability to recognize labels in each dataset. As a result, the interpreter's overall performance and success are tied to the labels on the seismic data.

In contrast, unsupervised machine learning models are a class of algorithms that discover hidden patterns and relationships in the data without labels. Using such algorithms can help the expert achieve a more accurate interpretation by identifying new relationships between seismic attributes that were previously unknown. These models have many advantages due to the large amount of seismic data and the absence of labels in new exploration. In addition, the structures of lithological data can be obtained by applying this kind of algorithm to data other than seismic, such as well logs. A robust interpretation model can be produced by linking those results to the seismic data. Some clustering algorithms include the simple Cross plotting method, K-means clustering, Self-organizing maps (SOM), Principal component analysis (PCA), and Generative Topographic Mapping (GTM) (Zhao et.al, 2015).

Roden et al. (2017) emphasized the underutilized potential of instantaneous attributes in thin-bed analyses. They proposed a seismic multiattribute approach that leverages self-organizing maps to identify natural clusters from combinations of attributes exhibiting below-tuning effects. Through this approach, the study aimed to provide a more precise identification of thin beds, addressing the shortcomings of traditional methods. The methodology was validated against extensive well control data, demonstrating its effectiveness in accurately mapping facies below tuning without being constrained by traditional frequency limitations.

Machine learning models can effectively identify amplitude variations indicative of tuning effects, leading to improved detection of hydrocarbon reservoirs through analysis of seismic amplitude spectra or maps (Satinder & Kurt, 2007).

Chapter 3 - Data and Methods

3.1 3D Seismic Data

The 3D seismic survey for the Morrison NE field, Clark County, Kansas, was acquired in 2010 by Coral Coast Petroleum. The seismic data (Fig. 3.1) consists of 320 inlines, 380 crosslines, and a bine size of 82.5 ft x 82.5ft. A sampling rate of 2ms and data length of 2 seconds was used during the acquisition. The 3D seismic survey was conducted to explore the ideal conditions favorable for Viola production.

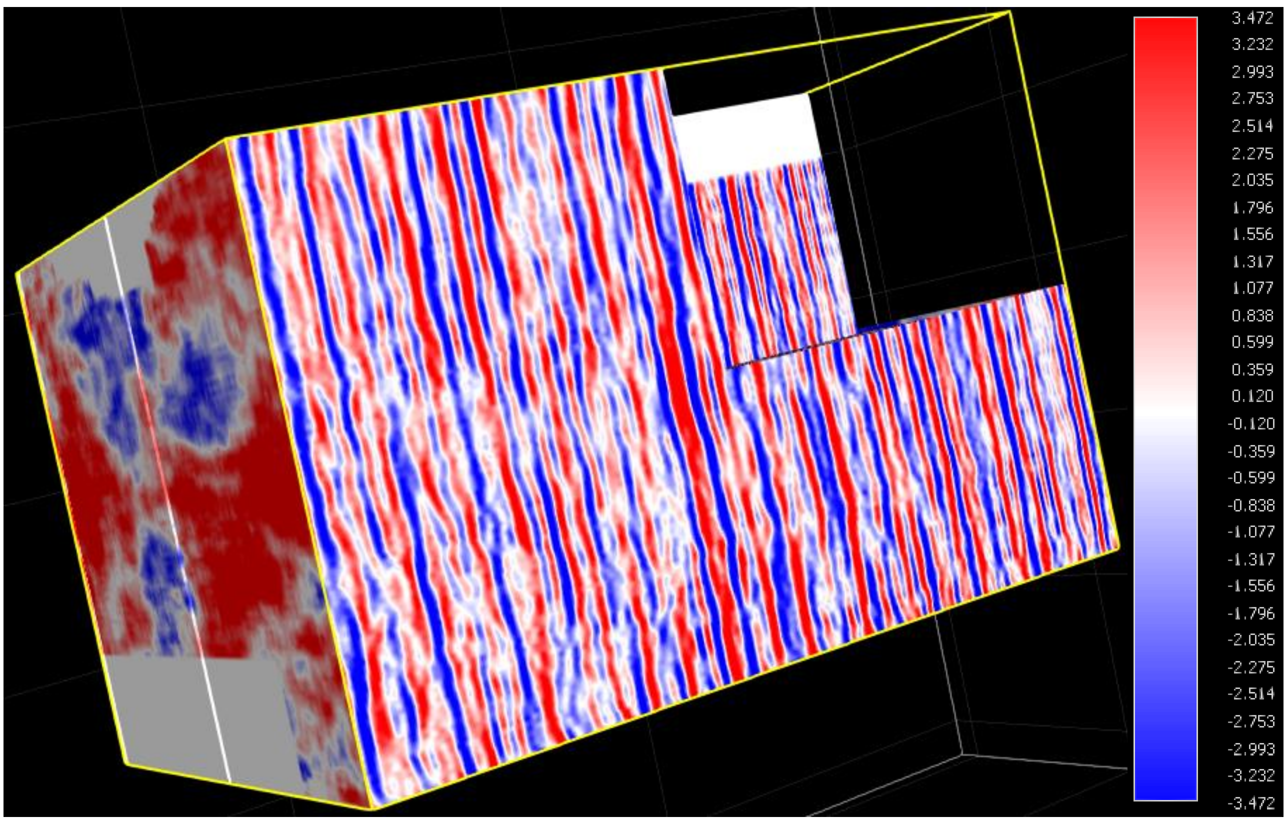

Figure 3.1: Stephens Ranch 3D seismic volume in a 3D view.

3.2 Geophysical Well Logs

Geophysical well logs are measurements of physical properties, such as resistivity, density, and sonic velocity, obtained by lowering sensors into a borehole. Eight wells are available in this study; some are producing wells (Stephens 1, Stephens 4, Stephens 6, Stephens 7, and Harden 1), while others are nonproducing wells (Stephens 3, Stephens 8 & Stephens 5). The well logs were utilized for generating synthetic wedge models, seismic-to-well ties, correlation, and building mineral composition profiles. Porosity (NPHI), density (RHOB), photoelectric (PE), and sonic (DT) logs were used to generate mineral composition profiles. Additionally, a cross-plot between porosity and amplitude was performed to observe the change in relationship before and after detuning.

3.3 Seismic Wavelet Extraction

The seismic wavelet serves as an essential bridge connecting seismic data (traces) with the stratigraphy and rock properties in the subsurface (Tianci & Gary, 2014). It is a mathematical representation of the seismic signal recorded by sensors (geophones or hydrophones) in response to energy waves generated by seismic sources. These recorded signals contain valuable information about the geology of the subsurface. We extracted the wavelets from a radius of ten seismic traces around well locations from the seismic data using the frequency extraction method in the IHS Kingdom suite (Fig. 3.2). The wavelets were utilized to generate synthetic seismograms, deterministic tuning curves, and wedge models. Theoretical wavelets (Ricker) of different frequencies were also used to create synthetic wedge models. The wavelet shape, wavelength, and frequency play a crucial role in the resolution of the seismic data. The extracted wavelets (Fig. 3.3 & 3.4) have different shapes and numbers of side lobes (peaks and troughs) due to differences in geology around the well locations. The amount of tuning is highly dependent on the number of side lobes.

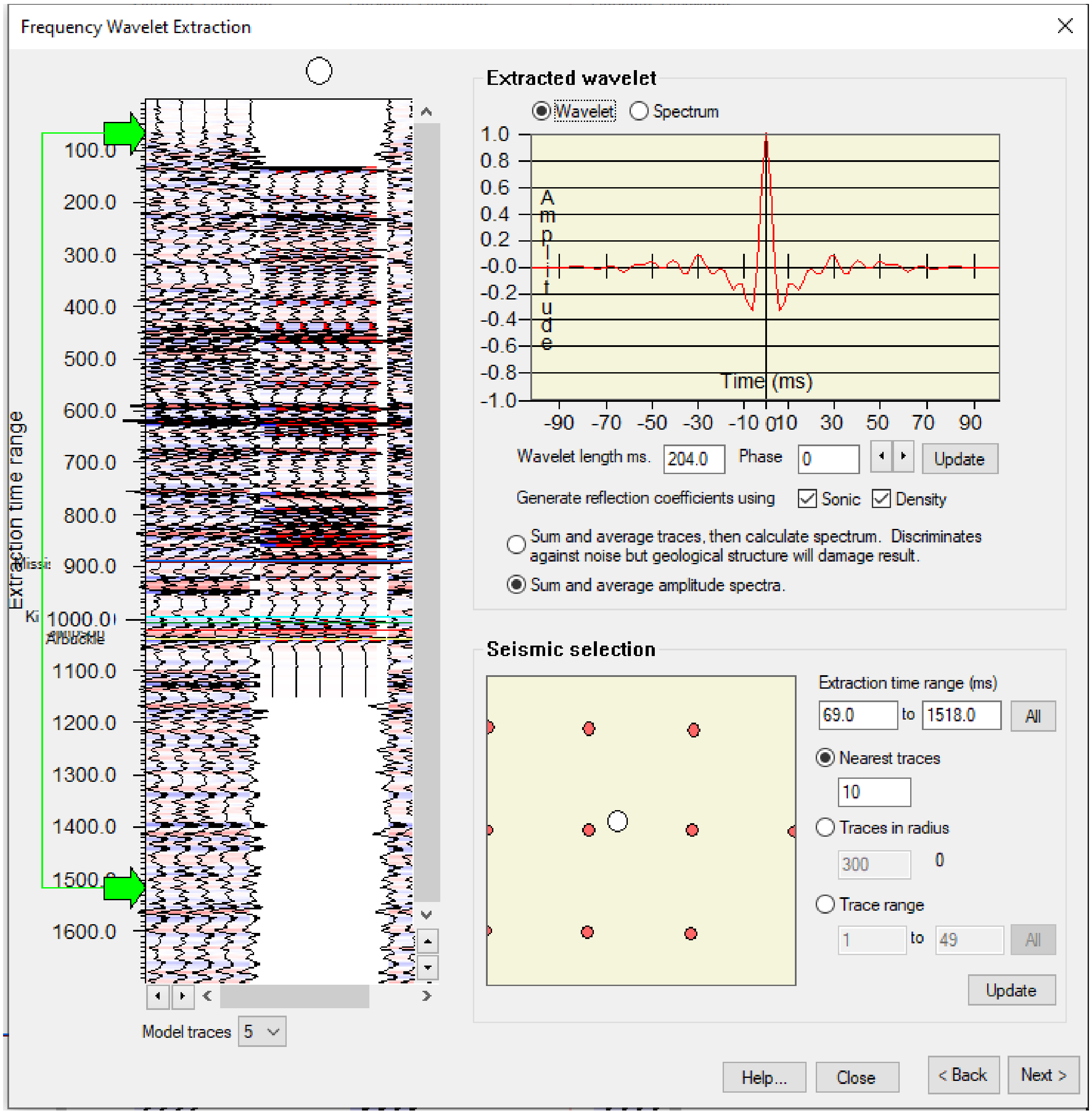

Figure 3.2: Frequency wavelet extraction process with an extraction time range of 69ms to 118ms around 10 seismic traces.

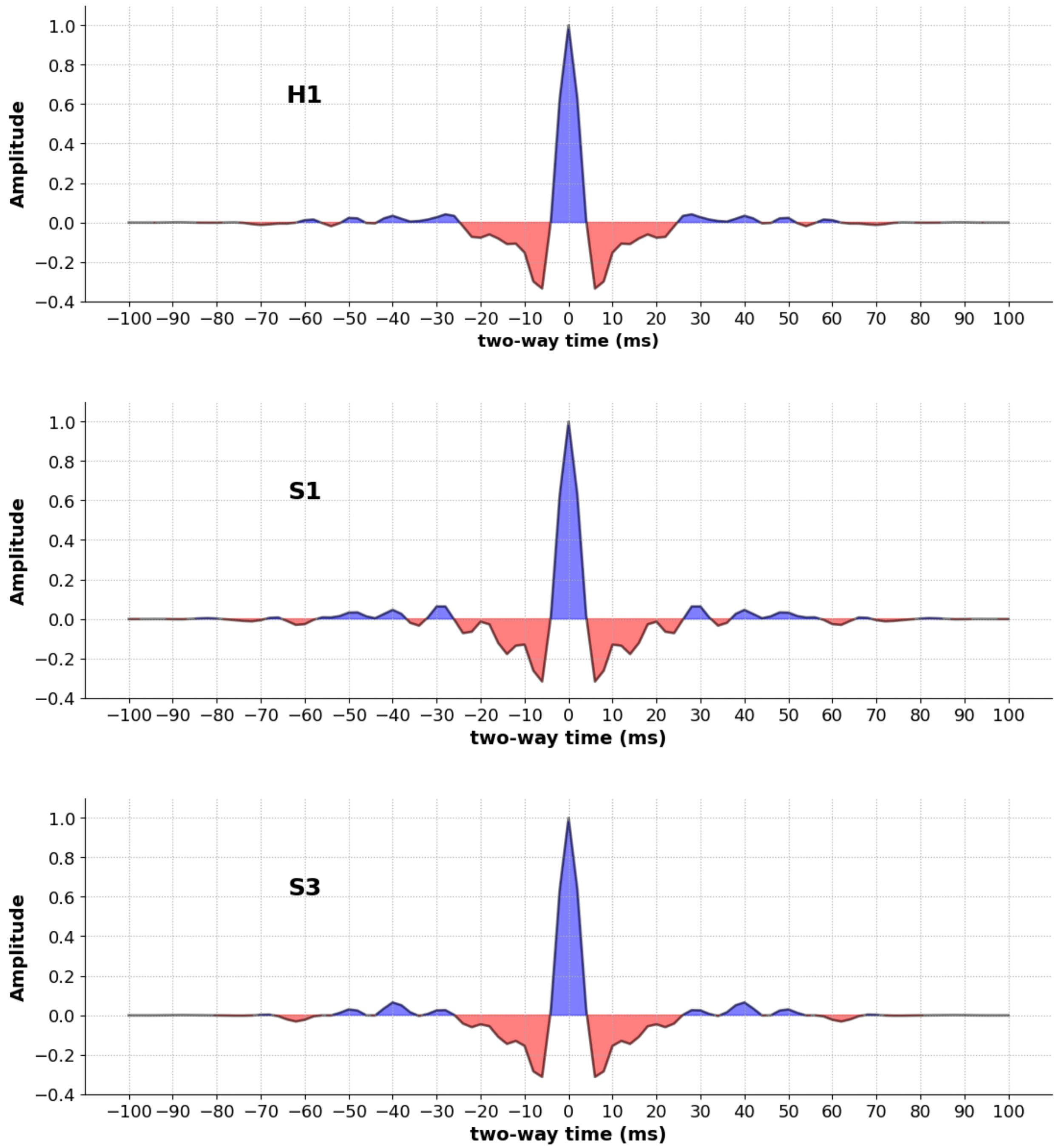

Figure 3.3: Extracted wavelets for Hardens1, Stephens1, and Stephens3

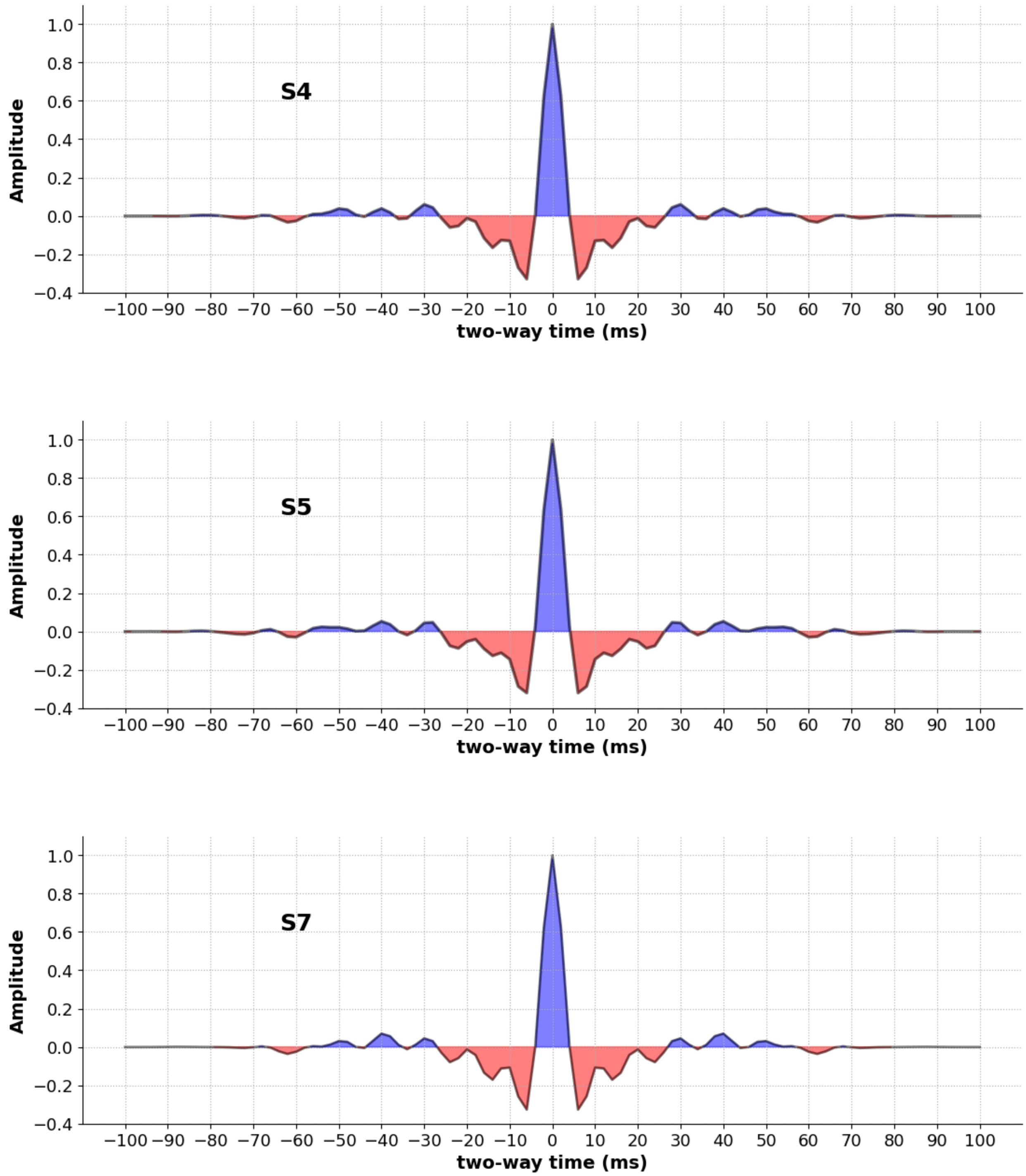

Figure 3.4: Extracted wavelets for Stephens4, Stephens5, and Stephens7.

3.4 1D Synthetic Modeling and Well-to-seismic tie

The 3D seismic survey for the Morrison NE field, Clark County, Kansas, and well logs covering the field were used to generate synthetic seismograms that represent the subsurface geology of the study area with the aid of the IHS Kingdom software. This was achieved by matching the synthetic seismogram generated from the well data with the actual seismic data from the survey and adjusting the model until a good fit was obtained (Fig. 3.5). This allows the higher-resolution data from the well to interpret the lower-resolution seismic data and vice versa. Establishing a time-depth relationship enabled mapping horizons of interest from the well logs to the respective seismic reflector.

The Viola horizon was mapped with the appropriate seismic reflector marking the top to generate time structure maps that can be used as surfaces to extract seismic attributes. Seismic attributes were extracted from the mapped horizons utilizing the IHS Kingdom suite. This helps to connect geology from boreholes to 3D seismic data.

3.5 Seismic Attributes Extraction

Seismic attribute extraction identifies and quantifies subsurface rock physical properties by analyzing seismic data. The goal of seismic attribute extraction is to create a more detailed understanding of the subsurface and to identify potential hydrocarbon reservoirs for exploration and production. The IHS Kingdom software was used to extract the Viola horizon's seismic amplitude and waveform characteristics (Fig. 3.6 to 3.9). Extracted attributes like instantaneous frequency and amplitude were detuned using the proposed data-driven method and utilized as input features for training machine learning models.

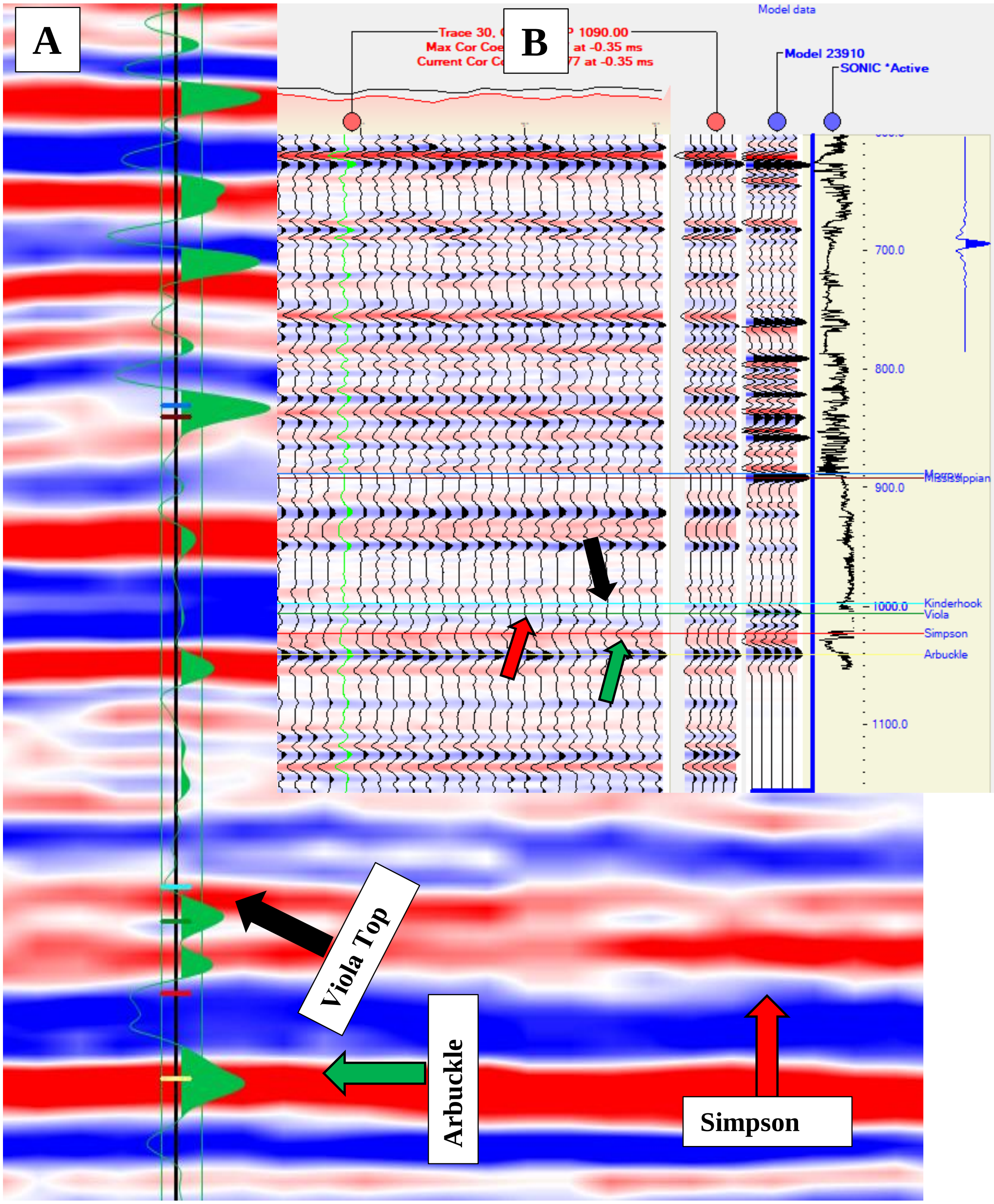

Figure 3.5: The seismic well tie (A) shows the Viola peak reflector (black arrow), Simpson trough reflector (red arrow), Arbuckle peak reflector (green arrow), and a Synthetic (B) 1-D trace model obtained from Stephens1.

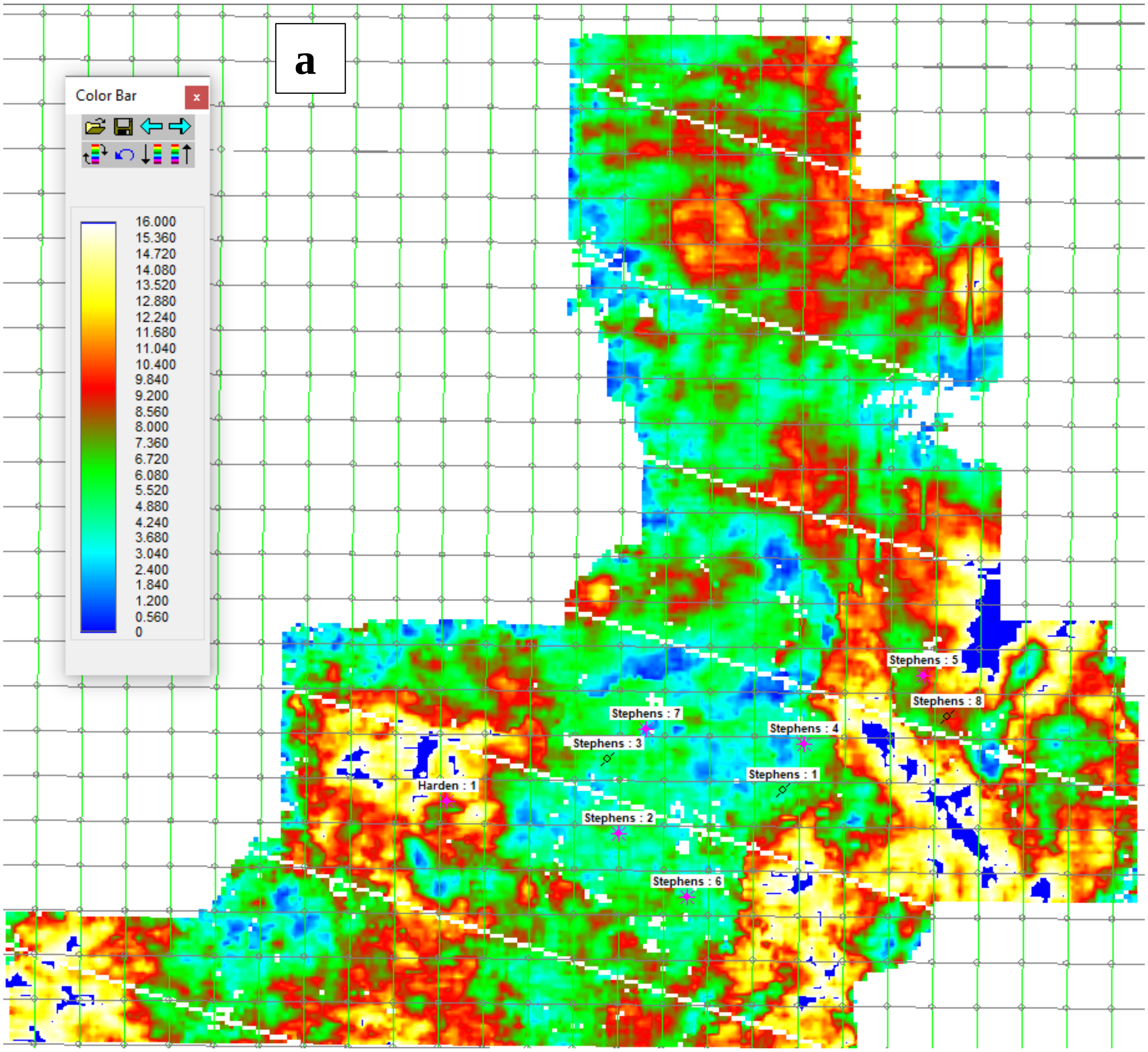

Figure 3.6: Amplitude map (a) of the Viola Limestone top. Amplitude values are represented by the color bar on the left.

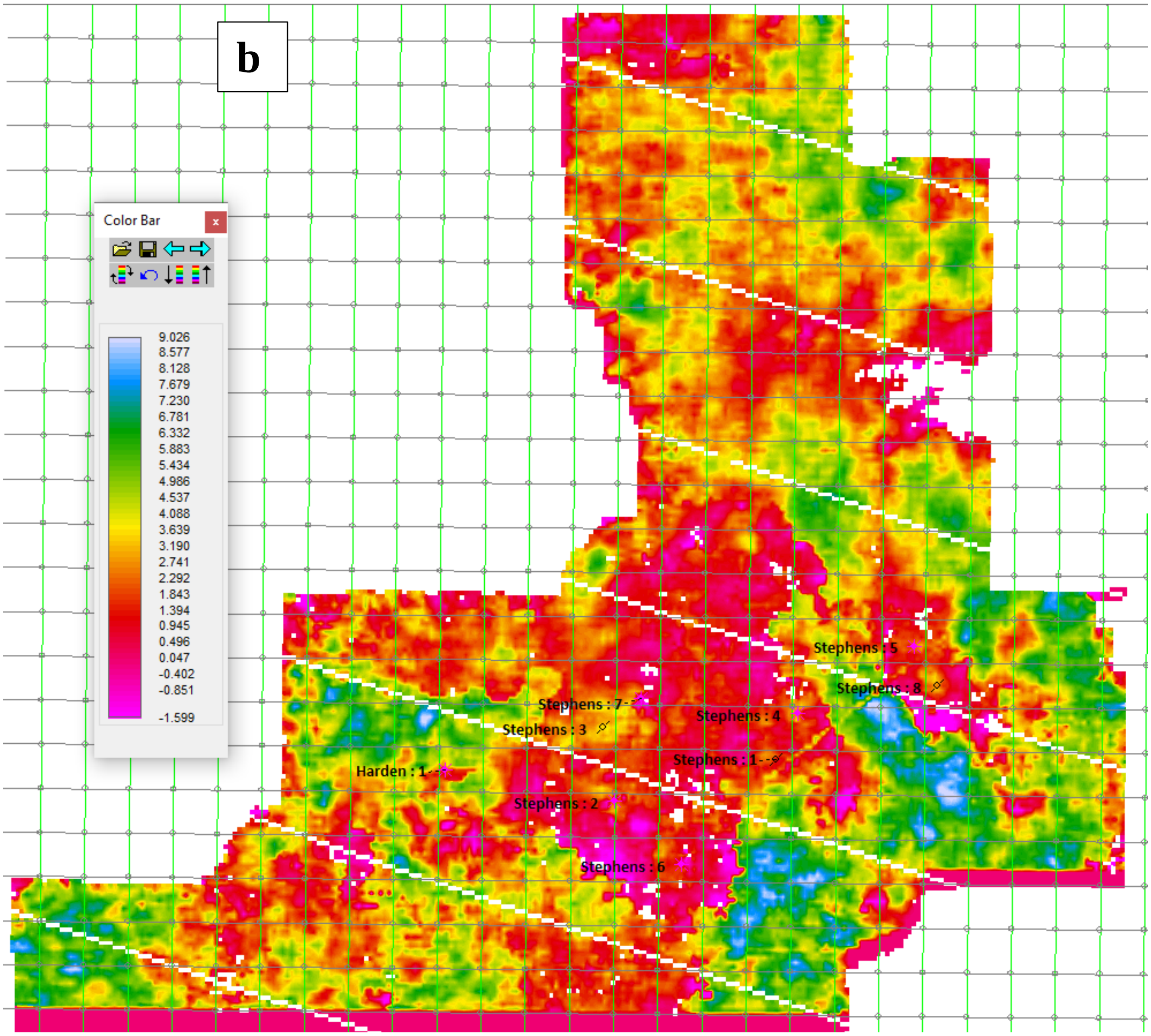

Figure 3.7: Reflectivity Strength (b) of the Viola Limestone top. Reflectivity Strength values are represented by the color bar on the left.

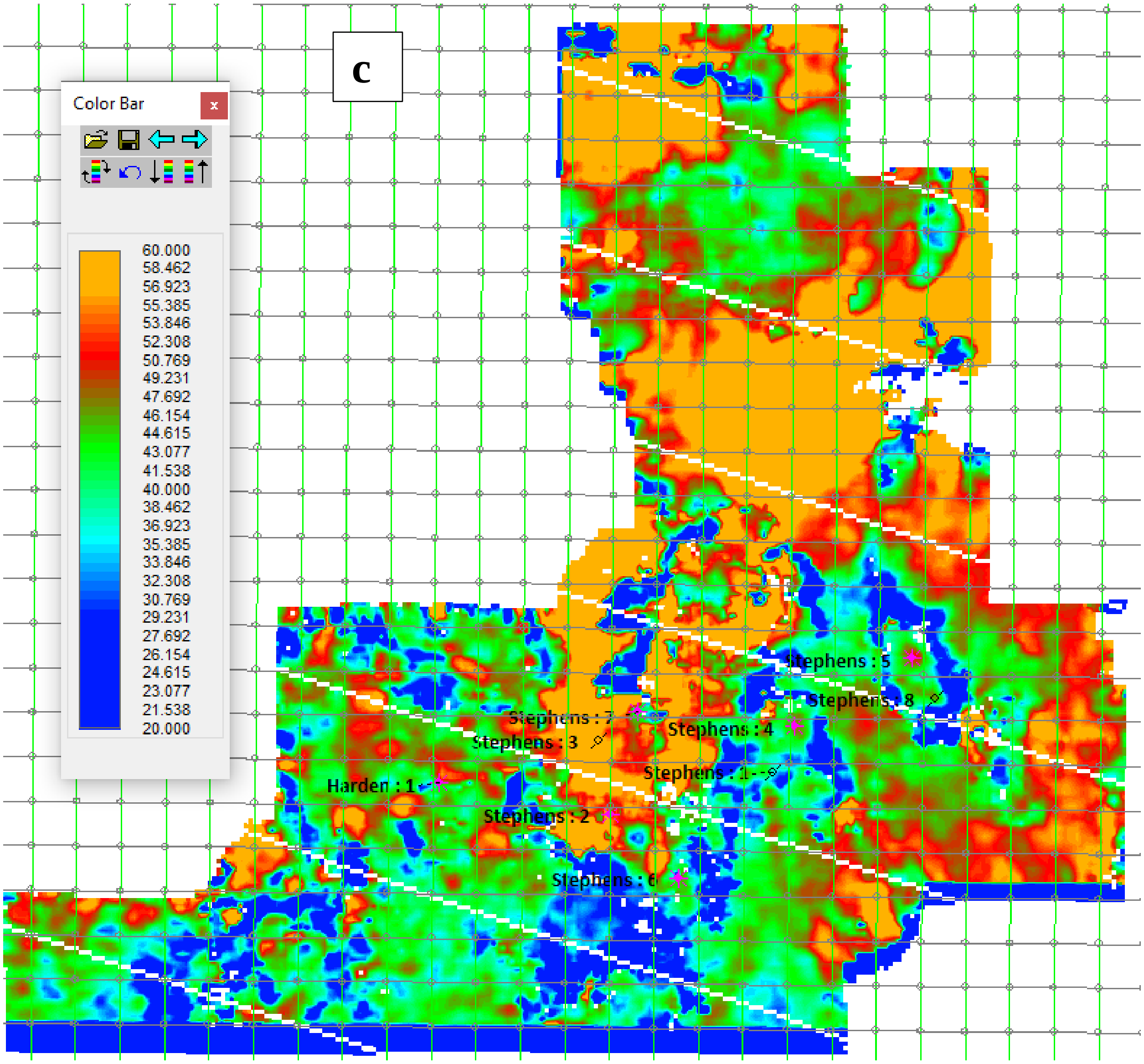

Figure 3.8: Instantaneous Frequency (c) of the Viola Limestone top. Instantaneous Frequency values are represented by the color bar on the left.

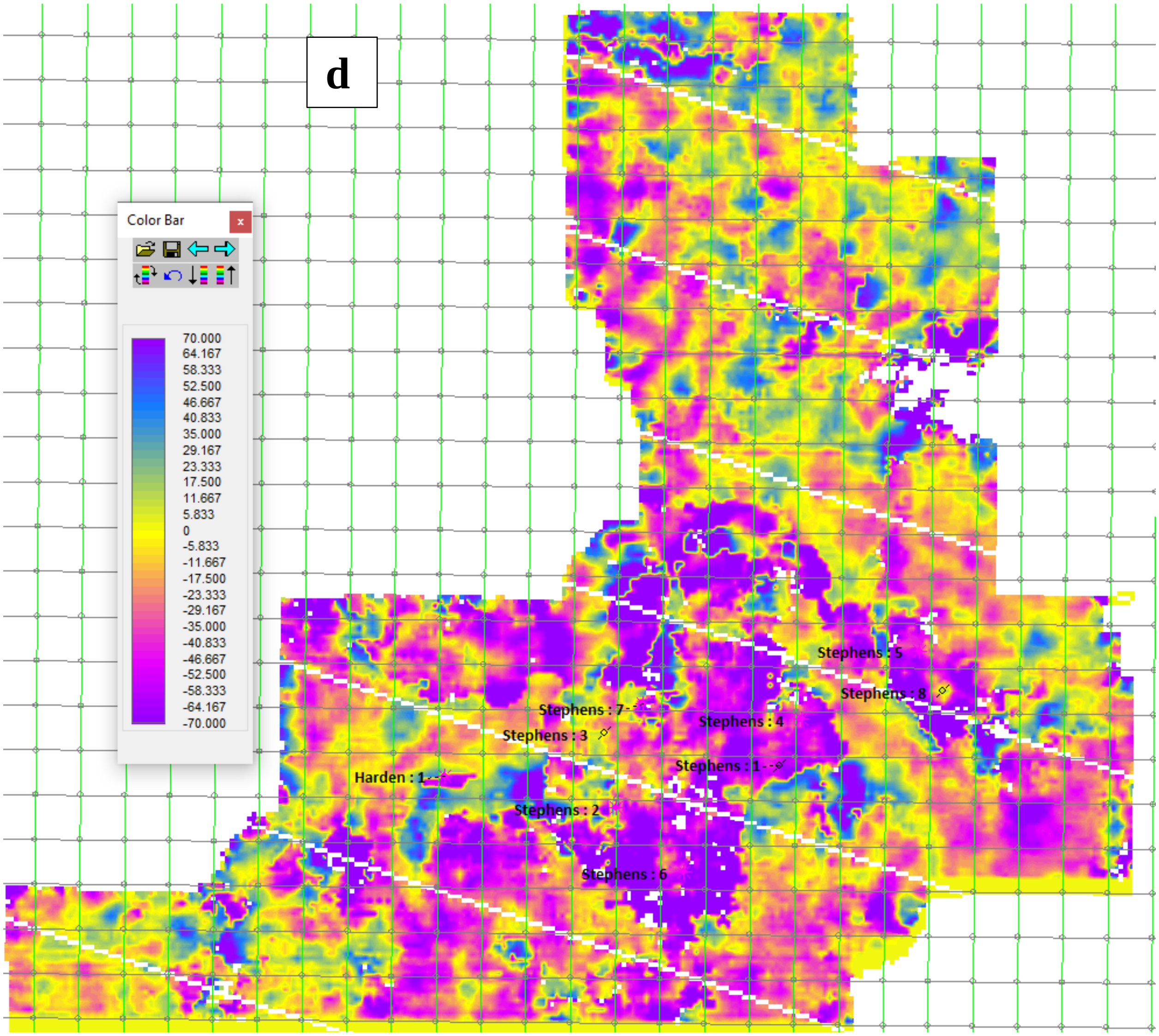

Figure 3.9: Instantaneous Phase (d) of the Viola Limestone top. Phase angles are represented by the color bar on the left.

3.6 Deterministic Wedge Model Approach

Synthetic wedge models were used for quantitative interpretations from seismic data to study the tuning thickness, vertical resolution, travel time shift below the tuning thickness, and amplitude decay below the tuning thickness. The wedge models consist of three layers (Maquoketa, Viola & Simpson) with varying thicknesses of the Viola and constant acoustic impedance at well locations arranged in a wedge-shaped configuration (Fig. 3.10). The amplitude variation is diagnostic of geometry (thickness) rather than geology (impedance). The brightening and dimming can be misinterpreted as direct hydrocarbon indicators. With a large thickness (>75m), the amplitude (0.175) is constant due to zero interference between the top and bottom of the Viola and, thus, the amplitude baseline (black dashed line). At $\frac{\lambda}{2}$ which is the onset of tuning; the peak side lobe of the viola bottom starts to interfere constructively with the central peak of the viola top by increasing the amplitude until the maximum tuning thickness $\frac{\lambda}{4}$ (31m). Beyond the tuning thickness, the central trough lobe of the viola bottom starts to interfere destructively with the main peak lobe of the viola top by causing dimming or decreasing amplitude.

Knowing which part of the curve (brightening or dimming) the reservoir of interest is located is crucial to adding or removing the tuning error. Various geological scenarios were examined by simulating and adjusting the wedge layers' thickness and angle to understand the seismic response due to tuning and to establish a tuning baseline (seismic attribute values in the absence of tuning). Wedge models were utilized to correct the seismic attribute anomalies by establishing the tuning baseline. The extracted seismic wavelets around the well locations and the IHS Kingdom software's simple wedge models were used to create apparent time thickness and normalized amplitude curves for the Viola limestone.

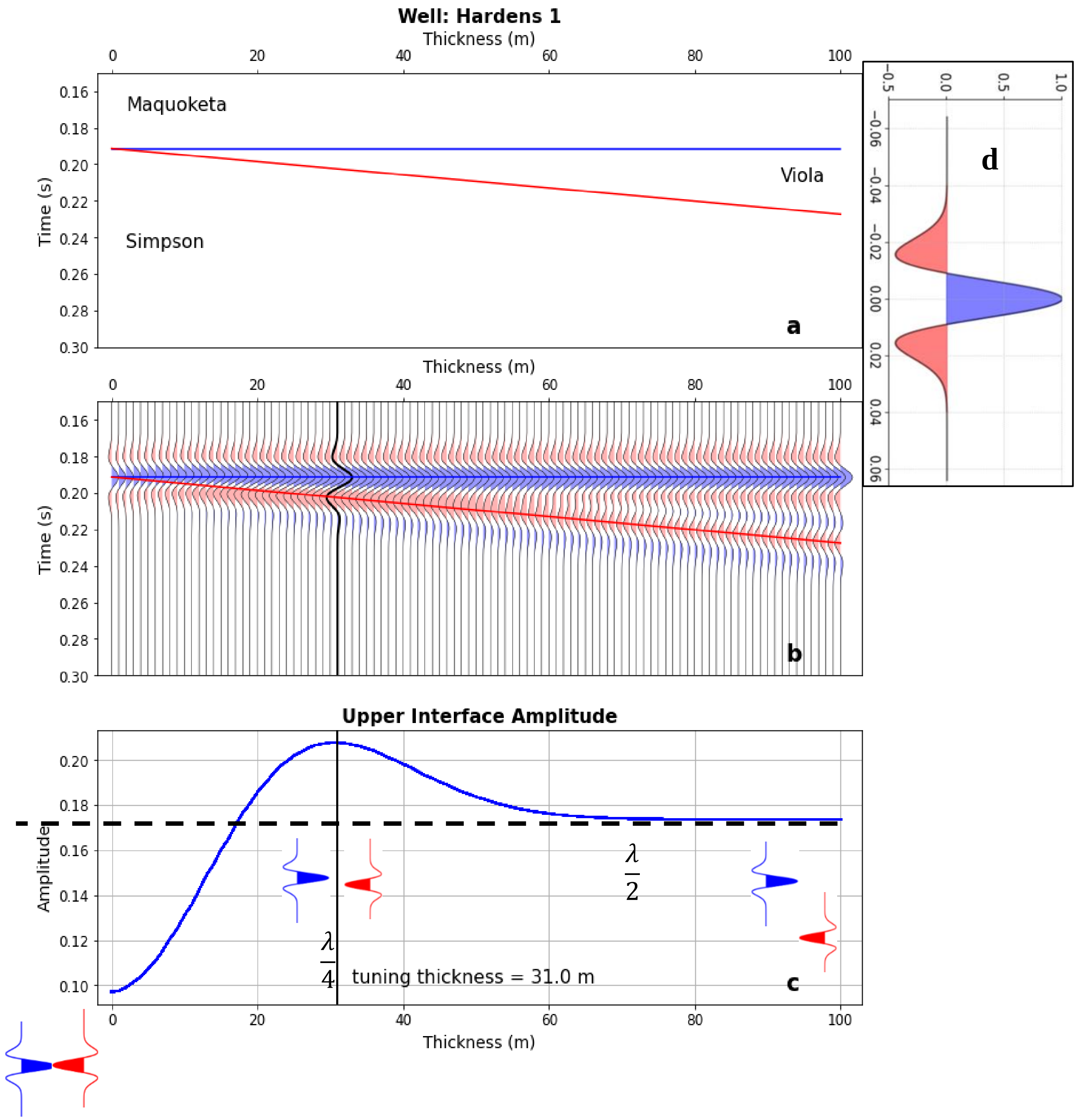

Figure 3.10: (a) A three-layer wedge model. (b) The constructive interference between the side lobes and main reflections produces brighter reflections, as seen in the zero-offset synthetic seismogram displayed in normal polarity. (c) The amplitude of the synthetic extracted along the top of the Viola reservoir. (d)The convolved Ricker wavelet of 38.5Hz.

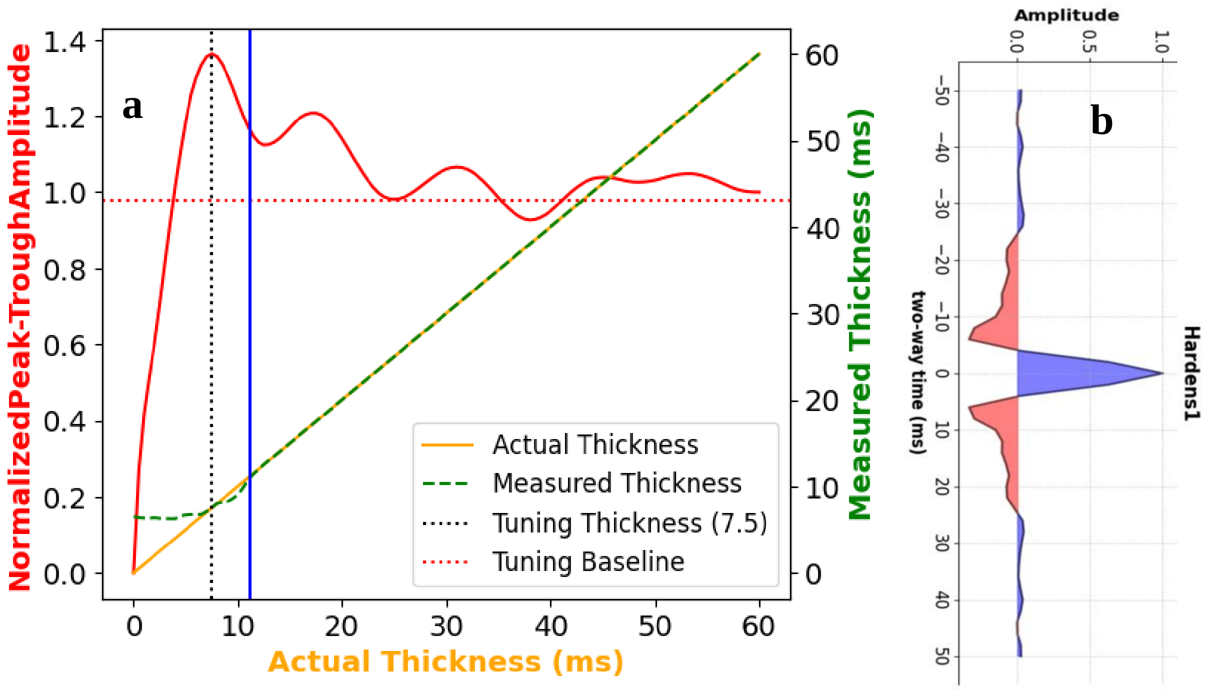

Figure 3.11: Deterministic tuning curve (a) of Hardens1 and the extracted wavelet (b) from the seismic around the well used for modeling.

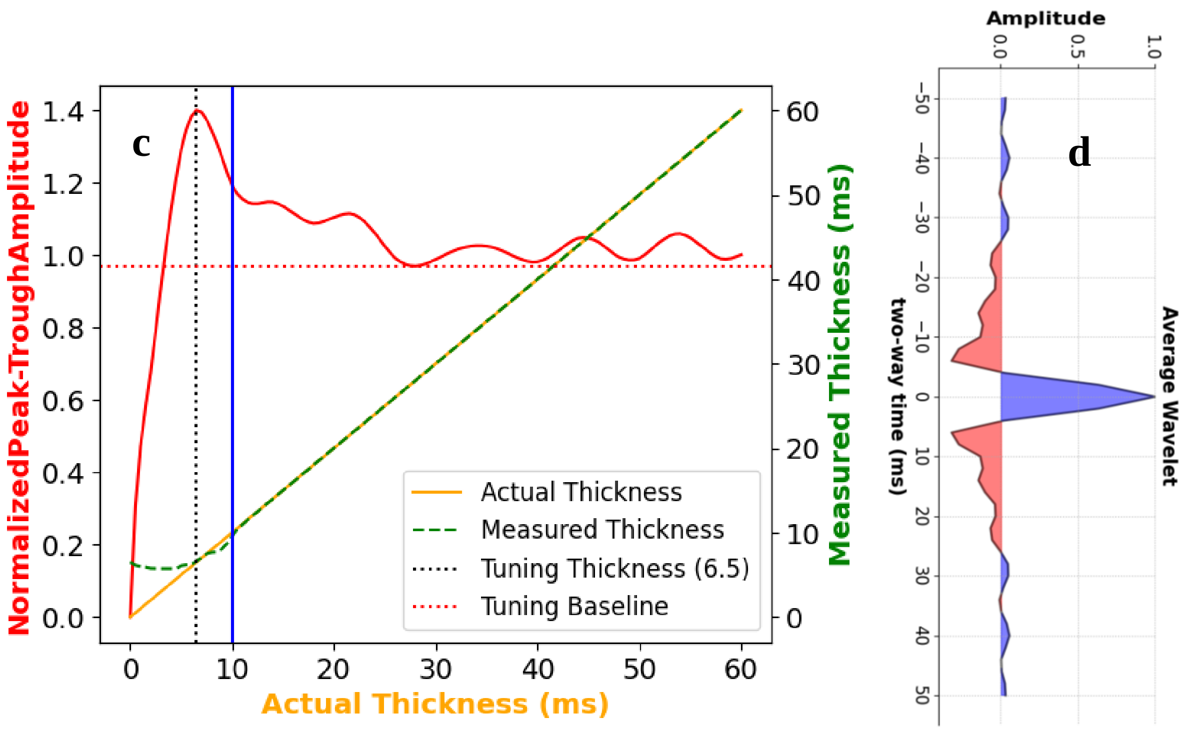

Figure 3.12: Deterministic tuning curve (c) of Hardens1 and the extracted average wavelet (d) from the seismic used for modeling.

Figures 3.11 and 3.12 above demonstrate deterministic tuning curves generated from the same well (Hardens1) utilizing two different wavelets, similar to what Meckel and Nath (1977) published. The difference between both tuning curves arises from the difference in wavelets. Thus, the number of peaks and troughs in a tuning curve depends on the number of sidelobes in the wavelet. Due to the inherent difference in measurement and scales between the well logs and the seismic data, there was a discrepancy in the seismic attribute (e.g., amplitude) ranges. Min-max scaling was implemented to scale the attribute values from the well logs to match those of the seismic horizons for accurate comparison and analysis (Fig. 3.13). By applying this scaling factor, we adjusted the attributes from the well logs to match those observed on the seismic horizons, ensuring consistency and reliability in subsequent analysis.

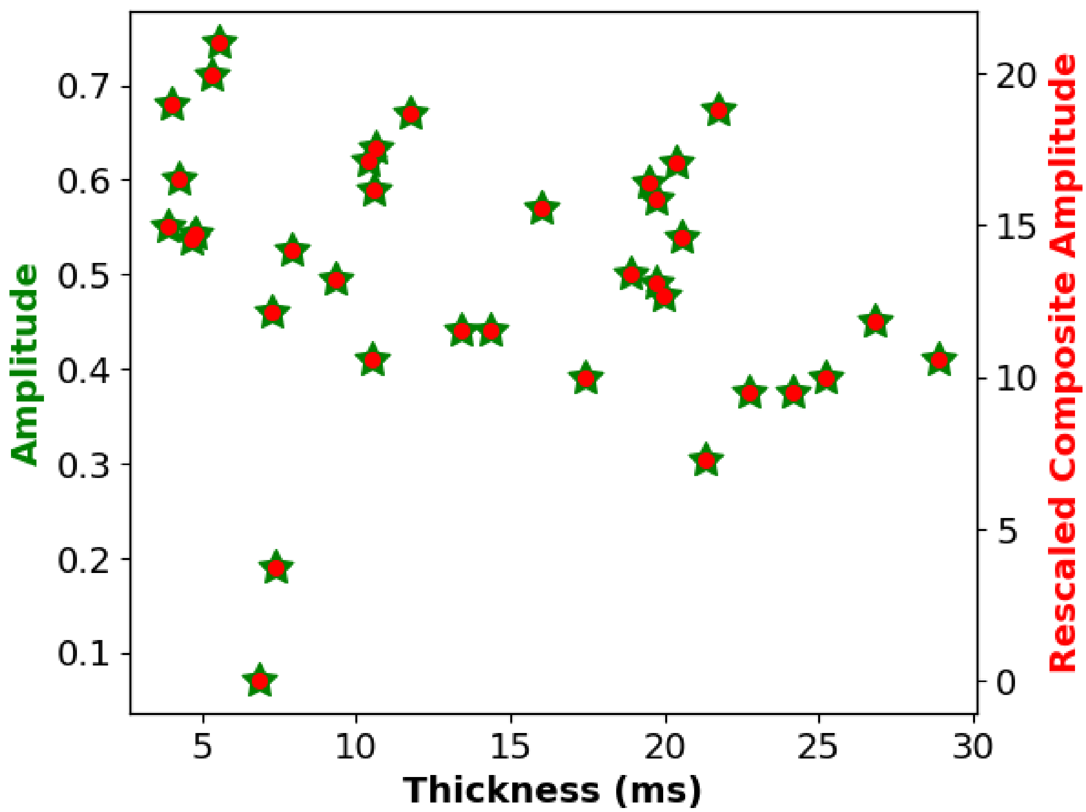

Figure 3.13: Shows the amplitude response (green stars) obtained from the wedge models rescaled to match the composite amplitude (red dots) scales of the seismic amplitude horizon.

Amplitude maps were extracted using stratal amplitudes onto the Viola top horizon. A Python code was created to detune the Viola top horizon by removing the geometric effects and enhancing amplitude anomalies diagnostic of reservoir properties. The program correlates the amplitude values with the normalized amplitude curves and the isochron values with the apparent time thickness curves. The curves were exported as text files, the isochron maps as ASCII files in the format of X-Y-Isochron values, and the amplitude maps as ASCII files in the format of X-Y-Amplitudes. The program expects .csv files as input files and interpolates isochron values onto the XY grid of the amplitude map to account for different grids (Fig. 3.14 & 3.15). The actual time thickness values are stored to produce a corrected isochron map and used to find the normalized amplitudes to correct the observed amplitudes using Equation 3.1 (Zachary et.al, 2020) below. The curves, isochrone map, and amplitude map were exported as text files, ASCII files (X-Y-Isochrone), and ASCII files (X-Y-Amplitude).

Equation 3.1: Relationship between horizon amplitude and normalized peak-trough amplitude.

$$A_C = A_H - \frac{1}{2}\left[(\tau_A - 1) * \frac{A_H}{\tau_A}\right]$$

Where τ_A is the wedge model's normalized peak-trough amplitude, A_H is the horizon amplitude, and A_C is the tuning-corrected amplitude. Since the wedge model uses peak-to-trough amplitudes, the horizon amplitude is centered on zero, so the second term is multiplied by a factor of $^1/_2$.

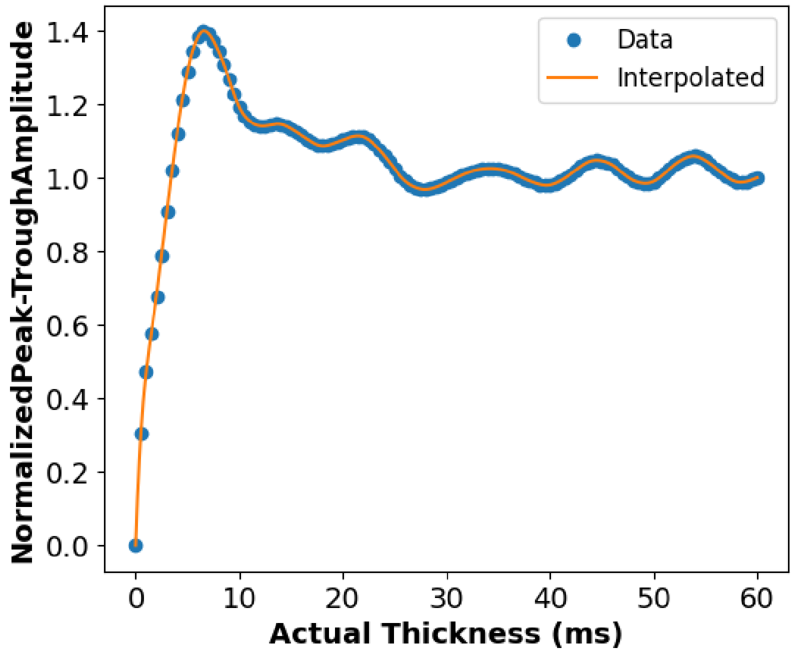

Figure 3.14: Shows the amplitudes (blue) and the interpolated amplitudes (orange) values for Hardens1.

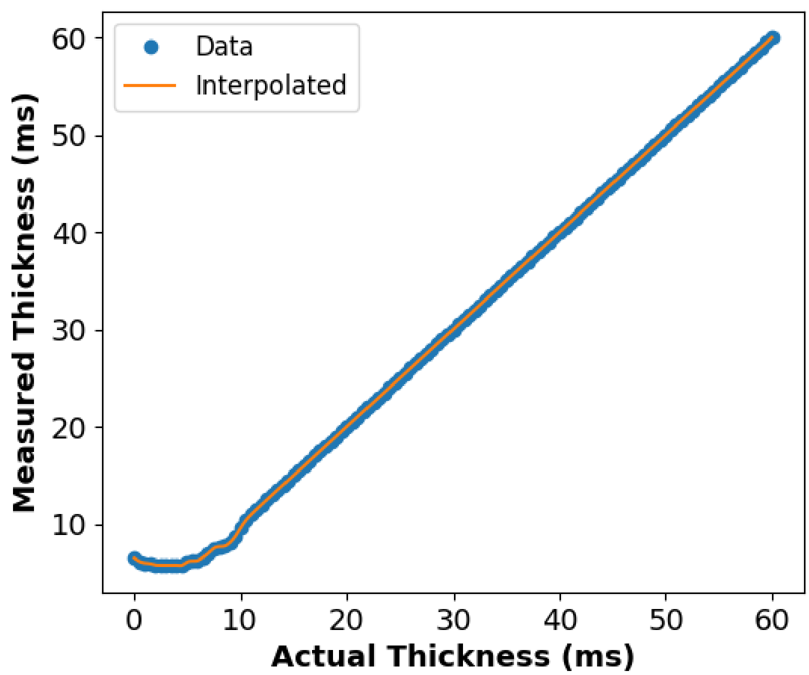

Figure 3.15: Shows the thicknesses and the interpolated thickness values for Hardens1.

3.7 Deterministic and Statistical Tuning Analysis

Kallweit and Wood (1982) conducted a deterministic study by convolving a Ricker wavelet with two spikes separated by varying distances. The study demonstrated that the maximum amplitude tuning time-thickness is represented by:

Equation 3.2: Maximum amplitude tuning thickness

$$\frac{b}{2} = \frac{1}{2.6 f_p} = \frac{\lambda_d}{4}$$

Where b is the trough-to-trough breadth of the wavelet's main lobe, f_p is the peak frequency (with the highest amplitude), and λ_d is the dominant wavelength.

This study utilizes a data-driven approach that considers both reservoir properties and amplitude tuning effects, which helps to avoid calibration difficulties introduced by the arbitrary nature of amplitude scale and the exclusion of reservoir properties in deterministic approaches. A wavelet extracted from the 3D seismic was used for identifying a deterministic tuning time-thickness and a side lobe (A_s), main lobe (A_m), amplitude ratio.

As Brown (Brown, 1999) advocated, composite seismic attributes from target zones were utilized due to their ability to amplify reservoir-related effects while suppressing the contribution of the surrounding material due to the approximate proportionality between the top and bottom of the reflections (Fig. 3.16). For the Viola Limestone, when the thickness is one-quarter of the dominant wavelength, there is an overlapping of the top reflection energy from the main central lobe with the bottom reflection energy from the side lobe, resulting in an opposite polarity case. Two factors were assumed to contribute to the lateral variability in composite amplitudes of the target zone:

a) Tuning effects result from the reflection of seismic attributes from the reservoir zone, where thicknesses are less than one period ≈ 20ms.

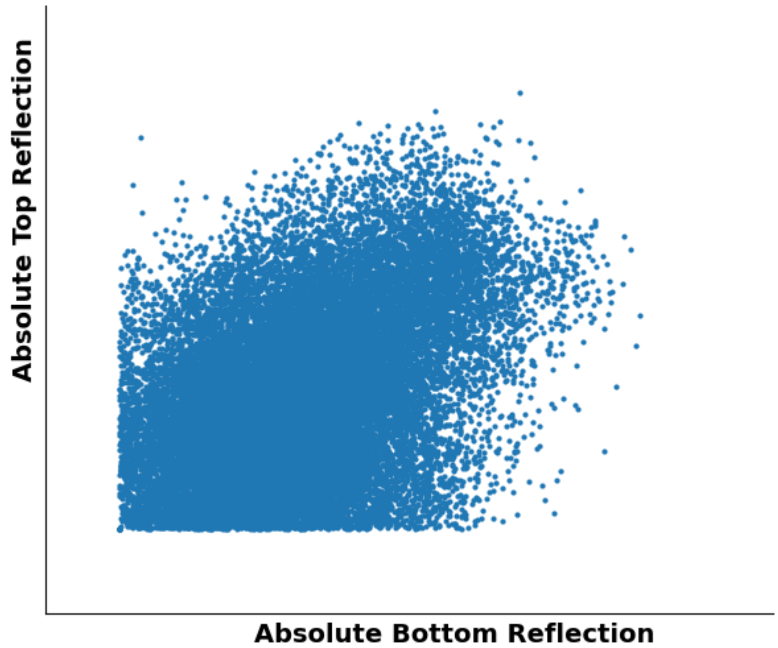

Figure 3.16: Cross-plot of the base amplitudes of the Viola Limestone against its top amplitudes demonstrating approximate proportionality.

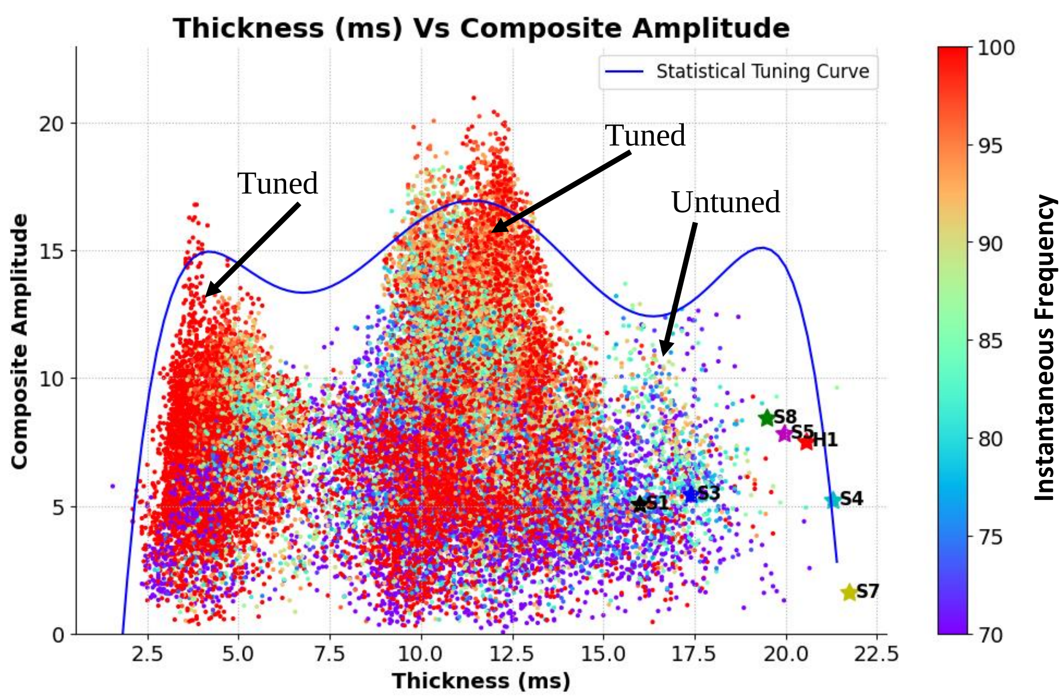

Figure 3.17: Cross-plot of the composite amplitude of the seismic horizons against the Isochrone thickness (ms) colored by the instantaneous frequency.

b) Lateral changes in reservoir properties provided that the acoustic impedance in the encasing beds is stable and the 3D-seismic data has undergone amplitude preservation processing.

The composite amplitude of the reservoir was divided into three sets based on the type of variability content: untuned sets (thickness greater than the extracted wavelet length), tuned sets (highest 15% of analyzed data), and global sets (overall variability).

Regression was performed on each group to establish variability, statistical tuning, calibrating, and global variability trends. Linear trend lines, L1 and L2, were fitted to the untuned and global sets. L1 represents the average amplitude-variability of thickness, excluding tuning geometrical contributions, while L2 represents the average amplitude-variability of thickness, including both tuning and petrophysical properties.

We established a baseline to determine the tuning error for each time-thickness. A statistical tuning curve (Fig. 3.17) was created by fitting a polynomial to the tuned set, which includes and enhances tuning variability. Deterministic tuning curve points were also obtained from the wedge models generated for each of the well. This same method was applied to other seismic attributes, such as the instantaneous frequency.

3.8 Mineral Composition Profile

Doveton's (2017) calculator was employed, which provides an apparent density and bulk photoelectric absorption for the mineral matrix. Using these variables, percentages were calculated for Quartz (Chert), Dolomite, and Calcite (Limestone) at each depth along a log curve to understand the changes in the seismic response with lithology. The necessary inputs are density porosity (*DPHI*), neutron porosity (*NPHI*), both in equivalent limestone fractional units, bulk density (*RHOB*) and photoelectric factor (*PE*). To eliminate the effect of porosity, the average of the density and neutron porosity logs were used to estimate the volume of porosity:

Equation 3.3: Volume of porosity

$$phi = {}^{(DPHI + NPHI)}\!/_{2}$$

The bulk photoelectric absorption (*U*) is calculated by converting the photoelectric factor log (*PE*) from barns per electron (b/e) to barns per cubic centimeters (b/cc):

Equation 3.4: Bulk photoelectric absorption (U)

$$U = PE * RHOB$$

The bulk photoelectric absorption of the mineral matrix (*Umaa*) is calculated from the estimated volume of porosity, bulk photoelectric absorption (*U*), and the photoelectric absorption of the mud filtrate (U_f):

Equation 3.5: Bulk photoelectric absorption of mineral matrix (Umaa)

$$U_{maa} = {}^{(U - phi * U_f)}\!/_{(1 - phi)}$$

RHOmaa is the estimate of the density of the mineral matrix recorded in grams per cubic centimeter (gm/cc):

Equation 3.6: Density of the mineral matrix (RHOmaa)

$$RHO_{maa} = {}^{\left(RHOB - phi *\ RHO_f\right)}\!/_{(1 - phi)}$$

Where RHO_f is the density of water in the pore spaces, which will most likely be the density of the mud filtrate.

A composition profile technique was used to identify the vertical distribution of lithofacies. This approach leverages the mineral-specific information encoded in RHOmaa and

Umaa values to estimate their relative proportions at each depth, generating a continuous picture of rock composition within the wellbore. The conventional RHOmaa-Umaa chart (Fig. 3.18), mainly utilized by logging companies, was used, which agrees with the geology of the study area having limestone (Calcite), Quartz, and Dolomite. Mineral profiles were created by transforming RHOmaa and Umaa values into estimated mineral proportions at each depth.

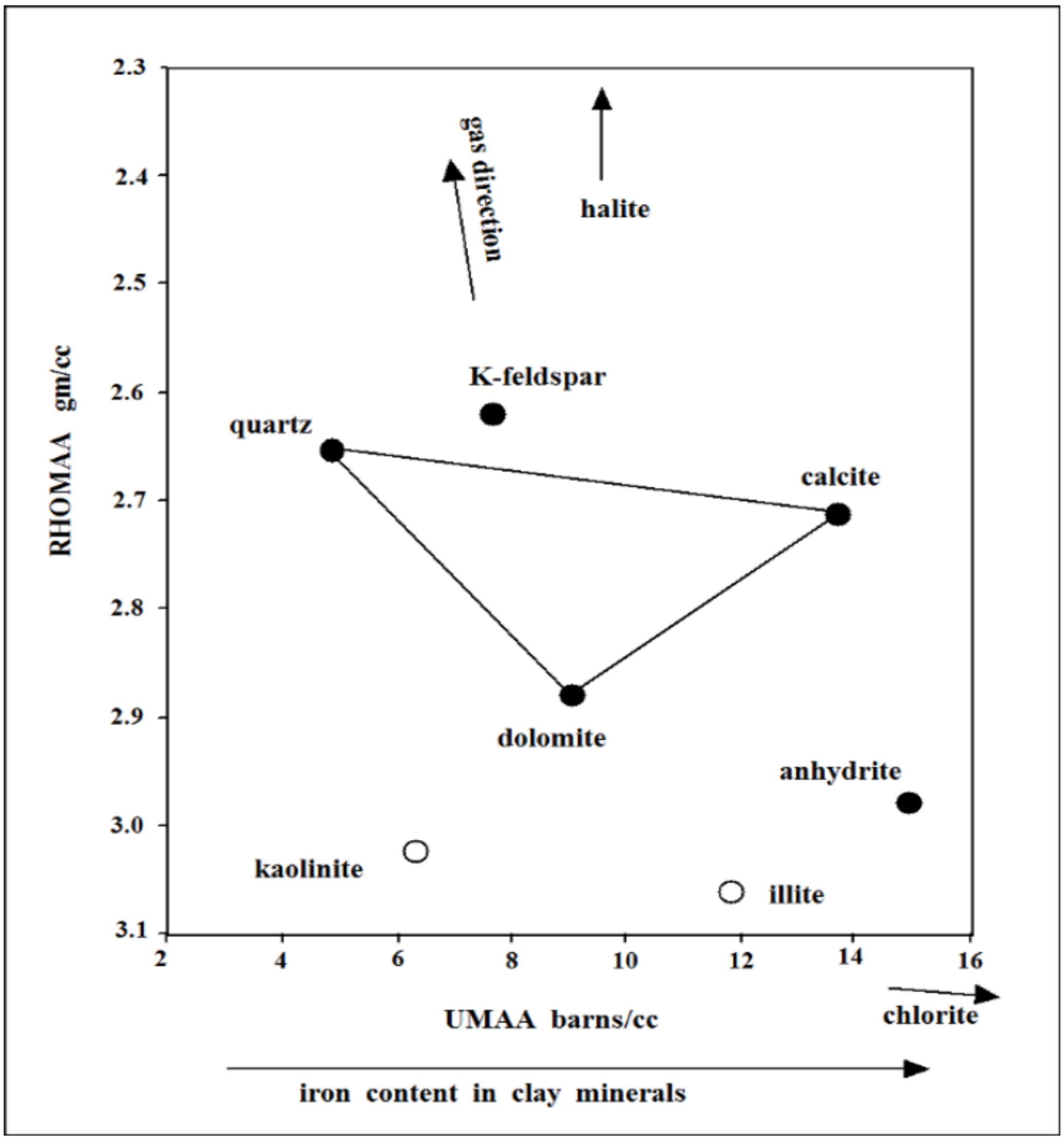

Figure 3.18: RHOmaa-Umaa chart shows the basic plan of the crossplot found in logging service company chartbooks.

The coordinates of each point on the RHOmaa-Umaa crossplot (Fig. 3.19), representing a specific depth, are fed into a predefined equation below that considers the known properties of Quartz, Calcite, and Dolomite.

Equation 3.7: Mineral composition profile equation (Python code)

$$[Mineral\ Proportions] = C^{-1} \times [RHOmaa,\ Umaa]$$

$[Mineral\ Proportions]$ is a column vector containing the estimated proportions of Quartz (chert), Dolomite, and Calcite at a specific depth. C^{-1} is the inverse of the coefficient matrix. $[RHOmaa,\ Umaa]$ is a row vector containing the RHOmaa and Umaa values for that depth. This equation, encoded in a coefficient matrix, essentially decodes the crossplot point into its corresponding mineral proportions. Since these three minerals make up a "closed system" ("summing to unity"), only two log variables (RHOmaa and Umaa) are needed to solve for three unknowns (mineral proportions). The sonic log was also included in the mineral composition profile (Fig. 3.20) to understand the change in velocity due to mineralogy (lithology). The change in velocity translates to changes in seismic amplitude and thus helps distinguish amplitude anomalies from changes in lithology to anomalies due to seismic tuning. We generate a dynamic composition profile by applying this method to all depths in the wellbore using the detailed steps below.

Step 1: Define inputs from RHOmaa crossplot at a depth calculated from the well logs.

- Imagine a point on the RHOmaa-Umaa crossplot with RHOmaa = 2.7 g/cc and Umaa = 0.6 barns/cc

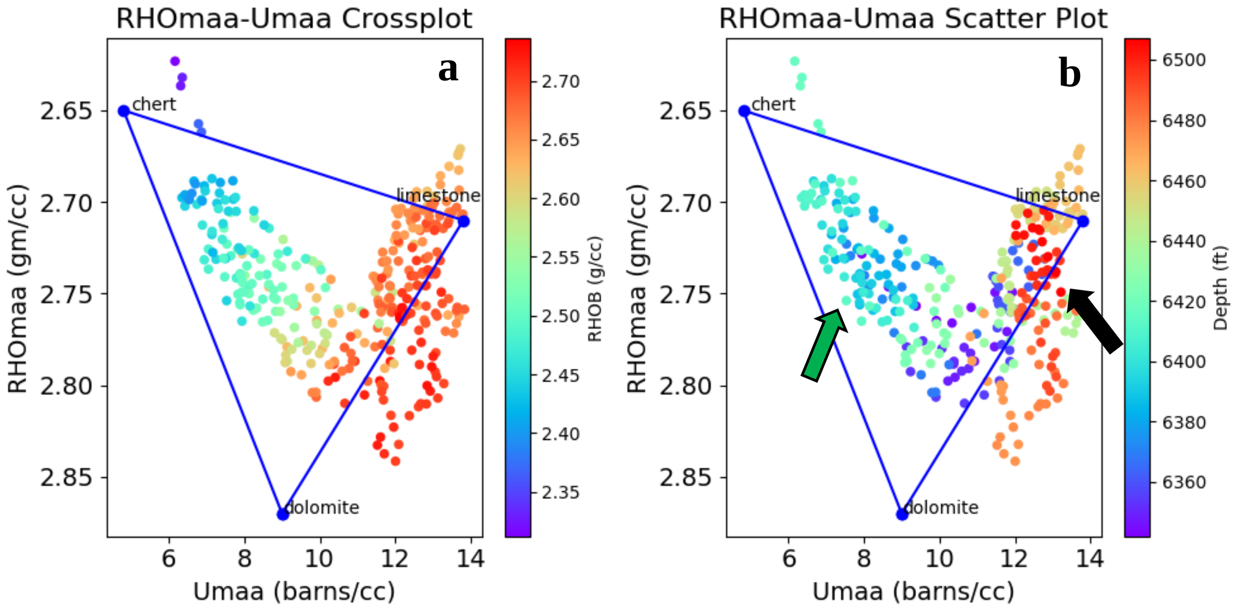

Figure 3.19: Cross-plot of RHOmaa-Umaa values for Stephens8 (S8) colored by the density(a) and the reservoir depth (b) interval. The shallow part (green arrow) of the Viola reservoir for S8 consist majorly of Cherty dolomite (Quartz & Dolomite) while the deeper part (black arrow) consists mainly of Limestone (Calcite).

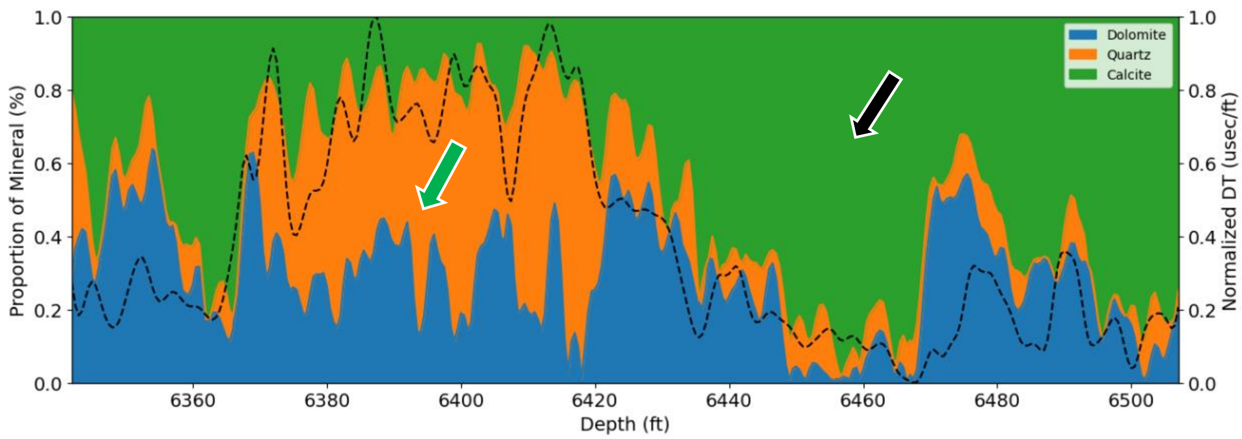

Figure 3.20: Mineral composition profile for Stephens8 (S8) at the reservoir depth interval of interest. The black dashed line is the sonic log, which shows how velocity varies with lithology.

- We have the predefined coefficient matrix below (Table 3.1) for Dolomite, Quartz, and Calcite.

Table 3.1: RHOmaa and Umaa values for the three minerals as a coefficient matrix "C"

Mineral	RHOmaa fraction	Umaa fraction	Unity
Dolomite	2.87	9	1
Quartz	2.65	4.8	1
Calcite	2.71	13.8	1

Step 2: Matrix Multiplication

We multiply the point's RHOmaa (2.7 g/cc) and Umaa (0.6 barns/cc) values by the coefficient inverse matrix of Table 3.1.

Table 3.2: Matrix multiplication between well log (RHOmaa &Umaa) and inverse matrix

	Dolomite Fraction	Quartz Fraction	Calcite Fraction	Sum
RHOmaa	2.87 * 2.7	2.65 * 2.7	2.71 * 2.7	22.22
Umaa	9 * 0.6	4.8 * 0.6	13.8 * 0.6	16.56
Sum	13.15	10.04	15.6	38.79

Step 3: Mineral Proportions (Sum & Divide)

- We calculate the mineral proportion of each mineral by their fractions (Table 3.3).

Table 3.3: Mineral Proportion

Mineral	Proportion
Dolomite	$\frac{13.15}{38.79} = 0.339$
Quartz	$\frac{10.04}{38.79} = 0.259$
Calcite	$\frac{15.6}{38.79} = 0.402$

The calculation at this specific depth implies that the estimated mineral composition is approximately 25.9% quartz, 40.2% calcite, and 33.9% dolomite. This is automated by a Python program for every depth using the calculated RHOmaa and Umaa values from the well logs.

3.9 Supervised Machine Learning for Tuning Analysis

Several machine learning models were employed in this study, ranging from simple linear regression models to complex algorithms like XGBoost. Gradient boosting, random forest, and XGBoost provided promising results and thus became the focus of this study. The machine learning workflow (Fig. 3.21) shows the step-by-step process of building the machine learning models.

The seismic attributes extracted from the seismic horizons and the isochron (thickness) were used as input features, and the maximum tuning errors obtained from the statistical and wedge model approaches were utilized as target labels. The input features were cleaned and processed to handle missing values and outliers. Exploratory data analysis was carried out to identify input features responsive to thin layers. The strength and direction of association between the seismic attributes were established using the Spearman correlation, which also captures nonlinear relationships and is valuable when features are not normally distributed.

The dataset was split randomly into training, validation, and test sets. 20% of the dataset was used for testing, while the remaining 80% was used for training and validation. Gradient boosting, random forest, and XGBoost models were built, and their performances were assessed using metrics like the mean square error (MSE) and the R-squared. Hyperparameters were tuned, and selected input features were adjusted based on the validation results. The details of each of the algorithms are described below.

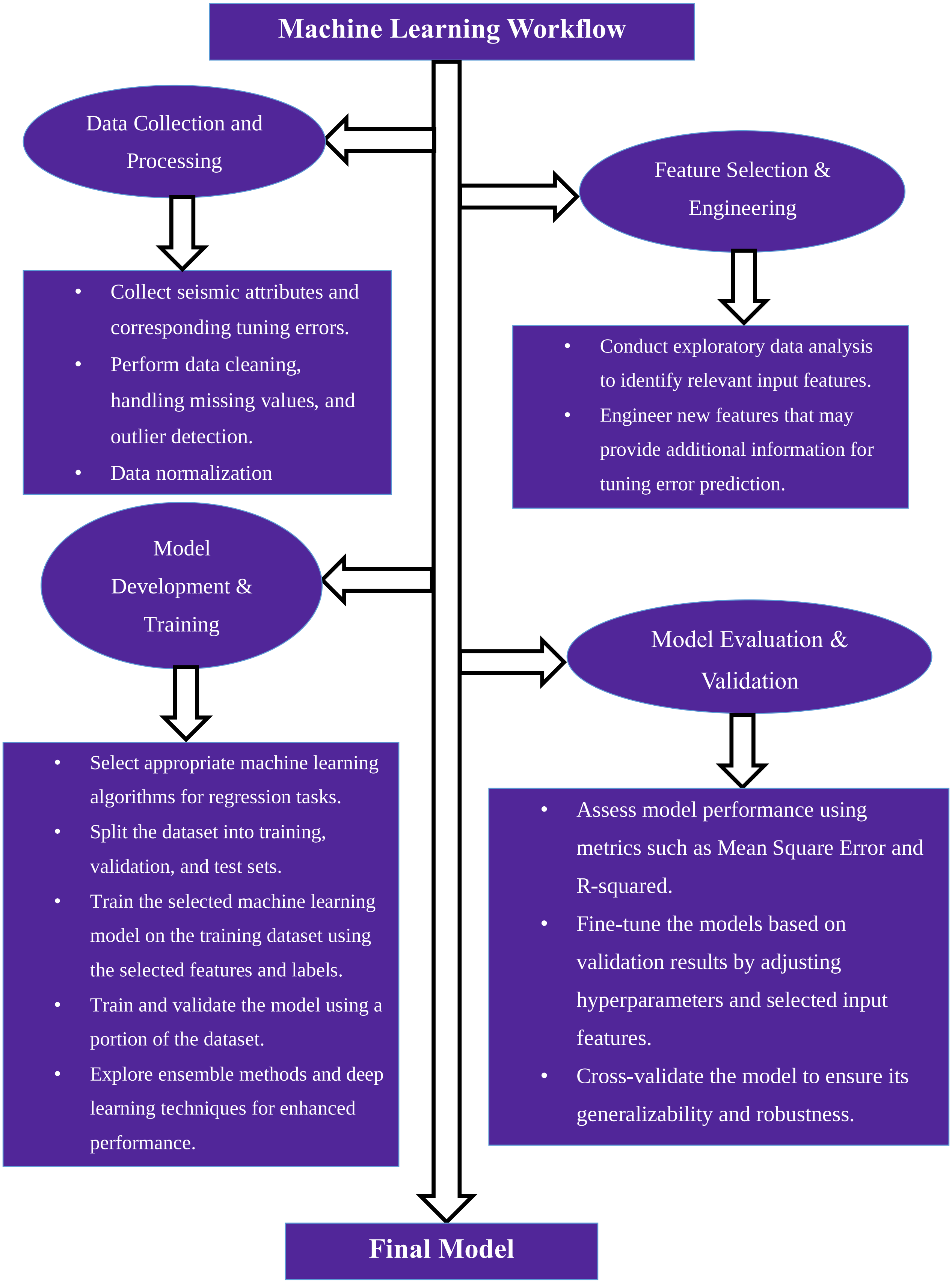

Figure 3.21: Supervised machine learning workflow for maximum tuning error prediction.

Gradient Boosting

Gradient Boosting is a powerful machine learning technique that builds a predictive model by combining the strengths of multiple weak learners, typically decision trees. It works iteratively, each tree correcting errors made by the previous ones, resulting in a robust and accurate ensemble model. Gradient Boosting excels in capturing complex relationships within data and is widely used in predictive modeling. (Friedman, 2001) introduced the concept of gradient boosting and described the gradient boosting algorithm as a method for approximating arbitrary smooth functions by an additive expansion of simple functions. The algorithm can be described mathematically as follows:

Equation 3.8: Gradient boosting algorithm

1. Initialize the model with a constant value:

$$F_{0(x)} = \underset{\gamma}{\operatorname{argmin}} \sum_{i=1}^{n} L(y_i, \gamma)$$

2. For $m = 1\ to\ M$:

2-1. Compute residuals $\gamma_{im} = -\left[\frac{\partial L\left(y_i, F(x_i)\right)}{\partial F(x_i)}\right]_{F(x)=F_{m-1}(x)} \quad for\ i = 1, \ldots, n$

2-2. Train regression tree with features x against γ and create terminal nodes $R_{jm}\ for\ j = 1, \ldots, J_m$

2-3. Compute $\gamma_{jm} = \underset{\gamma}{\operatorname{argmin}} \sum_{x_i \in R_{jm}} L(y_i, F_{m-1}(x_i) + \gamma)\ \ for\ j = 1, \ldots, J_m$

2-4. Update the model:

$$F_m(x) = F_{m-1}(x) + v \sum_{j=1}^{J_m} \gamma_{jm} 1\left(x \in R_{jm}\right)$$

The first step initializes the model with a constant value prediction F_0, usually the mean of the target variable y. $argmin$ executes the search for the value γ that minimizes $\sum L(y_i, \gamma)$.

Step two is iterated M times. Where M represents the number of trees created and m denotes the index of each tree.

For every iteration (boosting round), the model fits a weak learner (decision tree) to the negative gradient of the loss function with respect to the current model predictions (Fig. 3.22). This step aims to minimize the loss function by moving in the direction that reduces the error. The next step (2-4) updates the model by adding the output of a weak learner multiplied by a learning rate (v) to the current model. Step 2 is repeated until a predefined number of iterations is reached or until the loss function's improvement becomes negligible.

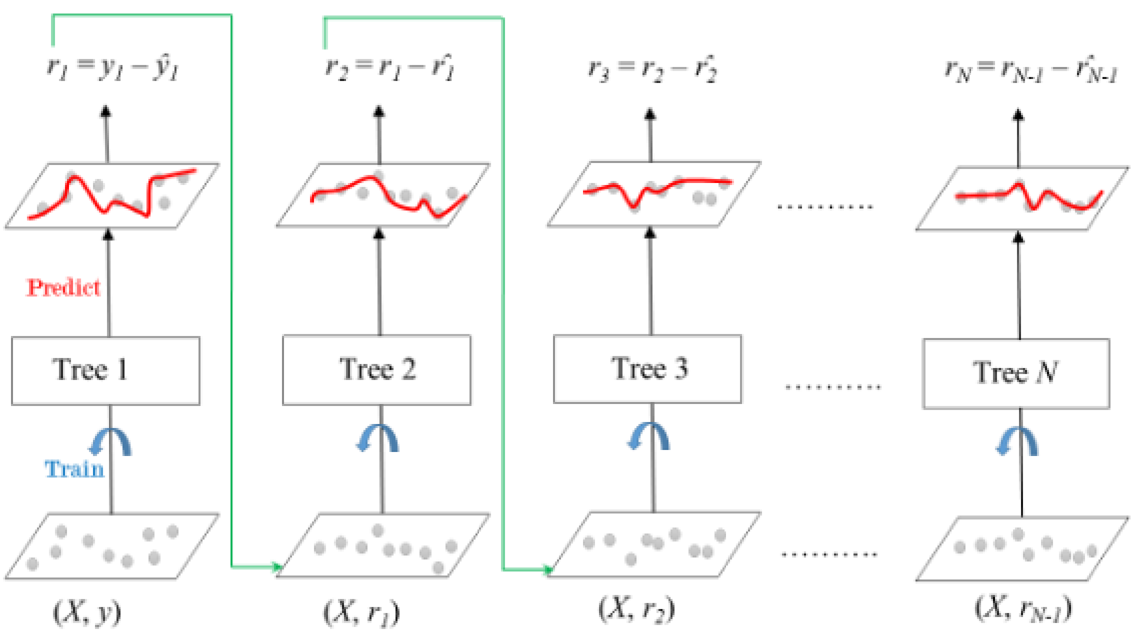

Figure 3.22: Gradient boosted trees for regression (geeksforgeeks.org)

Random Forest

Random Forest is a versatile machine learning algorithm renowned for its robust performance in predictive modeling. It constructs an ensemble of decision trees and leverages their collective predictions to enhance accuracy and mitigate overfitting. Random forest adapts to handling complex relationships in diverse datasets by introducing randomness in tree-building. Random forest excels in capturing intricate patterns and delivering reliable predictions, making it a valuable tool for regression analysis. (Breiman, 2001) described the Random Forest algorithm in his paper titled "Random Forests" as a combination of tree predictors, where each tree is built using a random selection of features and a bootstrapped sample of the training data.

For this study, the Random Forest Regressor in sci-kit-learn was employed, and the bagging method was used to construct the individual decision trees. Bagging stands for Bootstrap Aggregating, and it involves training each tree on a random subset of the training data with replacement, which helps to introduce randomness and reduce overfitting. The algorithm can be described mathematically as follows:

For a regression problem, Random Forest aims to predict a continuous target variable Y from input features X.

If the training dataset $D = \{(x_1, y_1), (x_2, y_2), \ldots, (x_n, y_n)\}$, where x_i denotes the input feature vector for the ith sample and y_i is the equivalent target value, the equation for averaging the predictions of individual trees is given by:

Equation 3.9: Random Forest equation for averaging predictions of individual trees

$$\hat{Y}(x_i) = \frac{1}{N} \sum_{j=1}^{N} F_j(x_i)$$

$\hat{Y}(x_i)$ denotes the predicted value for the ith sample.

N is the total number of trees in the Random Forest.

$F_j(x_i)$ is the prediction of the jth sample x_i.

Bootstrapped sampling randomly selects n samples with replacement from the original dataset to generate multiple bootstrap samples where each sample serves as the training set for a decision tree (Fig. 3.23). At every node of the decision tree, a subset of features (typically denoted as m where m "p, where p is the total number of features) is randomly selected for splitting.

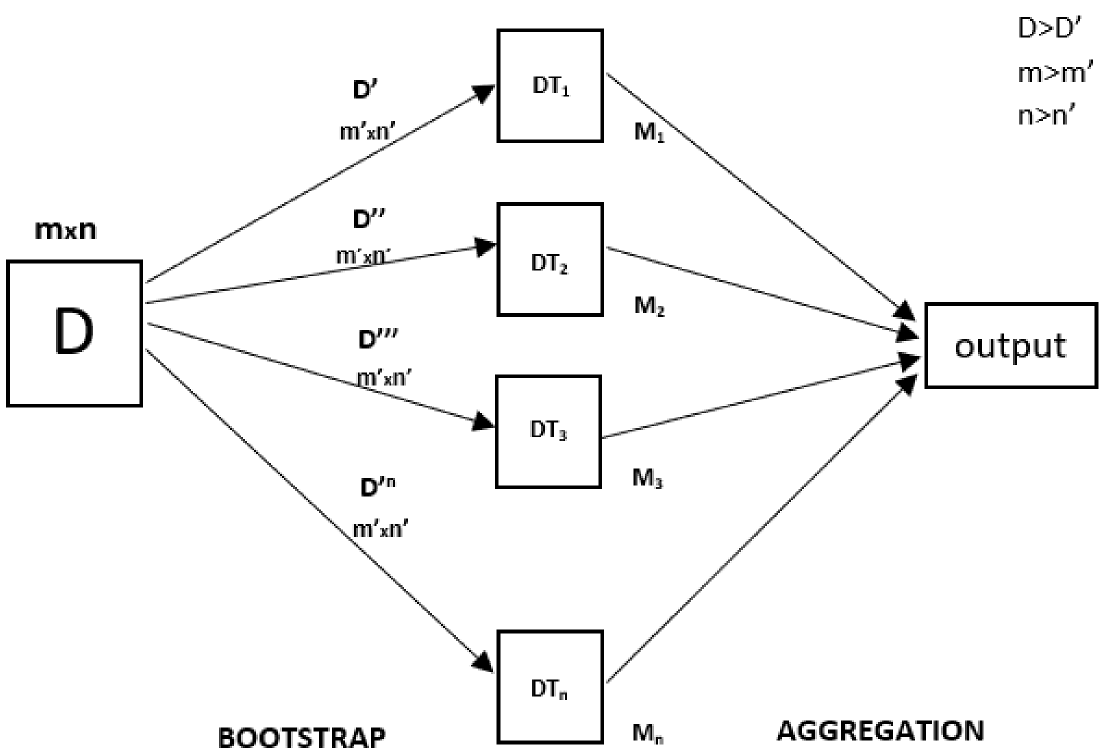

Figure 3.23: Random Forest regression architecture (geeksforgeeks.org).

This introduces variability and decorrelates the trees. Every bootstrap sample generates a tree recursively by choosing the best split at each node based on a criterion, such as minimizing the mean squared error (MSE) and then averaging the predictions of individual trees.

XGBoost

XGBoost (Extreme Gradient Boosting) is a powerful and efficient machine learning algorithm for regression problems. It operates by training multiple decision trees, each on a subset of data (Fig. 3.24). The predictions from these trees are intelligently combined to produce a robust and accurate final prediction. XGBoost is an efficient and scalable implementation of gradient boosting framework.

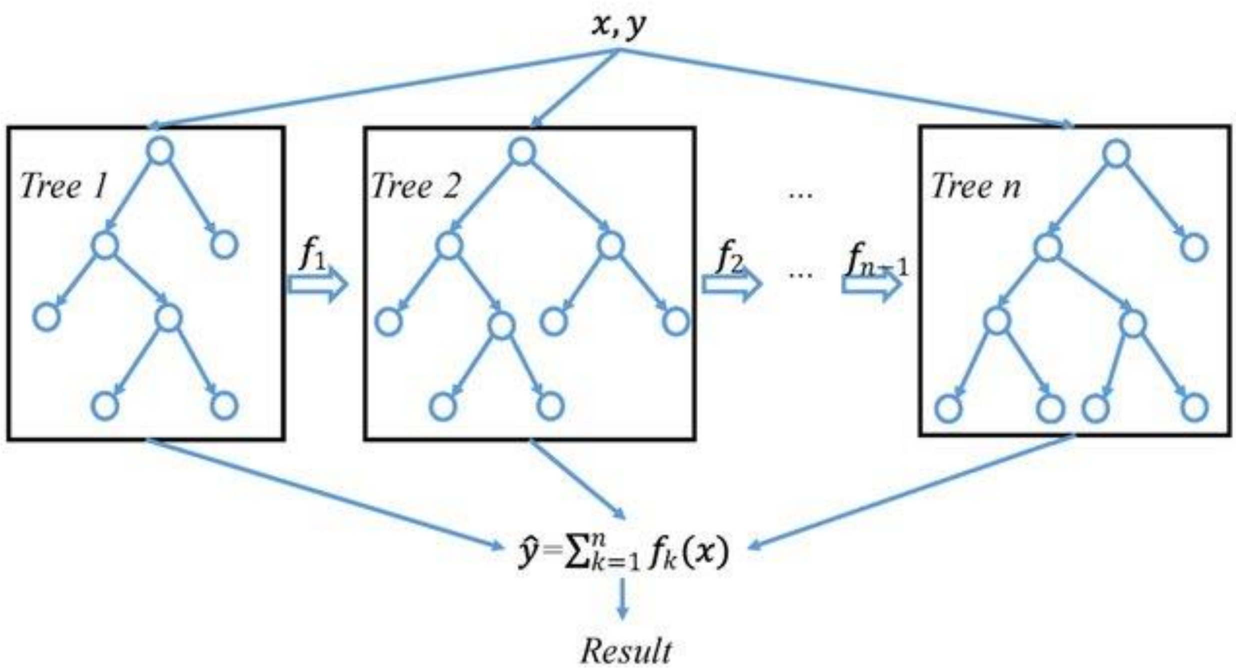

Figure 3.24: General structure of XGBoost (Kalyani et al., 2019).

The core algorithm is parallelizable; hence, it can harness the power of multi-core computers and scale to tackle big data (Chen & Guestrin, 2016). Known for its speed, accuracy, and ability to handle diverse data types, XGBoost stands out as a top choice in data-driven applications. XGBoost builds on the principles of gradient boosting, which is enhanced with regularization techniques and optimization methods. For a regression problem, XGBoost aims to learn a prediction function $F(x)$ that minimizes a regularized objective function. The objective function can be written as:

Equation 3.10: XGBoost Objective function

$$Obj = \sum_{i=1}^{n} L(y_i, \hat{y}_i) + \sum_{k=1}^{K} \Omega(f_k)$$

Where:

Obj is the overall objective to be minimized.

n is the number of training instances.

$L(y_i, \hat{y}_i)$ is a differentiable loss function that measures the errors between the predicted value $\hat{y}_i$ and the true target value y_i.

K is the number of base learners (trees) in the ensemble.

$\Omega(f_k)$ is the regularization term that penalizes the complexity of individual trees.

XGBoost searches for the best split at each node that minimizes the regularized objective function. Tree branches that do not contribute significantly to the minimization of the objective function are removed, which helps in preventing overfitting and enhances the generalizability of the model.

Chapter 4 - Results and Discussion

4.1 Synthetic Wedge Models

The wedge models demonstrated the tuning (increase and decrease) of seismic attributes within the Viola Limestone due to thickness change (Fig. 4.1 & 4.2). This helps illustrate the practical importance of studying and understanding tuning effects on the Viola Limestone. The instantaneous phase rotates from 1.5 to -1.5 as the layer thins (Fig. 4.1b). Fig 4.2b shows where the instantaneous frequencies jump or exhibit negative sign. Closely arriving reflected wavelets (tuning) causes the sign reversals (Taner, 2001). It can be used as an indicator for the onset of tuning.

The wedge models (Fig. 4.3) were obtained by varying the thickness of the wells (Stephens4 & 5) while the geology (acoustic impedance) was kept constant. The amplitude change observed is diagnostic of geometry rather than geology. The brightening and dimming can be misinterpreted as direct hydrocarbon indicators. Two peaks (P1 & P2) were observed in both wedge models with a trough in between them with an established tuning baseline. These observations are consistent with the statistical crossplot due to the influence of the average wavelet. The peaks, trough, tuning baseline, and the original thickness of the reservoir were extracted, rescaled, and plotted on the statistical crossplot as deterministic tuning points (Fig. 4.4). Beyond the tuning thickness, the main trough lobe of the viola bottom starts to interfere destructively with the main peak lobe of the viola top by causing dimming. Knowing which part of the curve the reservoir of interest is located helped in deciding where to add or remove the tuning error.

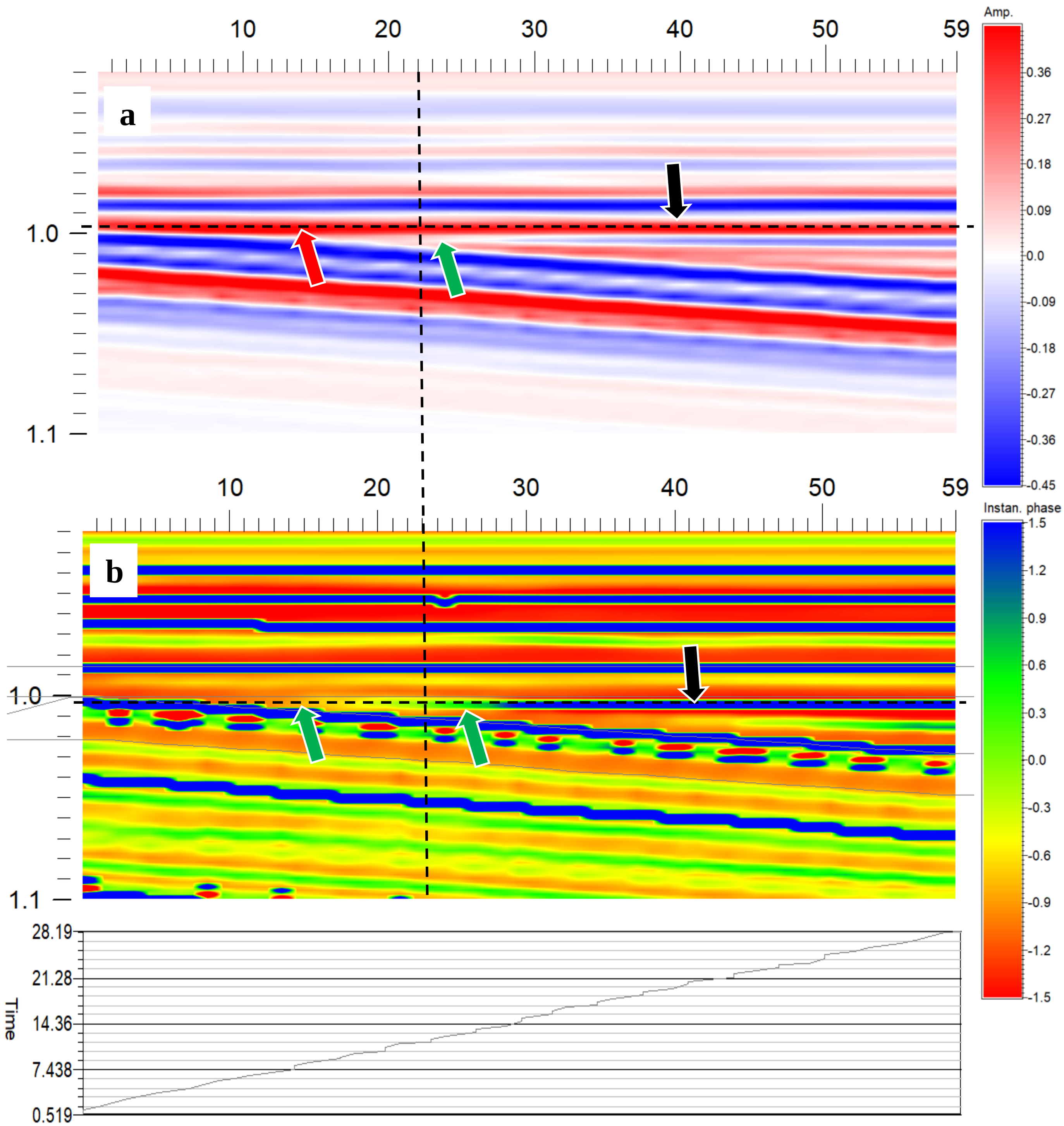

Figure 4.1: Wedge models show the change in seismic response of the amplitude (a) and instantaneous phase (b) at or below tuning, indicated by the vertical dashed lines. The time thickness (c) ranges from 0.5ms to about 28ms. The increase (red arrow), decrease (green arrow) of the seismic response and the Viola top (black arrow) are highlighted.

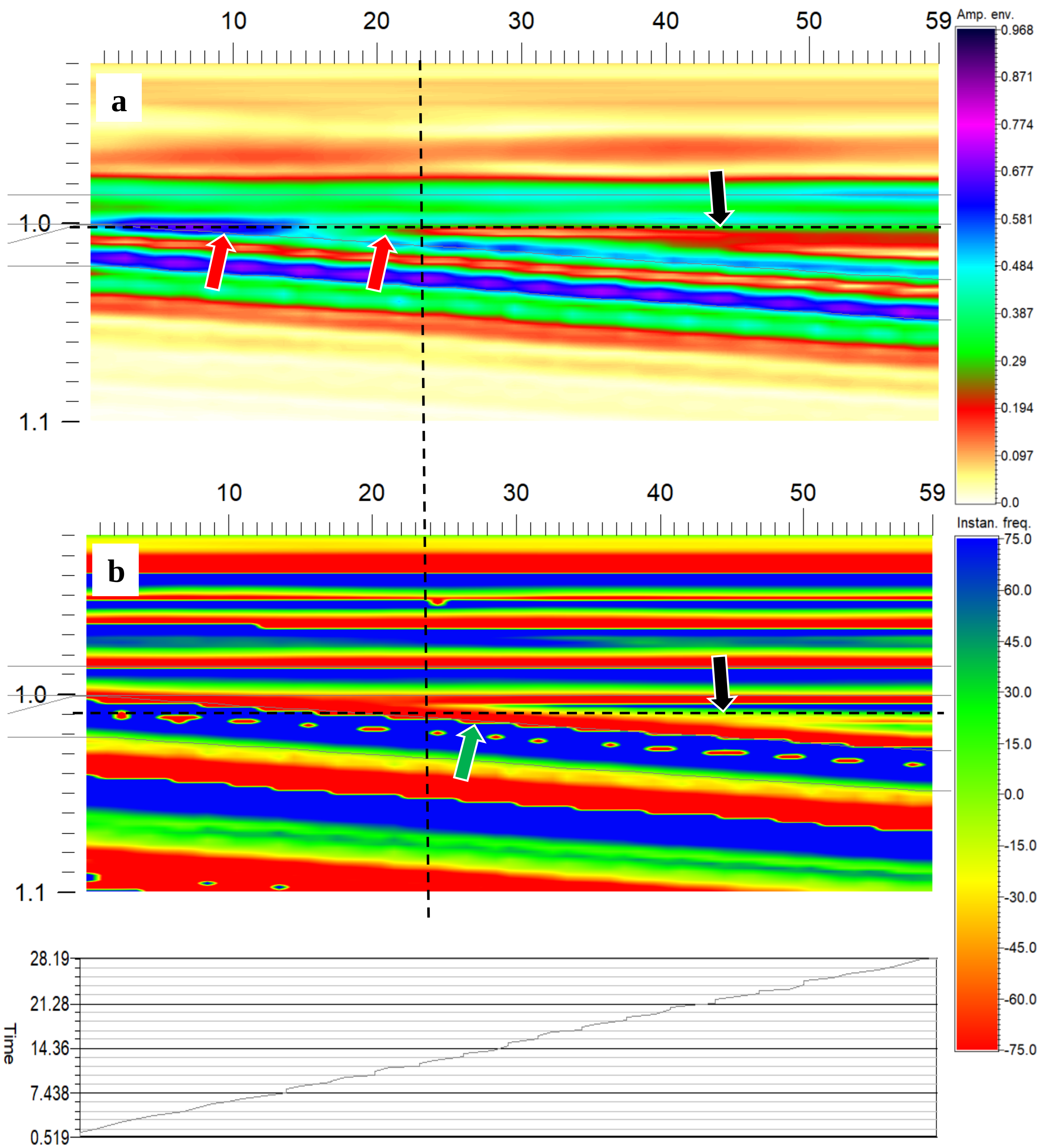

Figure 4.2: Wedge models show the change in seismic response of the amplitude envelope (a) and instantaneous frequency (b) at or below tuning, indicated by the vertical dashed lines. The time thickness (c) ranges from 0.5ms to about 28ms. The increase (red arrow), decrease (green arrow) of the seismic response and the Viola top (black arrow) are highlighted.

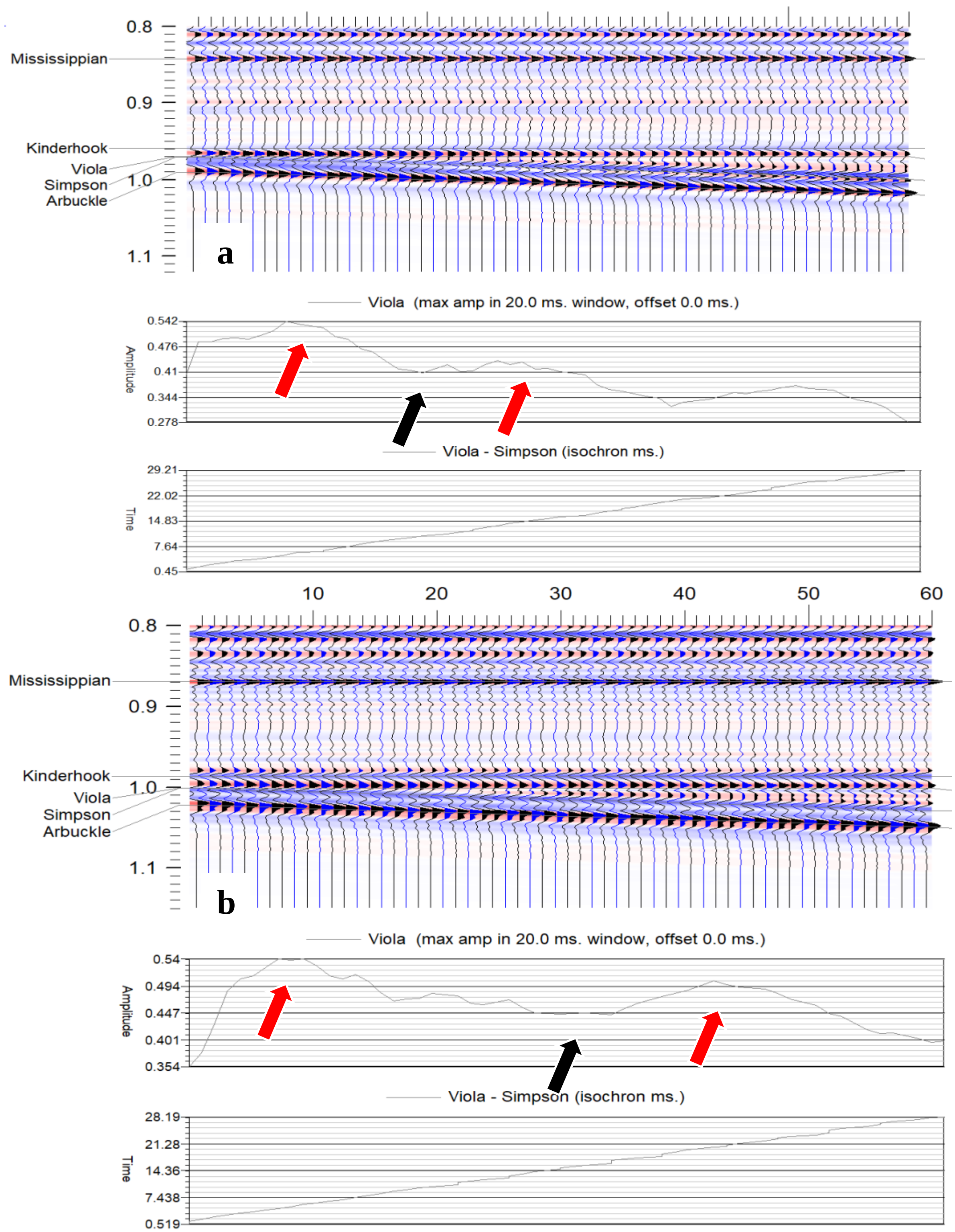

Figure 4.3: Wedge models for Stephens4 (A) and Stephens5 (B) and their corresponding amplitudes extracted from the viola top in a 20ms window. The isochron displays the time thickness (ms). Peaks (red arrows) and trough (black arrow) are highlighted.

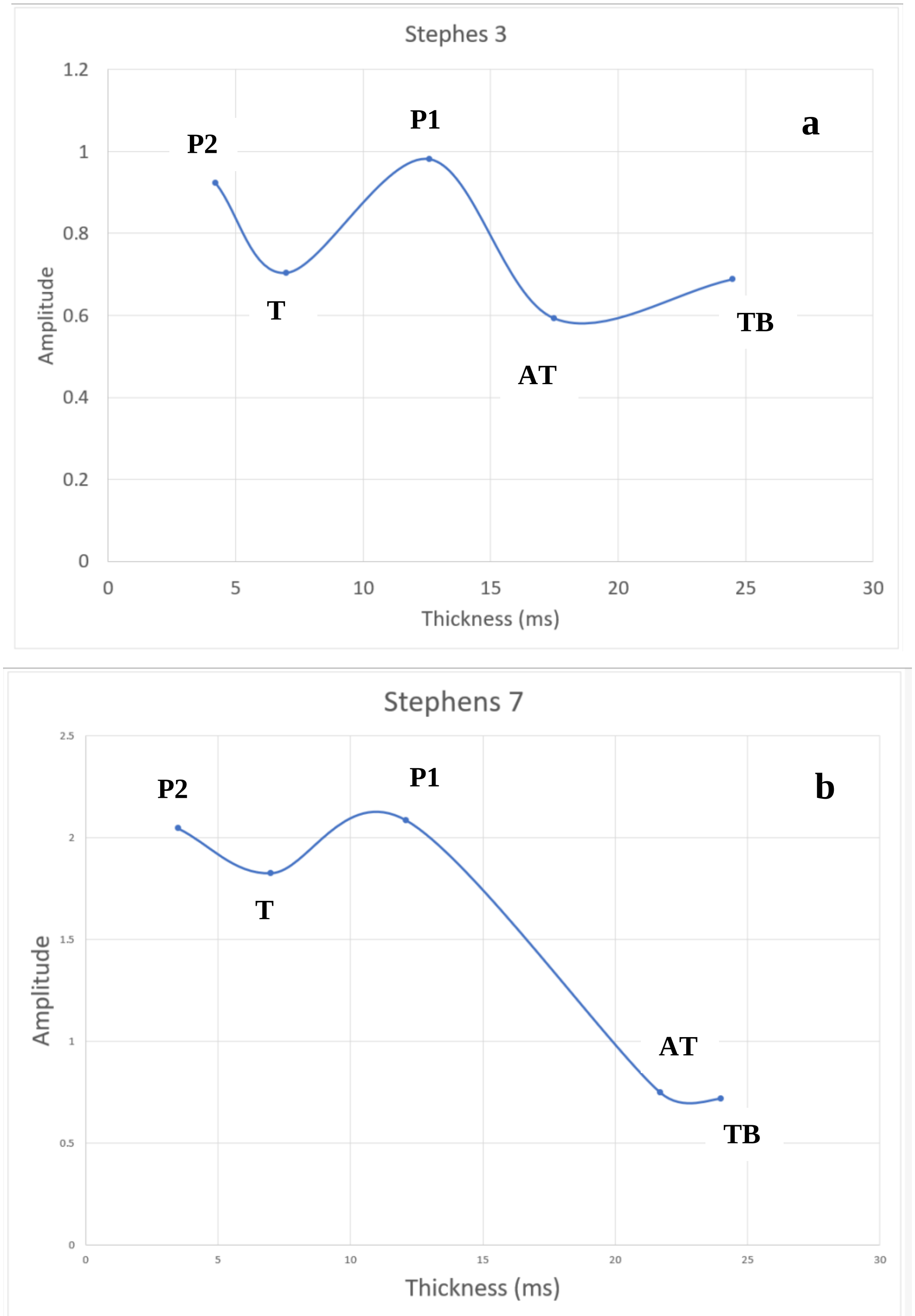

Figure 4.4: Deterministic tuning points for Stephens3 (a) and Stephens7 (b). The peaks (P1 & P2), trough (T), tuning baseline (TB), and the actual thickness (AT) of the reservoir were extracted for all the wells.

4.2 Composite Amplitude Cross plots

Two peaks were observed in the cross plot (Fig. 4.5a), which is consistent with the result of the wedge models (Fig. 4.3) because the extracted wavelet from the seismic data is complex and has several side lobes. P1 is due to interference by the first side lobe (S1), which has a larger magnitude, while P2 corresponds to interference by the second side lobe (S2).

These peaks also correspond to high instantaneous frequency (red colors), demonstrating that the instantaneous frequency is responsive to tuning (peaks with tuning). Also, tuning is not prevalent in thicknesses greater than 15.8ms.

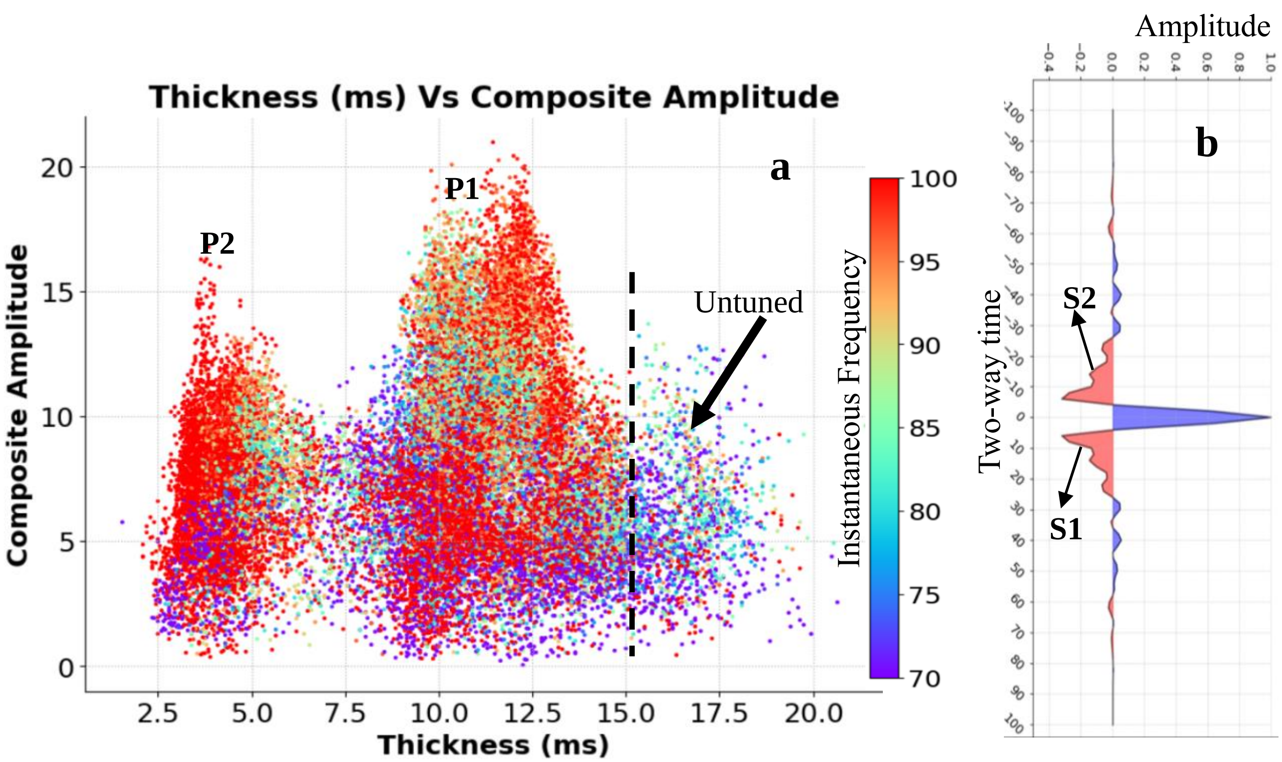

Figure 4.5: A cross-plot of the composite amplitude of the seismic horizons vs. thickness (ms) colored by the instantaneous frequency attribute. (b) Extracted wavelet from the seismic.

4.3 Statistical and Deterministic Tuning Analysis

The number of peaks and troughs caused by interference in the tuning curve (Fig. 4.6) demonstrates the number of side lobes of the seismic wavelet (Fig. 4.5b). At thicknesses greater than 10ms, the actual thickness of the thin reservoir corresponds to the measured thickness by the seismic until tuning effects begin. Below 10ms, the thickness is underestimated and later overestimated by the seismic. Thus, correcting for tuning on the reservoir thickness is crucial to avoid errors in reserve estimations.

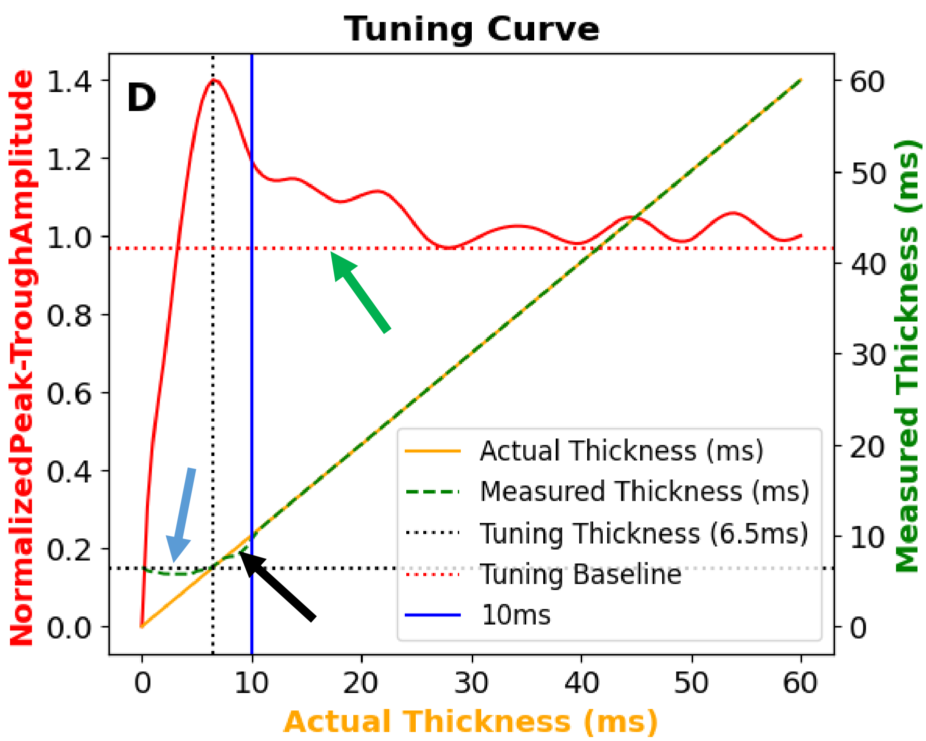

Figure 4.6: Deterministic tuning curve modeled with the average wavelet extracted from the seismic. Shows the underestimation (black arrow) and overestimation (blue arrow) of thickness beyond tuning. The amplitude abruptly deviates from the baseline (green arrow) with tuning.

The deterministic tuning time-thickness ($\frac{b}{2}$) was estimated from the extracted seismic wavelet with a trough-to-trough breadth of 12ms to be 6ms, which approximately corresponds to the tuning thickness of the tuning curve (Fig. 4.6) of 6.5ms. Figure 4.7 illustrates the deterministic tuning curve points and the statistical curve superimposed on the same cross-plots. The deterministic tuning curve points for a specific well share similar colors, while the discrepancies between tuning curve points for different wells arise from the variation in the characteristics of the wavelets extracted from the seismic data around each well used to generate the wedge models.

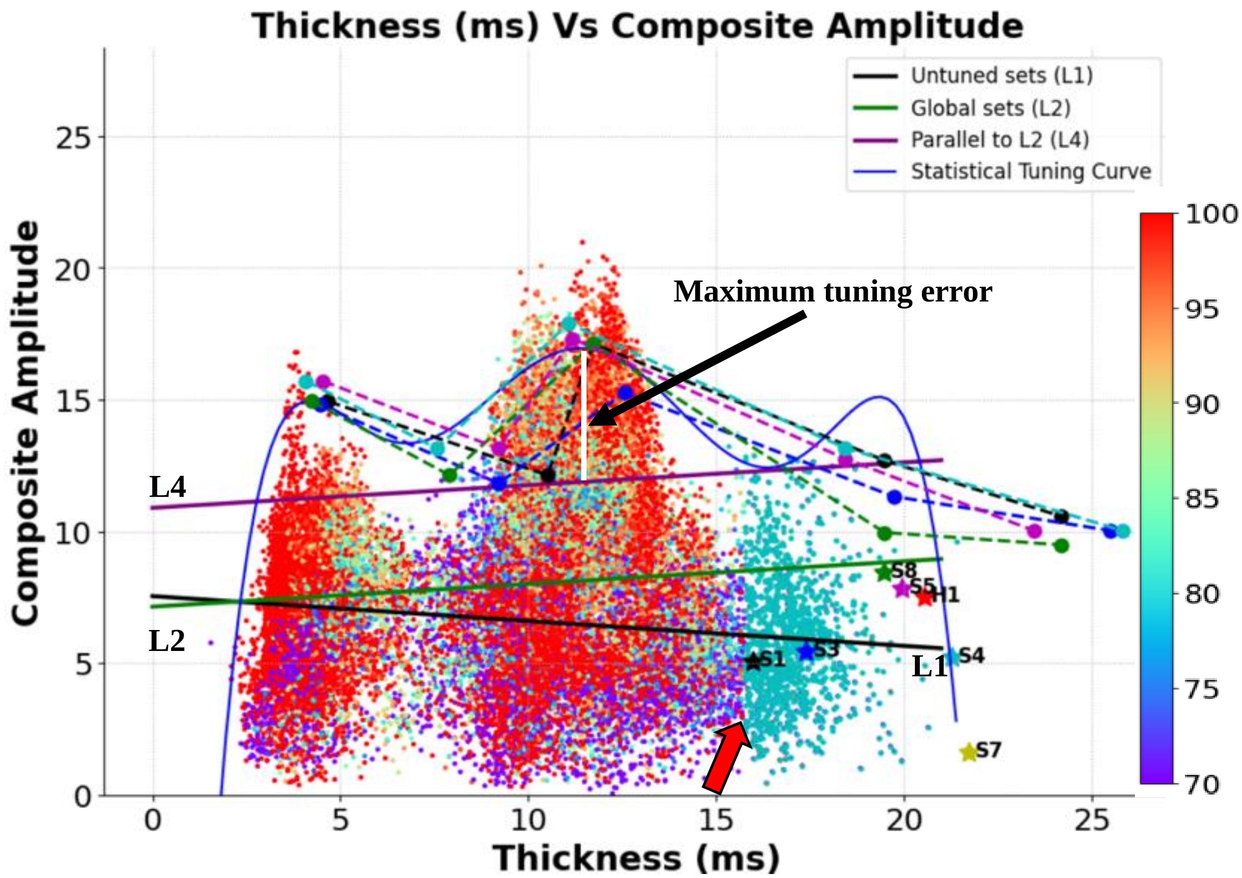

Figure 4.7: Composite amplitude cross plot showing wells (H1, S1, S3, S4, S5, S7 & S8) with fitted trends on the global set (green trend), untuned sets (black trend), and statistical curve enveloping the tuned sets (blue curve).

The red arrow marks the boundary between the tuned (left) and untuned sets (right). The tuning-free composite amplitudes calibration set (magenta dots) were used for constructing an average calibrating trend, L1, and a best statistical curve (blue) was fitted to the statistical tuning set (extreme amplitude values of the 95th percentile). L2 is a global trend, and L4 is the tuning baseline. The maximum tuning contribution (error), calculated as the difference between the peak amplitude value of the statistical curve and the corresponding baseline value (L4), is approximately 41.6%.

$$(17-12)/_{12} \ * 100\% = 41.6\%$$

The calculated 42% maximum tuning contribution agrees with the rule-of-thumb of an expected 40% maximum increase due to tuning, Brown 1991.

4.4 Mineral Composition Profiles & Victor's (2020) Ultrasonic Measurements

Mineral composition profiles (Fig. 4.8 & 4.9) reveal the vertical distribution of key components quartz (chert), Calcite (Limestone), and Dolomite within the Viola formation. Interestingly, a consistent trend emerges across all wells: seismic velocity decreases in areas with higher concentrations of Dolomite and Chert, while it increases in regions dominated by Calcite. This observation suggests a direct link between lithology and seismic amplitude. Notably, the low velocities in cherty dolomite zones coincide with the observed low amplitudes in producing wells, solidifying this connection.

The observed trends can also be related to porosity. The decrease in velocity within the cherty dolomite zones can be attributed to increased porosity due to dolomitization by the replacement of calcium carbonate (calcite) with dolomite. Dolomite crystals have a different crystal structure and may create additional pore spaces as they replace calcite. Raef et al. (2019)

established that the primary reservoir quality control of the Viola limestone as dolomitization-induced porosity.

Significant discrepancies between sonic and ultrasonic velocity measurements can be observed due to differences in measurement frequency and environment (Fig. 4.10). Sonic logs are acquired under in-situ open-hole conditions, while ultrasonic measurements typically occur under controlled laboratory settings. Figure 4.10 illustrates the contrasting responses of these two methods. Despite the observed variability, both logs exhibit a consistent trend as they traverse the Cherty Dolomitic section (highlighted by the blue square) and the Muddy Dolomitic section (red square). This variation can be attributed to the combined effects of measurement frequency and overburden (effective) pressure.

Interestingly, both the Cherty Dolomite ("B" Zone) and Muddy Dolomite ("C" Zone) correspond to highly porous intervals within the Viola formation (Fig. 4.11), where the neutron and density porosity logs mimic the trends of both sonic and ultrasonic velocity measurements, particularly in response to high porosity values.

Notably, the ultrasonic data exhibits a more pronounced sensitivity to porosity variations than the sonic log. These findings reveal a noteworthy correlation between lower velocity and cherty dolomite zones within the Viola reservoir, indicating increased porosity. This observation strongly suggests that porosity is a pivotal factor influencing velocity within the Viola, which is contributed by the porous nature of cherty Dolomite and thus appears as low amplitudes on the detuned amplitude map.

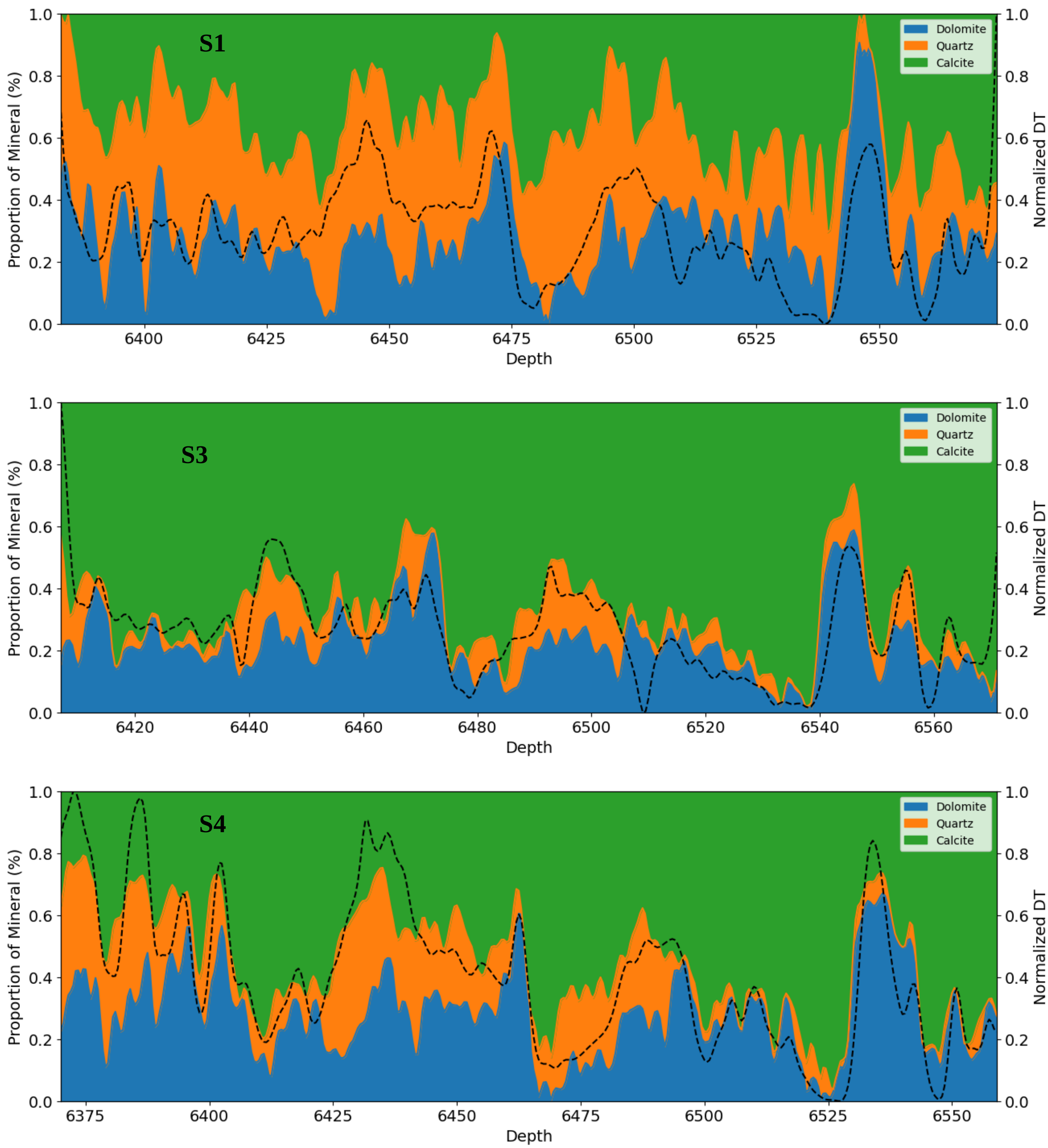

Figure 4.8: Mineral composition profile for well S1, S3, and S4 at the reservoir depth interval. The normalized sonic log (black dashed line) shows the velocity response with changing mineralogy (lithology).

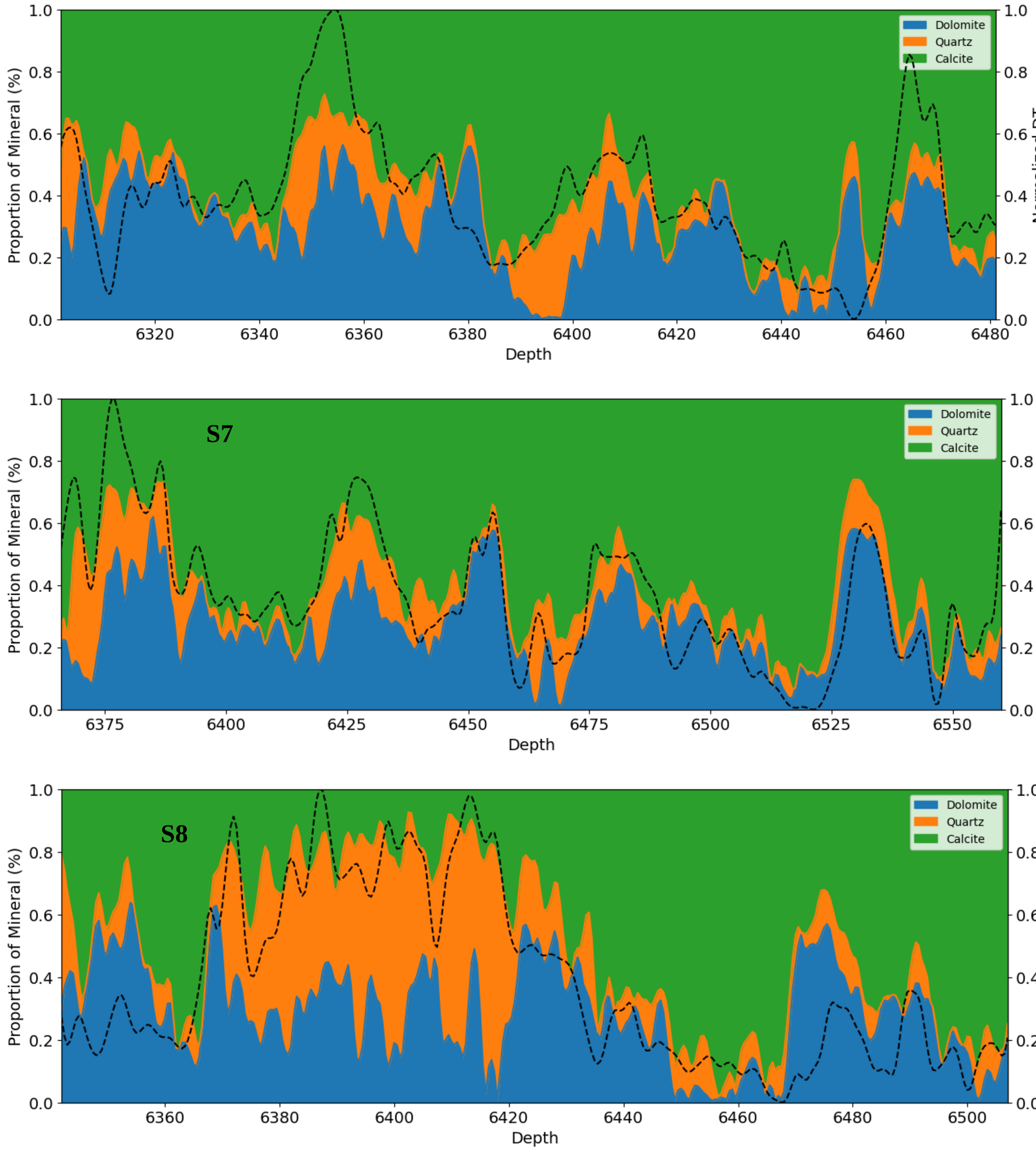

Figure 4.9: Mineral composition profile for well S5, S7, and S8 at the reservoir depth interval. The normalized sonic log (black dashed line) shows the velocity response with changing mineralogy (lithology).

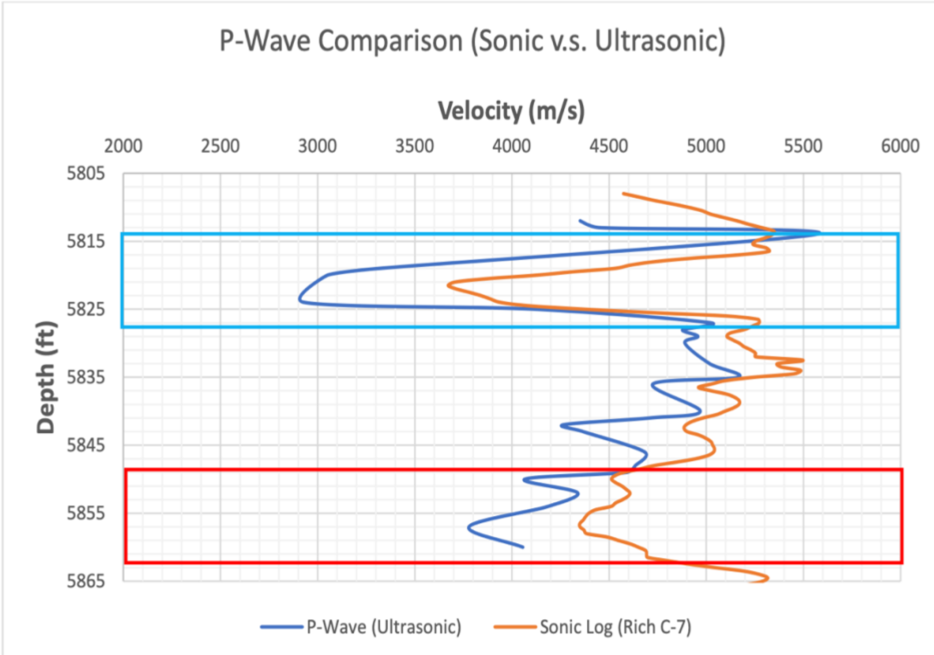

Figure 4.10: P-wave velocities are taken at sonic frequencies (wireline logging) and ultrasonic frequencies (Lab compression testing) in the Rich C-7 well and core. The blue box marks the Cherty Dolomite section, and the red one, the Muddy Dolomitic section (Victor et.al, 2020).

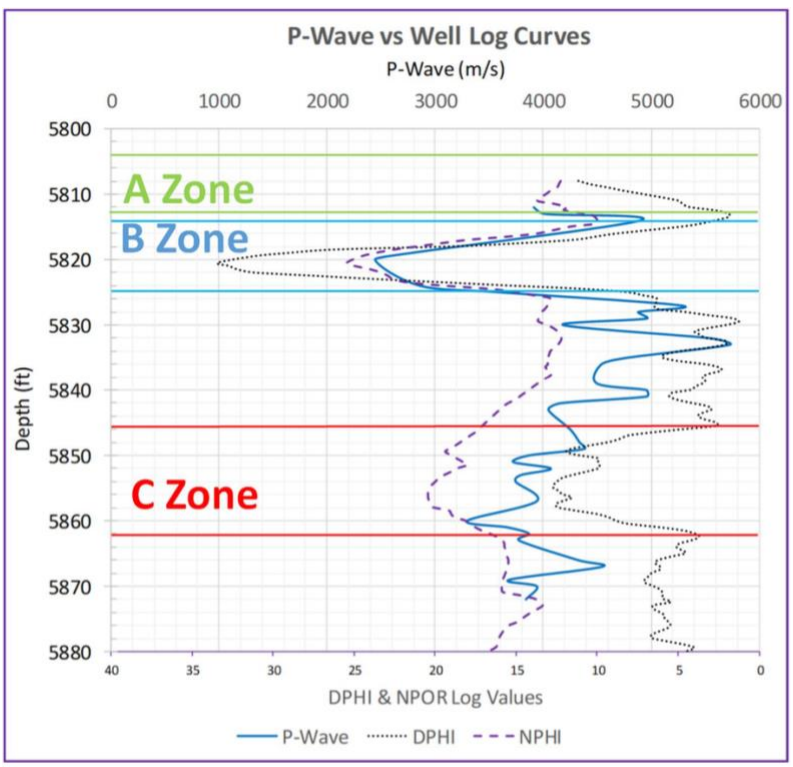

Figure 4.11: Density (DPHI) and neutron (NPHI) porosity logs compared to P-wave velocities from ultrasonic measurements obtained in the Rich C-7 Core (Victor et.al, 2020).

4.5 Amplitude Regression Analysis

The initial regression analysis (Fig. 4.12a) between compensated neutron porosity and original seismic amplitude revealed a weak and potentially non-significant relationship. The low R-squared value (0.152) suggests that the original seismic amplitude, likely containing geological and geometric information, was not an effective predictor of reservoir properties. This highlights the challenges posed by geometric effects, where variations in layer thickness can obscure the actual geological signal within the seismic response.

Using the detuned seismic amplitude (Fig. 4.12b), we observed an increase in R-squared (from 0.152 to 0.222) indicating a statistically significant but still moderate relationship with compensated neutron porosity. This improvement can be attributed to successfully removing geometric effects, allowing the detuned seismic amplitude to reflect the underlying porosity more accurately. The enhanced correlation (from -0.39 to -047) between detuned seismic amplitude and porosity highlights the effectiveness of tuning correction in mitigating the influence of thickness variations and preserving the actual geological signal.

However, it is essential to acknowledge that the overall correlation remains moderate, suggesting that the amplitude response also depends on other geological factors, such as lithology, as shown by the mineral composition profiles (Fig. 4.8 & 4.9) and porosity (Fig. 4.11).

4.6 Detuned Seismic Attributes

Seismic amplitude response provides information about geology, such as lithology, porosity, and fluid type. However, amplitude also responds to geometry (thickness), resulting in uncertainties. From the detuned amplitude map (Fig. 4.14b), Lower amplitude anomalies correlate with hydrocarbon production, while non-productive wells are associated with higher amplitudes.

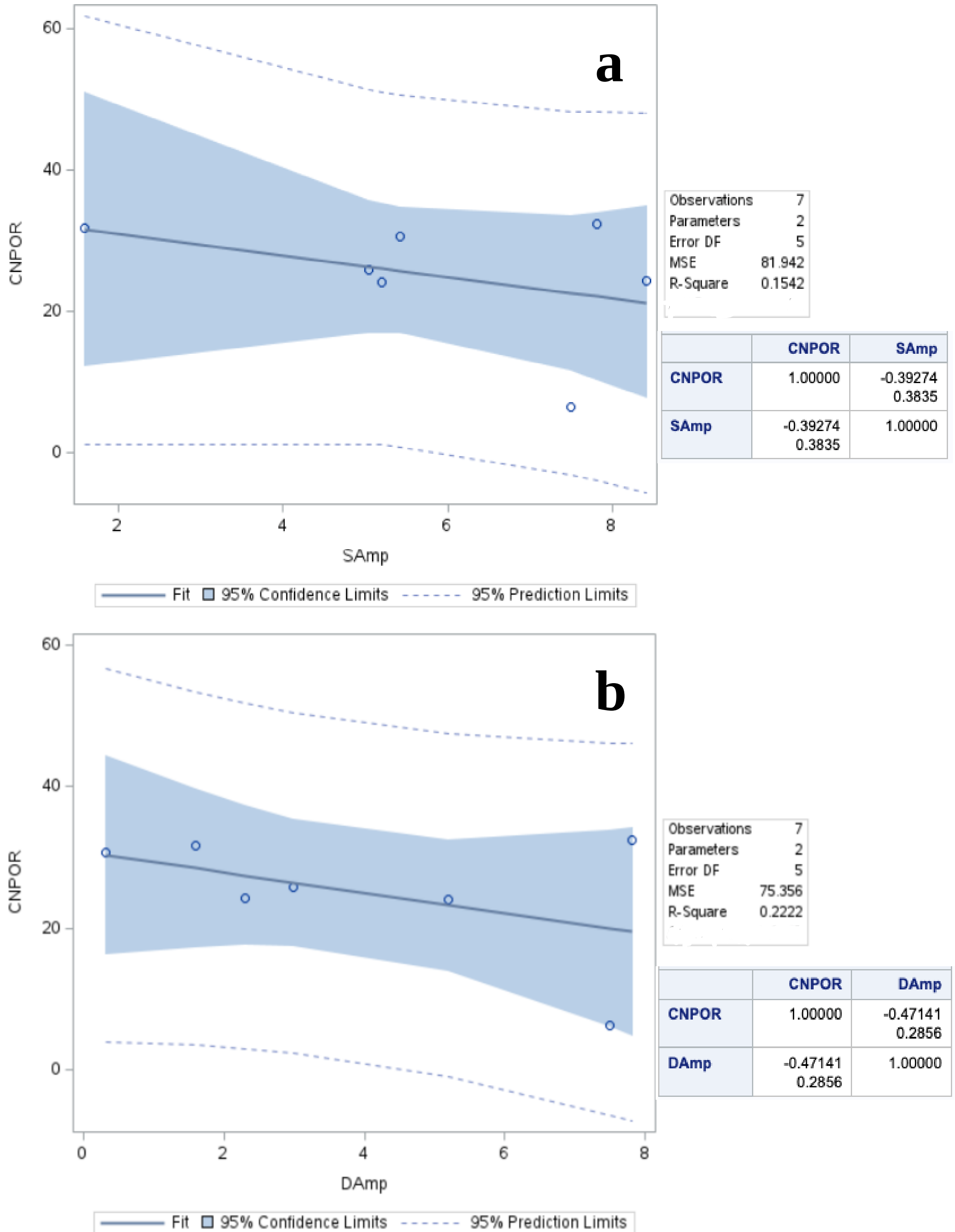

Figure 4.12: Regression analysis of the compensated neutron porosity against the original (a) and detuned (b) seismic amplitude.

Hydrocarbon-producing wells Well S1, S2, S4, S6 & S7 were initially masked by high amplitude anomalies before detuning. Nonproducing wells S5 and S8, initially identified as promising drilling targets due to their structural highs (Fig. 4.15a) and considerable thicknesses (Fig. 4.15d), exhibited high amplitudes even after detuning, indicating that the anomalies are likely geological rather than geometric artifacts. This observation suggests the absence of hydrocarbons in these wells, as high amplitudes are typically associated with limestone and low porosity, which translates to the lack of hydrocarbons within those areas of the Viola.

The instantaneous frequency decreases in zones of decreasing amplitude (Fig. 4.14d), suggesting the presence of hydrocarbon. Taner et al. (1979) observed lower frequencies beneath gas and condensate reservoirs, and Castagna et al. (2003) demonstrated that low-frequency shadows could identify gas reservoirs. Thus, Low instantaneous frequency can be used as a hydrocarbon indicator (Taner, 2001).

In terms of tuning, the instantaneous frequency peaks with thinning as observed in the statistical cross plot (Fig. 4.7). After detuning the instantaneous frequency (Fig. 4.14d), most of the extremely high-frequency values were removed, which suggests that the instantaneous frequency peaks in those areas are due to the thinning of the Viola. This insight is backed by the low thicknesses correlating to those areas in the thickness map (Figs 4.15d).

Areas exhibiting structural highs, high thicknesses, low instantaneous frequencies, and low amplitudes after detuning in the detuned amplitude map (Fig. 4.13 & Fig. 4.14) are particularly prospective for future well placement. These characteristics suggest the presence of geological features that could potentially harbor hydrocarbons. Moreover, the low amplitudes following detuning indicate that these anomalies are not artifacts of geometric effects, further reinforcing their geological significance.

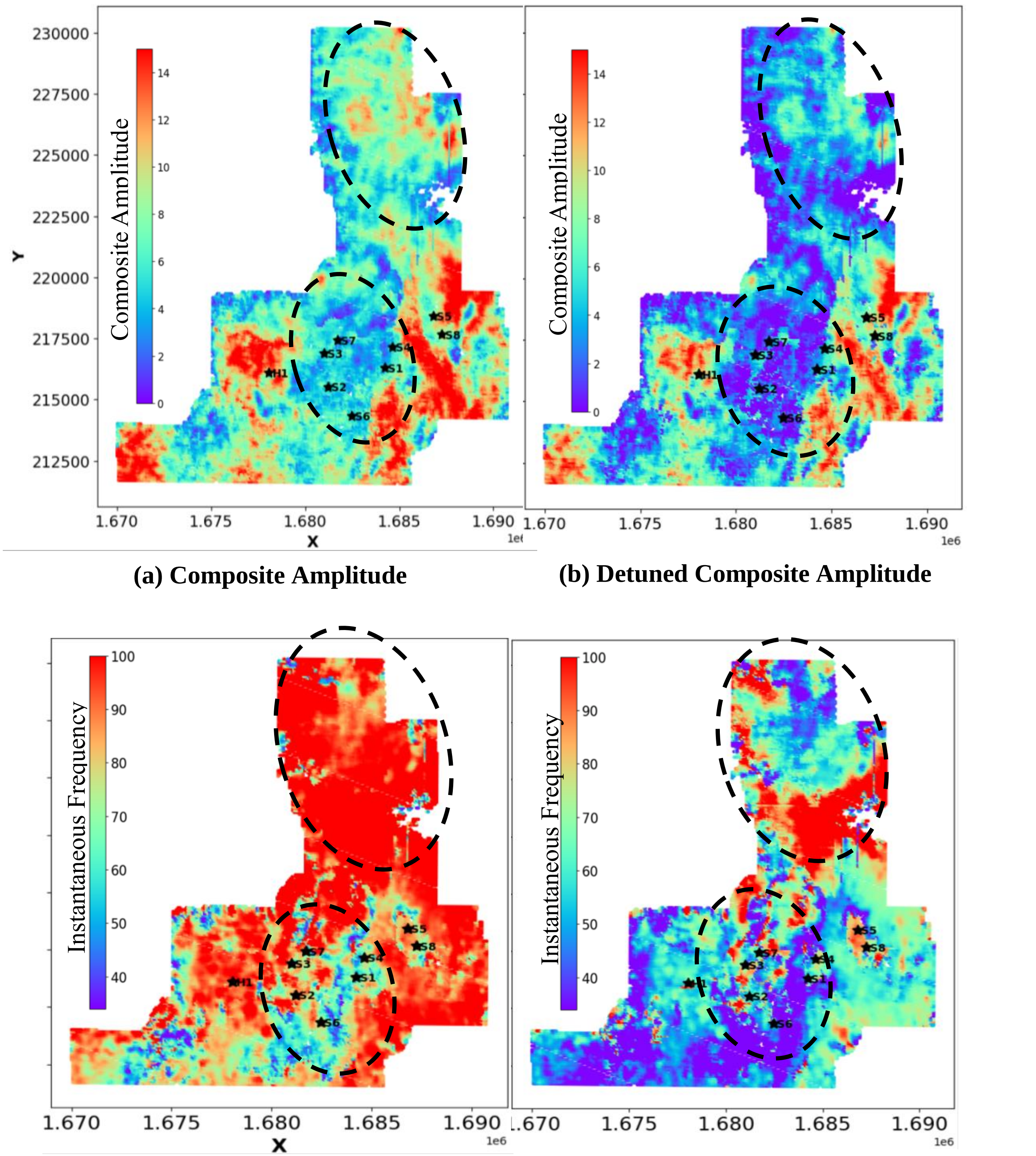

(a) Composite Amplitude (b) Detuned Composite Amplitude

(c) Composite Instantaneous Frequency (d) Detuned Composite Instantaneous Frequency.

Figure 4.13: Shows the original and corrected seismic attributes from the statistical method. Producing wells (black arrows), nonproducing wells (red arrows) and potential drilling zones (green arrows) are highlighted.

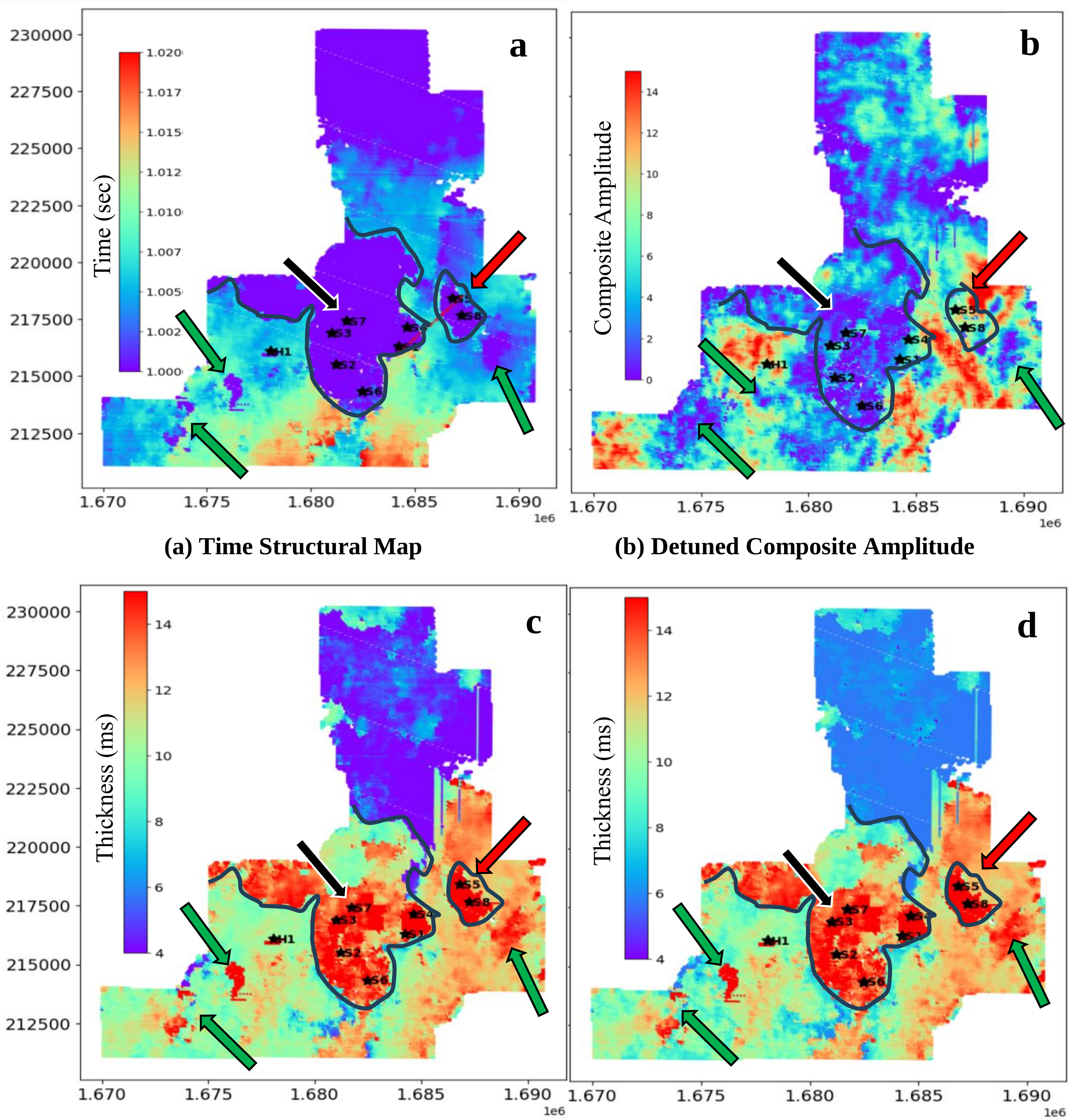

(a) Time Structural Map

(b) Detuned Composite Amplitude

(c) Original Isochrone

(d) Detuned Isochrone

Figure 4.14: Well locations superimposed on the time structural map (a), detuned composite amplitude map (b), Original isochrone map (c), and Detuned isochrone map (d) highlighting the correlation between structural highs, high thicknesses, and well locations originally targeted for drilling. Producing wells (black arrows), nonproducing wells (red arrows) and potential drilling zones (green arrows) are highlighted.

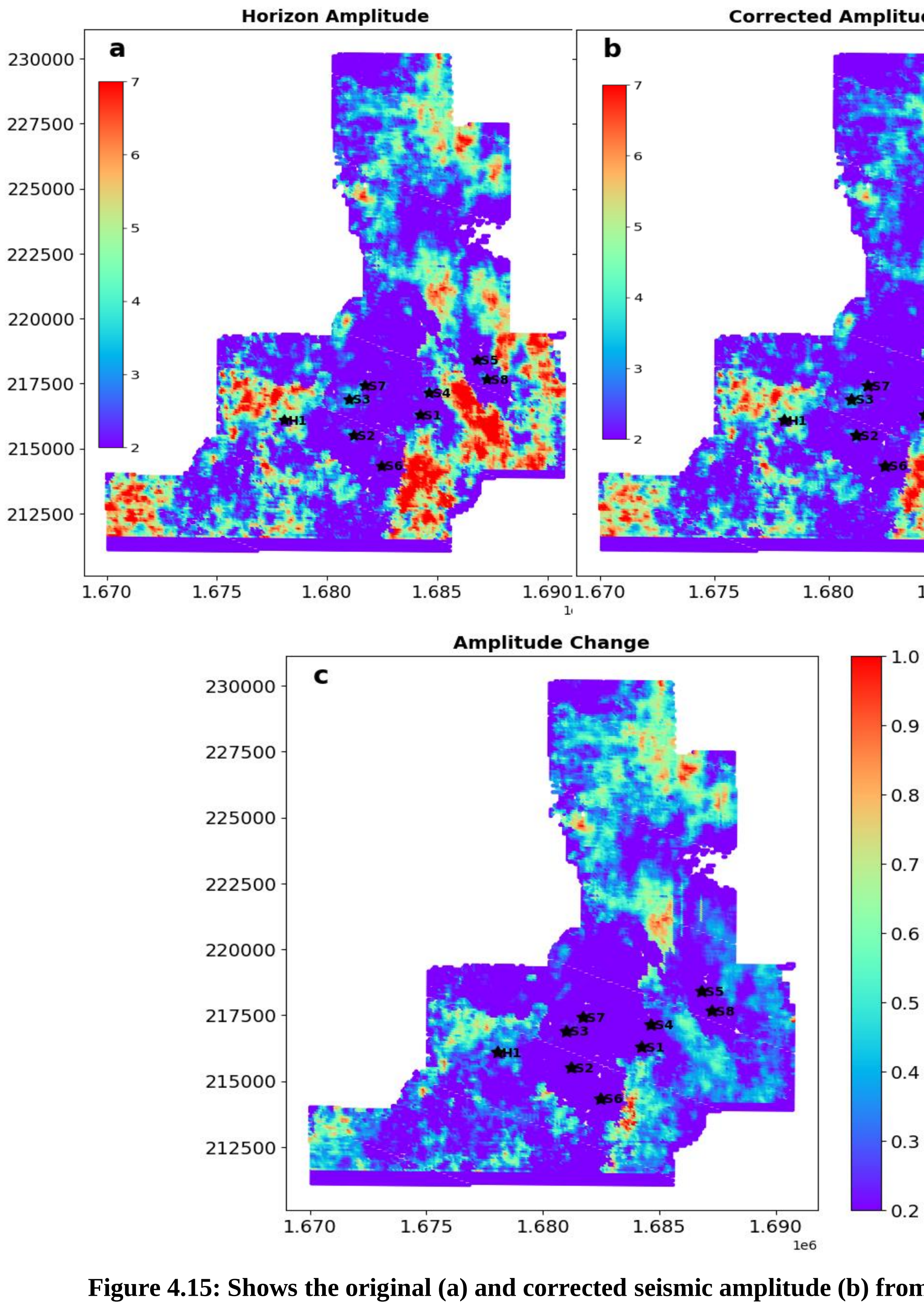

Figure 4.15: Shows the original (a) and corrected seismic amplitude (b) from the deterministic wedge model approach. The maximum tuning error map (c) highlights the amplitude change.

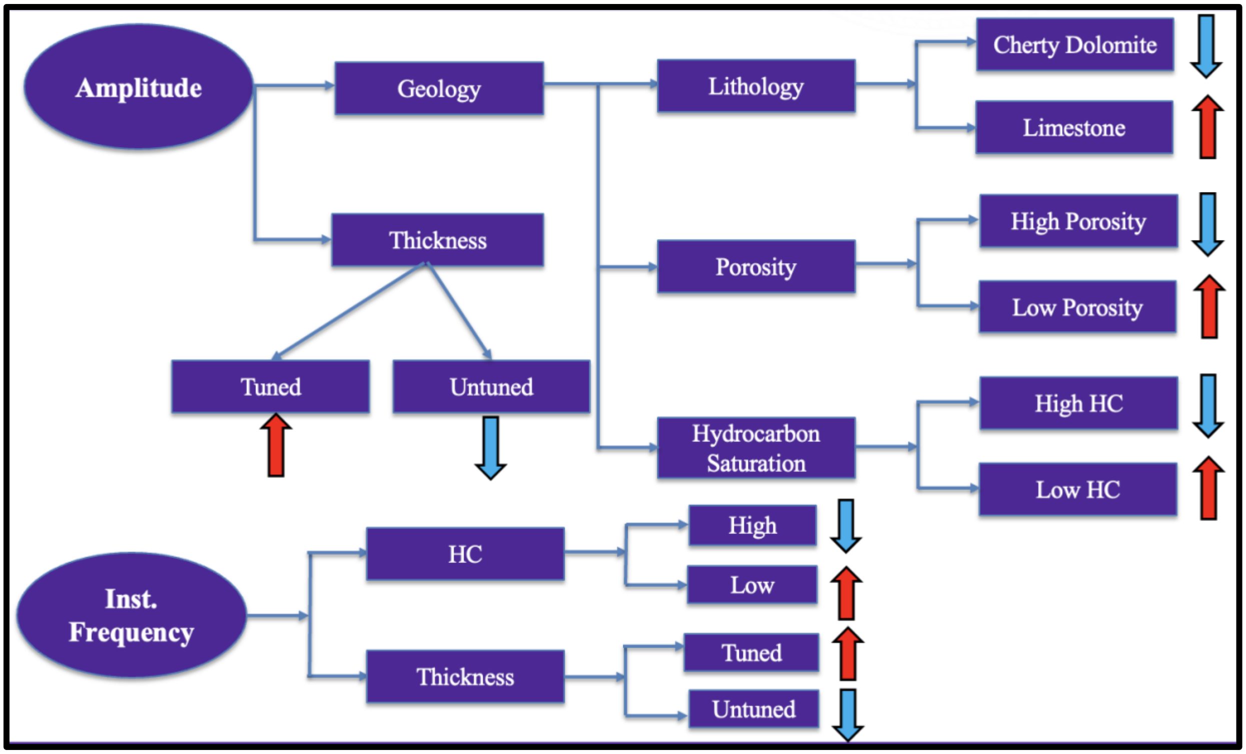

Figure 4.16: Summary of the amplitude and instantaneous frequency responses for the Viola Limestone. Red arrow and blue arrow represent increase and decrease respectively.

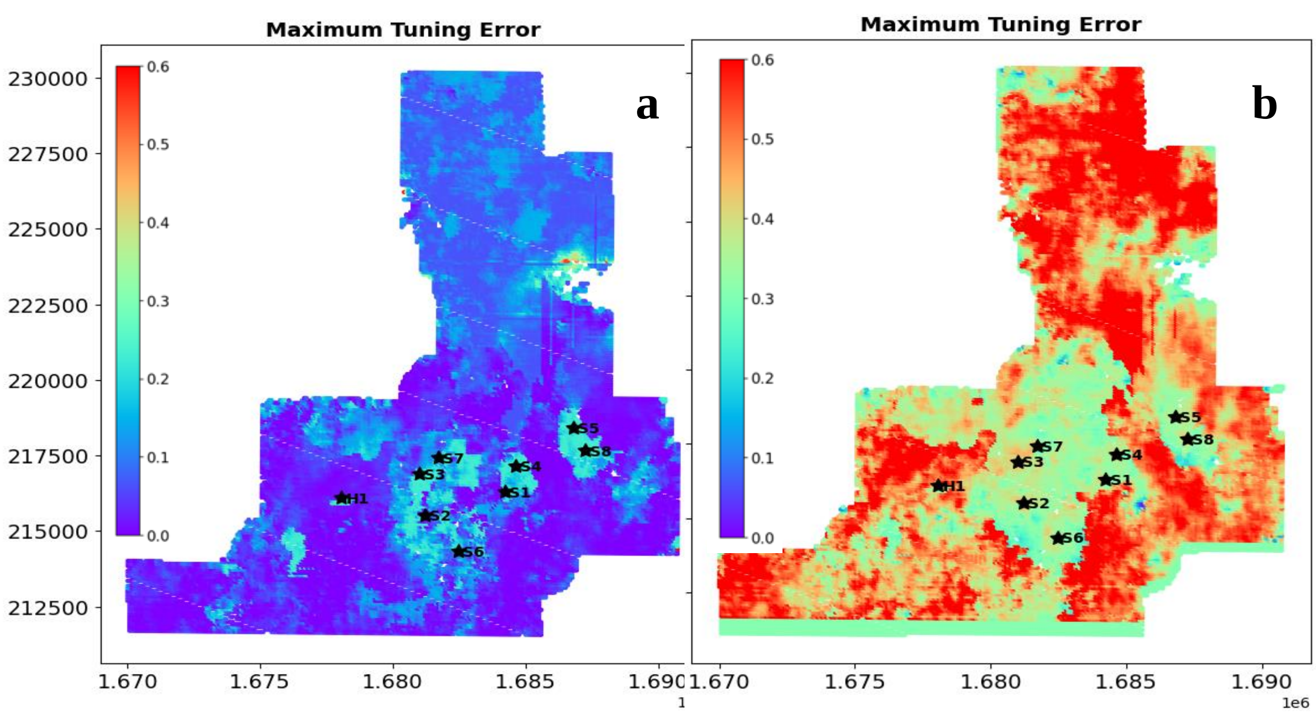

Figure 4.17: Shows the maximum tuning error map of the statistical method (a) the deterministic wedge model method (b)

The seismic response of the amplitudes and instantaneous frequencies of the Viola and their corresponding interpretations are summarized in Figure 4.16 above. Amplitude tuning correction using the wedge model approach (Fig. 4.15) yielded similar results to the statistical method, producing well areas with lower amplitudes. However, the deterministic wedge model method is dependent on the characteristics of the seismic wavelet. Figure 4.17 above compares the estimated maximum tuning error from both methods.

4.7 Maximum Tuning Error Prediction Using Supervised Machine Learning

The Gradient Boosting, Random Forest, and XGBoost models exhibited remarkable performance. The assessment metrics, namely R^2 (coefficient of determination) and MSE (mean square error), provide insights into the accuracy and precision of the models.

Target Label from Statistical Correction

For the Gradient Boosting, R^2 was 0.99, indicating a high level of explained variance, while the MSE was 0.0238, reflecting the average magnitude of prediction errors. The XGBoost model achieved an R^2 of 0.98 and an MSE of 0.129, suggesting a similarly robust performance. Notably, the Random Forest model outperformed both, attaining an impressive R^2 of 0.99 and the lowest MSE of 0.021, highlighting its superior predictive accuracy. These models (Fig. 4.18 & 4.19) were achieved by tweaking parameters (e.g., number of estimators, maximum depth & minimum sample leaf) using *GridSearchCV* and *RandomizedSearchCV* in the sci-kit-learn python library.

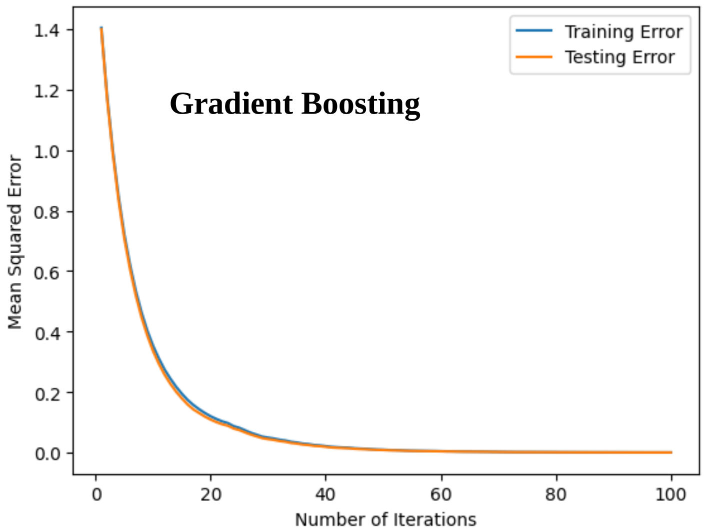

(a) Number of iterations against MSE

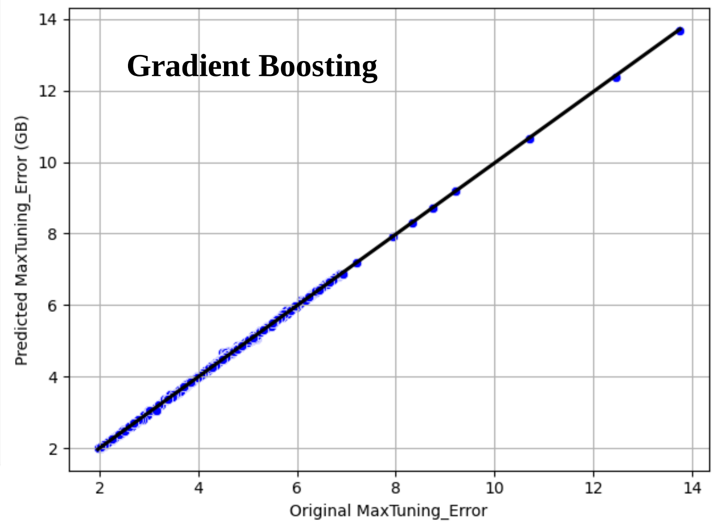

(b) Original vs predicted maximum tuning error

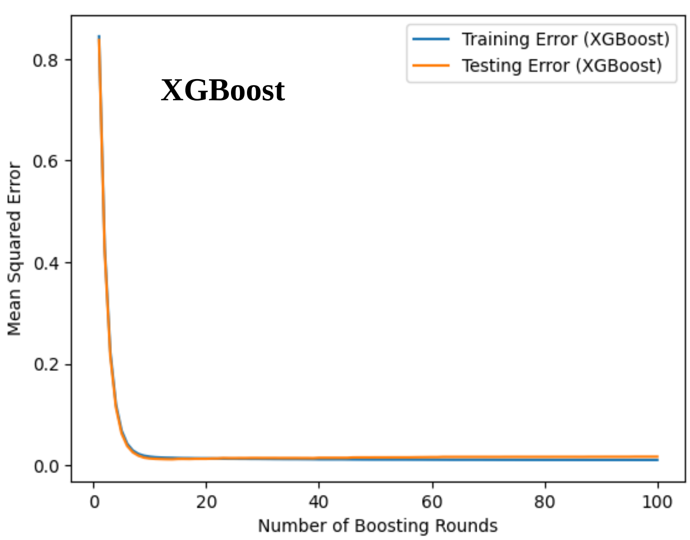

(c) Number of Boosting rounds against MSE

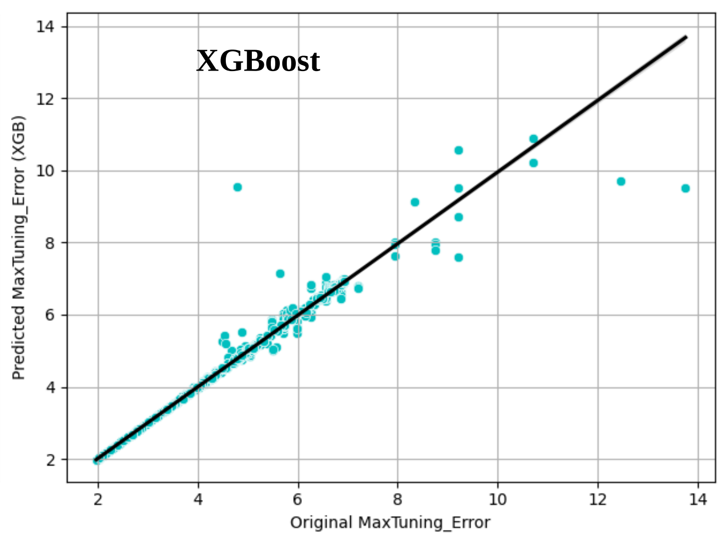

(d) Original vs predicted maximum tuning error

Figure 4.18: Displays the convergence behavior of the models, showcasing how MSE evolves across iterations for training and testing datasets (a & c). crossplots of the target labels (original maximum tuning error) against the predicted maximum tuning error (b & d) visualize the performance of the machine learning algorithms in predicting tuning errors.

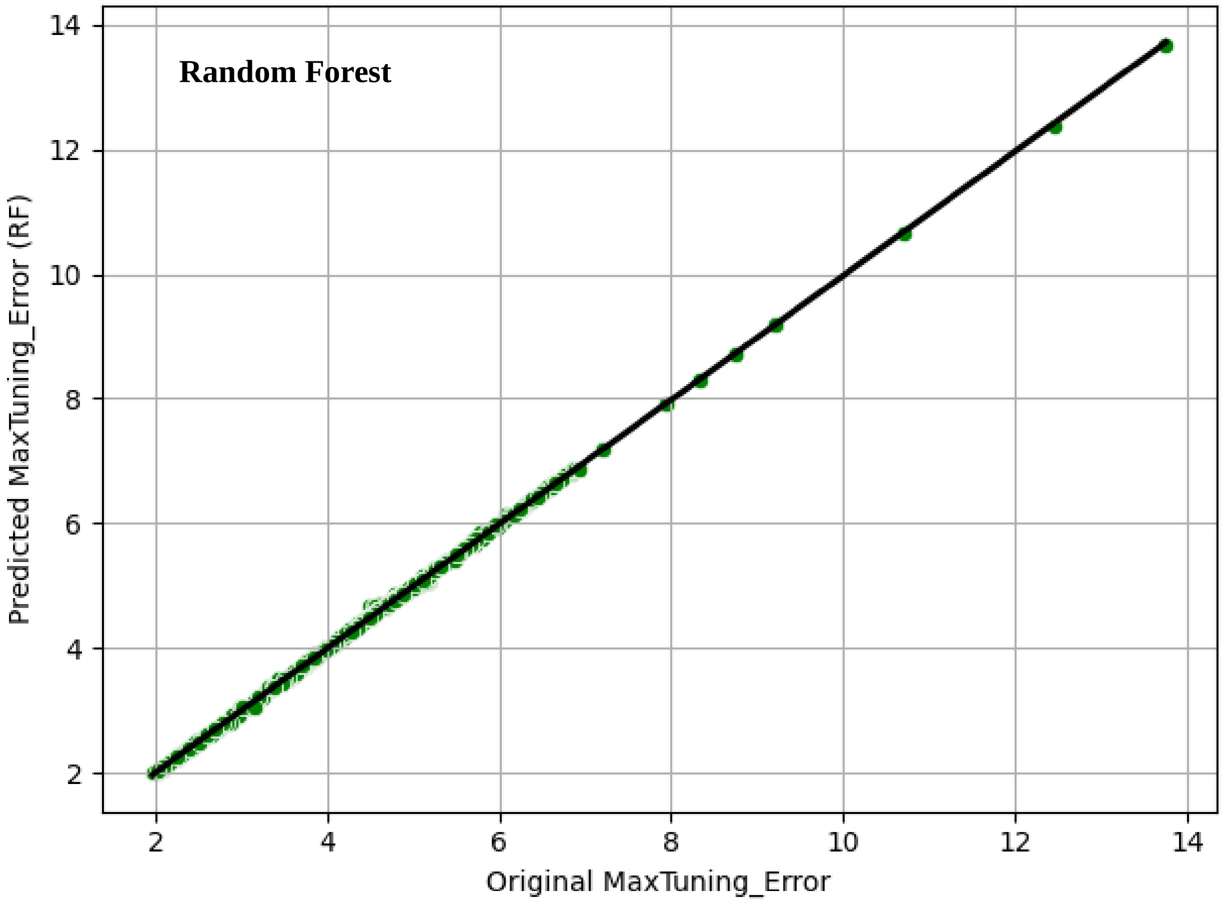

Figure 4.19: Cross-plot of the target labels (original maximum tuning error) against the predicted maximum tuning error visualizes the performance of the Random Forest model in predicting tuning errors.

The inclusion of uncorrected isochrone (thickness) and absolute Viola amplitude as input features during model training highlights the potential of machine learning models to provide accurate results. This is particularly notable in cases where seismic interpreters misidentify suitable reflectors (horizons), as the time thickness is susceptible to tuning effects, potentially leading to overestimation or underestimation. Thus, utilizing these features highlights the models' ability to mitigate interpretive errors and effectively navigate tuning-related problems.

Target Label from Wedge Model Approach Correction

Notably, the three models (Fig. 4.20 & 4.21) performed impressively with an average R^2 of 0.99 and average MSE of 0.004, highlighting its superior predictive accuracy over using target labels from the statistical correction. For the Gradient Boosting, R^2 was 0.99, while the MSE was 0.007. The XGBoost model achieved an R^2 of 0.99 and an MSE of 0.004, suggesting a similarly robust performance. The Random Forest model had the smallest MSE of 0.002 and an R^2 of 0.99. Utilizing the maximum tuning correction from the statistical and wedge model approach as input target labels yielded good predictions of the maximum tuning errors.

However, the difference observed between the two is the feature importance (Fig. 4.22a & 4.23a) for model building. The isochrone (thickness) contribution to the model building for the statistical target label is 99%, while the absolute amplitude contribution makes the remaining 1%. For the wedge model approach target label, the isochrone (thickness) contribution to the model building is 18%, while the absolute amplitude contribution is 82%. This discrepancy can be explained by the difference in the relationship shown by the Spearman correlation (Fig. 4-22b & 4.23b) between the input features for each correction method.

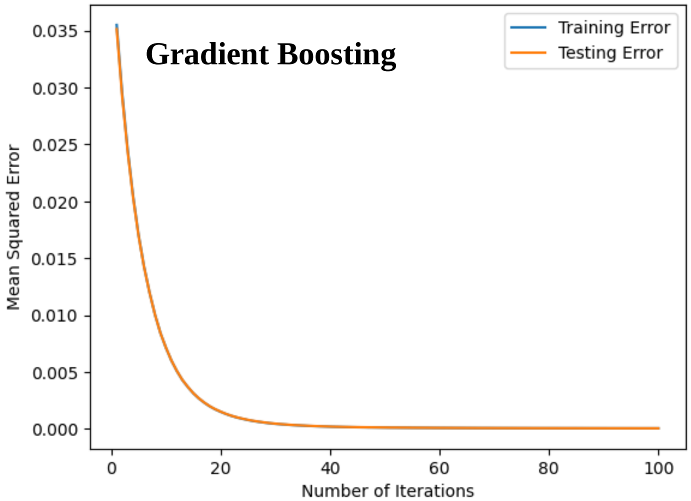

(a) Number of iterations against MSE

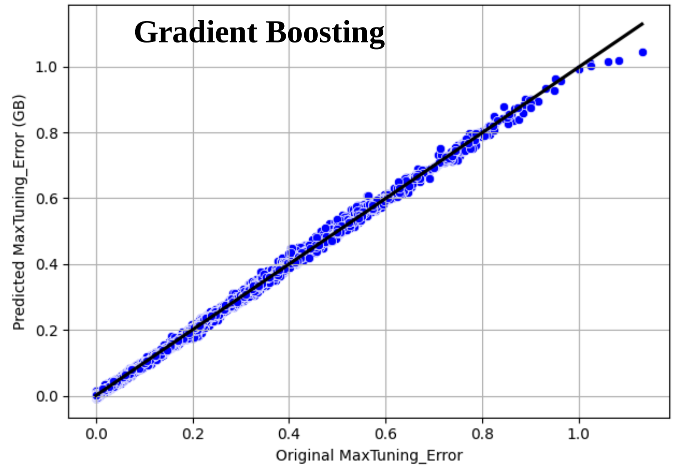

(b) Original vs predicted maximum tuning error

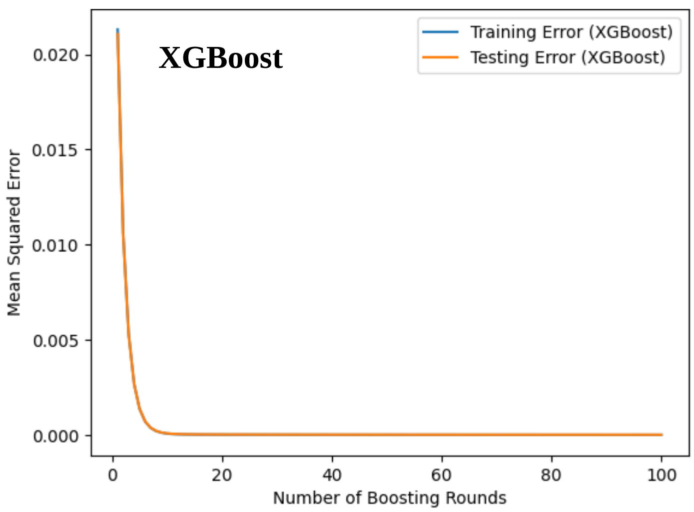

(c) Number of Boosting rounds against MSE

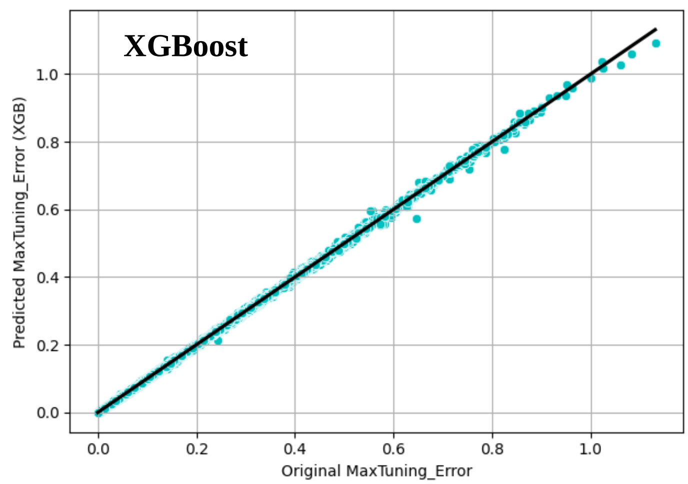

(d) Original vs predicted maximum tuning error

Figure 4.20: Displays the convergence behavior of the models, showcasing how MSE evolves across iterations for training and testing datasets (a & c). crossplots of the target labels (original maximum tuning error) against the predicted maximum tuning error (b & d) visualize the performance of the machine learning algorithms in predicting tuning errors.

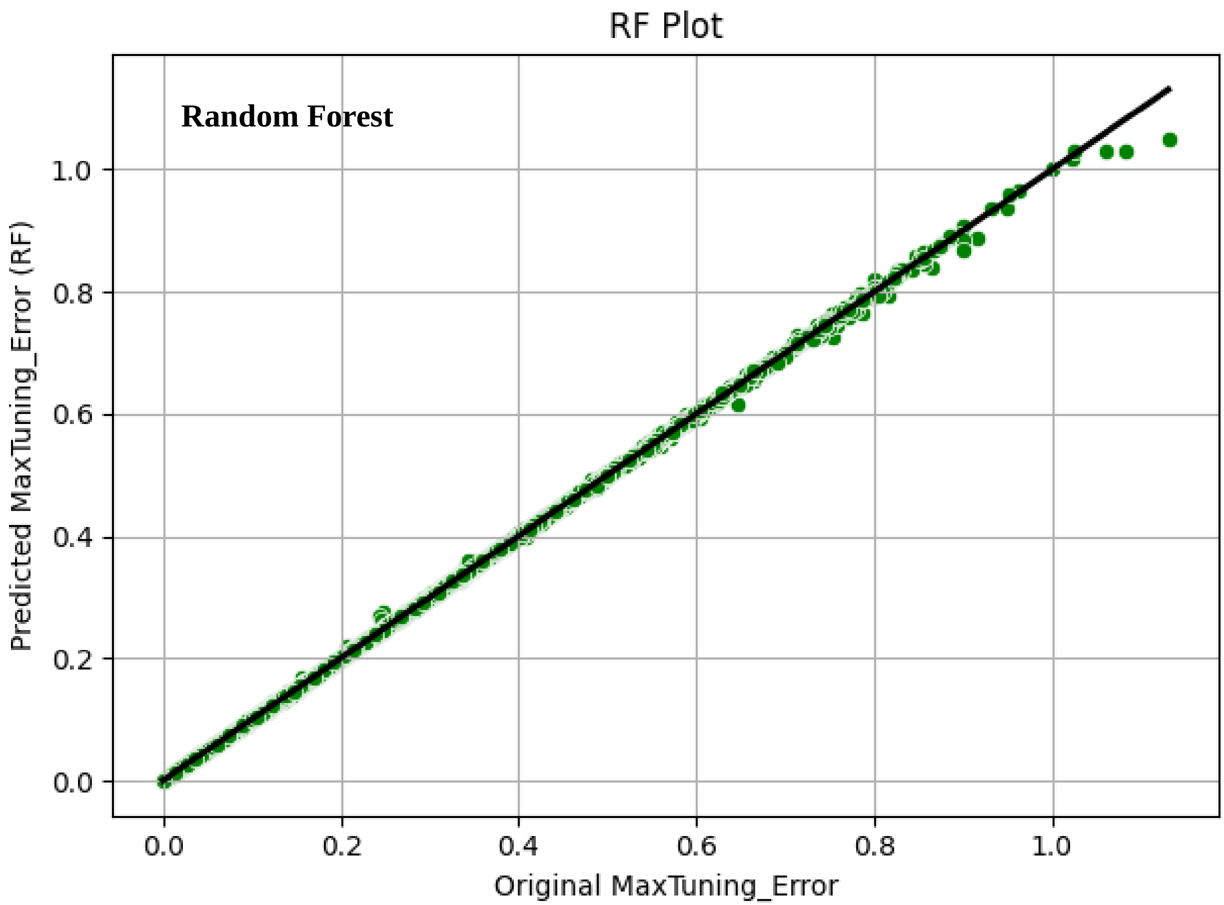

Figure 4.21: Cross-plot of the target labels (original maximum tuning error) against the predicted maximum tuning error visualizes the performance of the Random Forest model in predicting tuning errors.

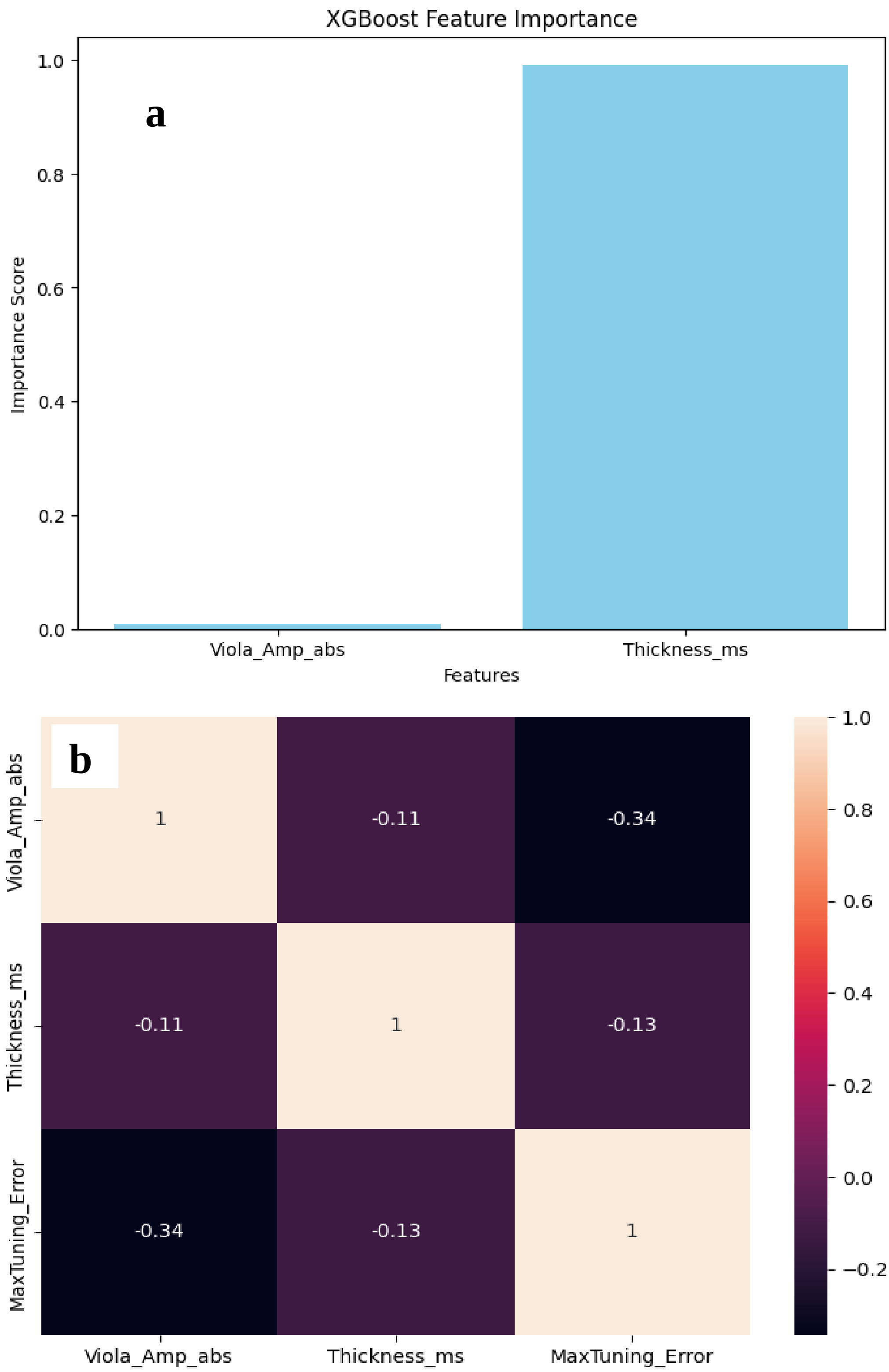

Figure 4.22: Feature importance score (a) and the Spearman correlation (b) between input features from the statistical correction approach.

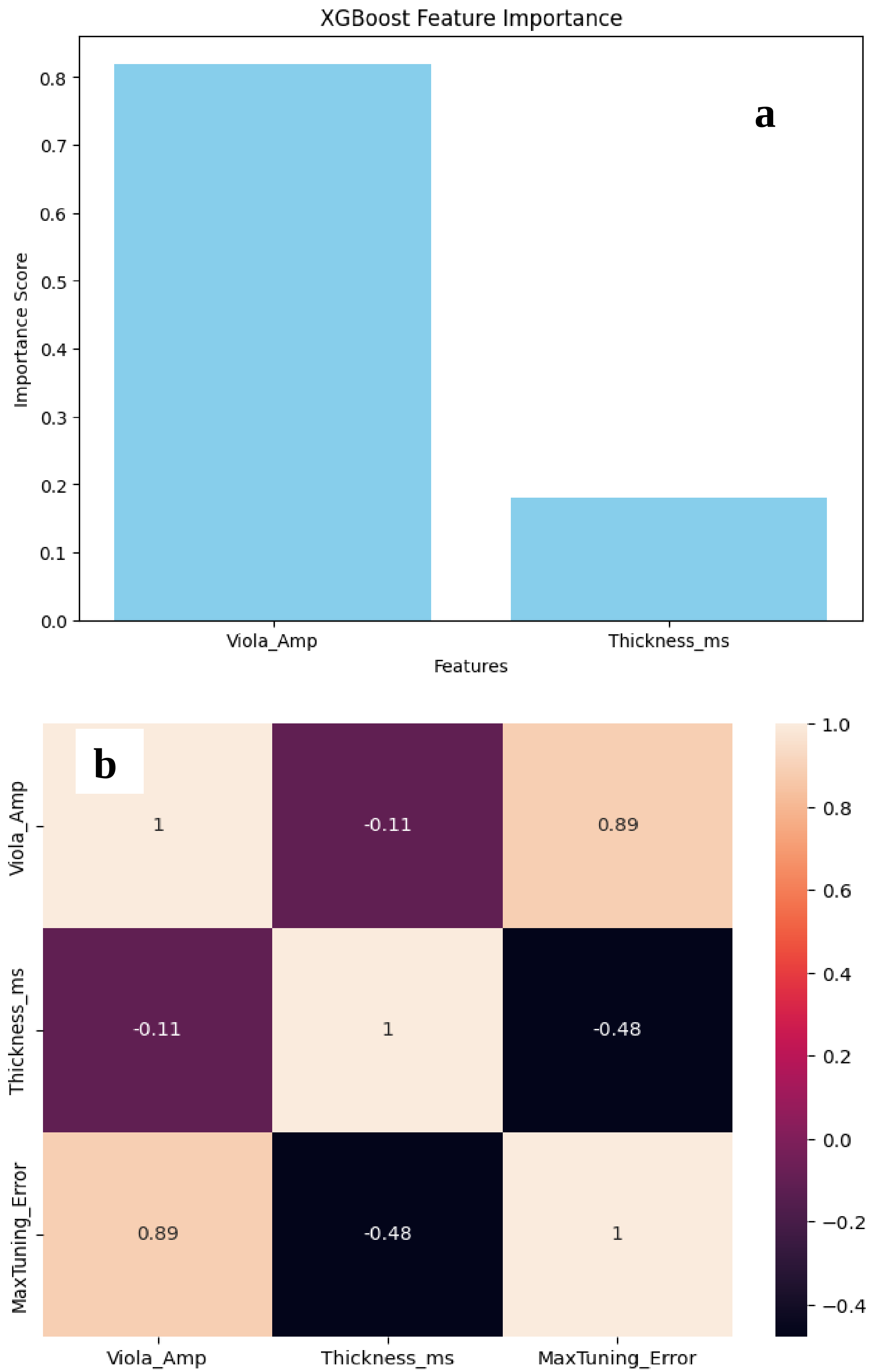

Figure 4.23: Feature importance score (a) and the Spearman correlation (b) between input features from the wedge model correction approach.

Chapter 5 - Conclusion

The maximum tuning error, calculated as the difference between the peak amplitude value of the statistical tuning curve and the corresponding baseline, L4, value, is 41.6% of the corresponding composite amplitude baseline value. The calculated 41.6% maximum tuning contribution agrees with the rule-of-thumb of an expected 40% maximum increase due to tuning, Brown 1991. This gives rise to increased credibility in the estimated tuning corrections. The tuning thickness calculated from the deterministic equation ($^{b}/_{2}$) is also consistent with the tuning thickness obtained from the tuning curve, which is about 6ms.

The analysis of detuned seismic attributes reveals promising areas for future well placement. Areas characterized by structural highs, substantial thicknesses, low instantaneous frequency, and persistently low amplitudes after detuning hold significant potential for hydrocarbon production. The correlation between lower seismic amplitudes and prolific hydrocarbon saturations and the association between higher amplitudes and non-productive wells supports this observation.

Furthermore, vuggy porosity and hydrocarbon within the Viola, characterized by lower acoustic impedance, can contribute to weaker seismic reflections and lower amplitudes. This further demonstrates the geological significance of these anomalies and the preservation of geological features through detuning. Therefore, these areas warrant further investigation and exploration of potential hydrocarbon wells.

Initially, a weak correlation existed between seismic amplitude and the underlying geology due to thickness effects. However, our tuning correction method successfully mitigated these effects, leading to a significantly improved correlation, as evidenced by increased R-squared values. This robust method, applicable across diverse seismic attributes and geological settings, paves the way for more reliable reservoir characterization and improved geological interpretation from seismic data. This knowledge can be transferred to siliciclastic reservoirs.

Gradient boosting, Random Forest, and XGBoost models have shown to be the best algorithms for predicting maximum tuning errors. This study highlights the power of machine learning models in predicting tuning errors accurately while mitigating interpretive errors arising from horizon tracking.

References

Attribute. (2015). Retrieved from Schlumberger Oil Filed Dictionary: https://glossary.slb.com/terms/a/attribute

Ball, M. M., Mitchell, E. H., & Sherwood, E. F. (1991). Petroleum geology of the Anadarko Basin region, Province (115), kansas, Oklahoma, and Texas. *U.S Geological Survey*.

Bornemann, E., & Doveton, J. H. (1983). Lithofacies Mapping of Viola Limestone in South-Central Kansas, Based on Wireline Logs. *The American Association of Petroleum Geologists Bulletin*, 609-623.

Breiman, L. (2001). Random Forests. *Machine Learning*, 5-32.

Brown, A. R. (1996). Seismic atttibutes and their classification. *Leading Edge*, 15, 1090.

Brown, A. R. (1999). *Interpretation of Three-Dimensional Seismic Data.* Tulsa, Oklahoma: The American Association of Petroleum Geologists and the Society of Exploration Geophysicists.

Brown, A. R. (2011). Structural Interpretation. In *Interpretation of Three-Dimensional Seismic Data* (pp. 61-102). Society of Exploration Geophysicists and American Association of Petroleum Geologists.

Castagna, J. P., S, S., & Siegfried, R. W. (2003). Instantaneous spectral analysis: Detection of low-frequency shadows associated with hydrocarbons. *The Leading Edge*, 22, 120-127.

Chen, T., & Guestrin, C. (2016). XGBoost. *Proceedings of the 22nd ACM SIGKDD International Conference on Knowledge Discovery and Data Mining* (pp. 785-794). New York, NY, USA: ACM.

Chopra. (2005). Seismic attributes - A historical perspective. *Geophysics*.

Chopra, S., & Marfurt, K. J. (2005). Seismic Attributes - A Historical Perspective. *Geophysics*, 3-28.

Chopra, S., & Marfurt, K. J. (2008). Emerging and futures trends in seismic attributes. *The Leading Edge*, Vol. 27, no. 3, p. 298-318.

Clark County--Oil and Gas Production. (2014). Retrieved from Kansas Geological Survey: http://www.kgs.ku.edu/PRS/County/abc/clark.html

Cole, V. B. (1975). Subsurface Ordovician-Cambrian Rocks in Kansas. *Kansas Geological Survey, Subsurface Geology Series 2*.

Doveton. (2017). *Mineral Composition Profiles*. Retrieved from Kansas Geological Survey: http://www.kgs.ku.edu/Publications/Bulletins/LA/12_profiles.html

Faleide, Thea Sveva; Midtkandal, Ivar; Planke, Sverre; Corseri, Romain; Faleide, Jan Inge; Serck, Cristopher Sæbø; Nystuen, Johan Petter;. (2019). Characterisation and development of Early Cretaceous shelf platform deposition and faulting in the Hoop area, southwestern Barents Sea—constrained by high-resolution seismic data. *Norwegian Journal of Geology*.

Franseen, E. K., Byrnes, A. P., Cansler, J. R., Steinhauff, D. M., & Carr, T. R. (2004). The Geology of Kansas Historical Aspects of Arbuckle. *Kansas Geological Survey Earth Sciences Bulletin*, 250(part 2) 1-43.

Friedman, J. H. (2001). Greedy Function Approximation: A Gradient Boosting Machine. *The Annals of Statistics*, 1189-1232.

Gradient Boosting in ML. (2023). Retrieved from geeksforgeeks: https://www.geeksforgeeks.org/ml-gradient-boosting/

Hagood. (2019). *Detailed Core and Log Analysis of a Producing Viola Dolomite Well in Comanche County, Kansas.* Manhattan: Kansas State University.

Heron. (2011). Resolution. *Society of Exploration Geophysicists* , 75-82.

Kallweit, R. S., & Wood, L. C. (1982). The limits of resolution of zero-phase wavelets. *Geophysics*, 1035-1046.

Kallweit, R. S., & Wood, L. C. (1982). The limits of resolution of zero-phase wavelets. *Geophysics 47*, 1035-1046.

Kalyani, P; Manasa, Y; Ahammad, Hasane Sk; Suman, M; Anwer, Mohammed Kak Twana; Hossain, Md Ahmad; Rashed, Ahmed Nabih Zaki;. (2019). Prediction of patient's neurological recovery from cervical spinal cord injury through XGBoost learning approach. *European Spine Journal*, 2140-2148.

Meckel, L. D., & Nath, A. K. (1977). Geologic Considerations for Stratigraphic Modeling and Interpretation.

Raef, A., Totten, M., Linaries, A., & Kamari, A. (2019). Lithofacies Control on Reservoir Quality of the Viola Limestone in Southwest Kansas and Unsupervised Machine Learning Aproach of Seismic Attributes Facies-Classification. *Pure and Applied Geophysics*, 176(2019), 4297-4308.

Ralph, W. K., & Neil, L. A. (1995). Comparision of High-resolution and Conventional-resolution Seismic Data-- Application to Cyclothems. *Kansas Geological Survey*.

Random Forest Regression in Python. (2023). Retrieved from geeksforgeeks: https://www.geeksforgeeks.org/random-forest-regression-in-python/

Richardson, L. J. (2013). The Herd Viola trend, Comanche County, Kansas. *AAPG Search and Discovery*, #20220.

Ricker, N. (1953). Wavelet Contraction, Wavelet Expansion, and the Control of Seismic Resolution. *Geophysics*, 769-792.

Roden, Rocky; Smith, Thomas A; Santogrossi, Patricia; Sacrey, Deborah; Jones, Gary. (2017). Seismic interpretation below tuning with multiattribute analysis. *The Leading Edge*, 330-339.

Satinder, C., & Kurt, M. J. (2007). *Seismic Attributes for Prospect Identification and Reservoir Characterization.* Society of Exploration Geophysicists.

Schoenberger, M., & Levin, F. K. (1978). Apparent attenuation due to intrabed multiples. *Geophysics*, 43, 730-737.

Sheriff, Robert E; Geldart, Lloyd P. (1995). *Exploration Seismology.* Cambridge University Press.

Taner, M. T., Koehler, F., & Sheriff, R. E. (1979). Complex seismic trace analysis. *Geophysics*, 1041-1063.

Taner, T. M. (2001). Seismic Attributes. *Canadian Society of Exploration Geophysicists*, vol. 26 .

Tianci, C., & Gary, M. F. (2014). Seismic wavelet estimation. *CREWES Research Report*.

Van Ornam, Z. W. (2020). *Understanding the compound seismic signature of CO2 injection in a thin carbonate reservoir during enhanced oil recovery.* Manhattan: Kansas State University.

Victor, C., & Abdelmoneam, R. (2020). *A rock physics modeling approach in analysis and integration of well logs and ultrasonic velocities for characterizing the reservoir facies of the Viola Limestone in southwestern Kansas.* Manhattan: Kansas State University.

Widess, M. B. (1973). How Thin is a Thin Bed. *Geophysics*, 1176-1180.

Zhao, T., Jayaram, V., Roy, A., & Marfurt, K. J. (2015). A comparision of classification techniques for seismic facies recognition. *Interpretation, 3(4), SAE29-SAE58*, https://doi.org/10.1190/INT-2015-0044.1.

Appendix A - Extracted Seismic Attributes

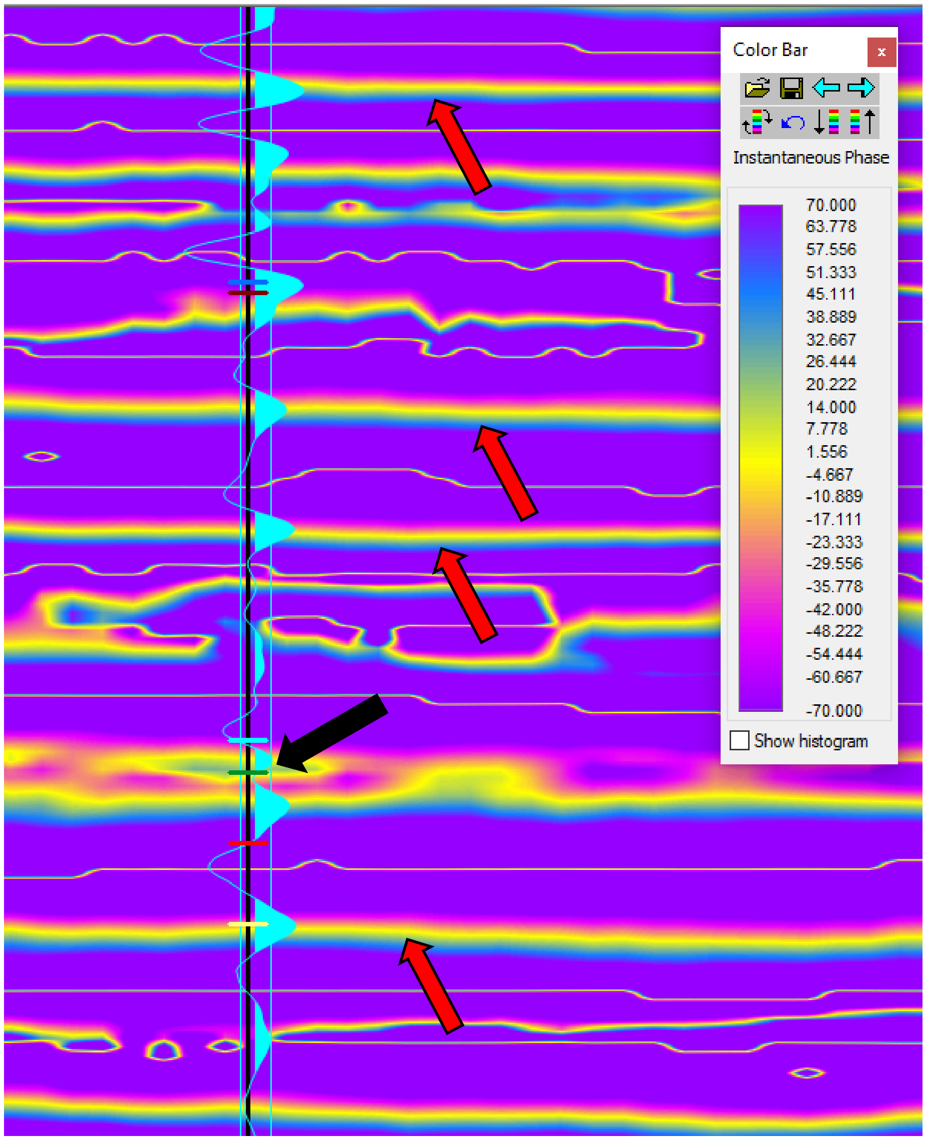

Figure A. 1: Instantaneous phase attribute as an indicator of lateral continuity. It highlights detailed visualization of stratigraphic elements as consistent and continuous events (red arrows). The black arrow shows the Viola peak, and the phase angles are represented by the color bar to the right.

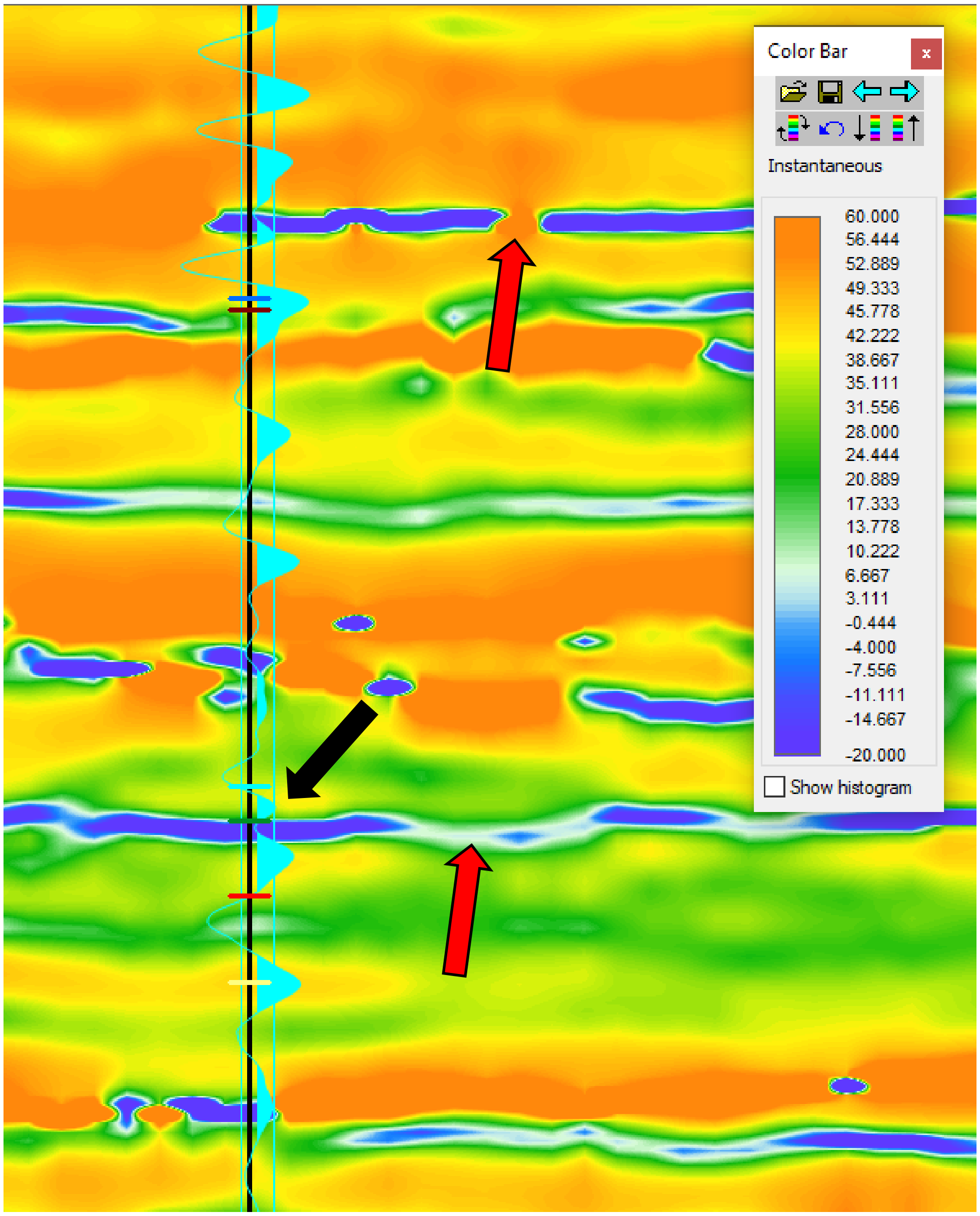

Figure A. 2: Instantaneous frequency as a thin bed indicator. It highlights locations (onset of tuning) where instantaneous frequencies jump or exhibit a negative sign caused by closely-arriving reflected wavelets (red arrows). The black arrow shows the Viola peak, and the frequency values are represented by the color bar to the right.

Appendix B - RHOmaa-Umaa Cross-plots

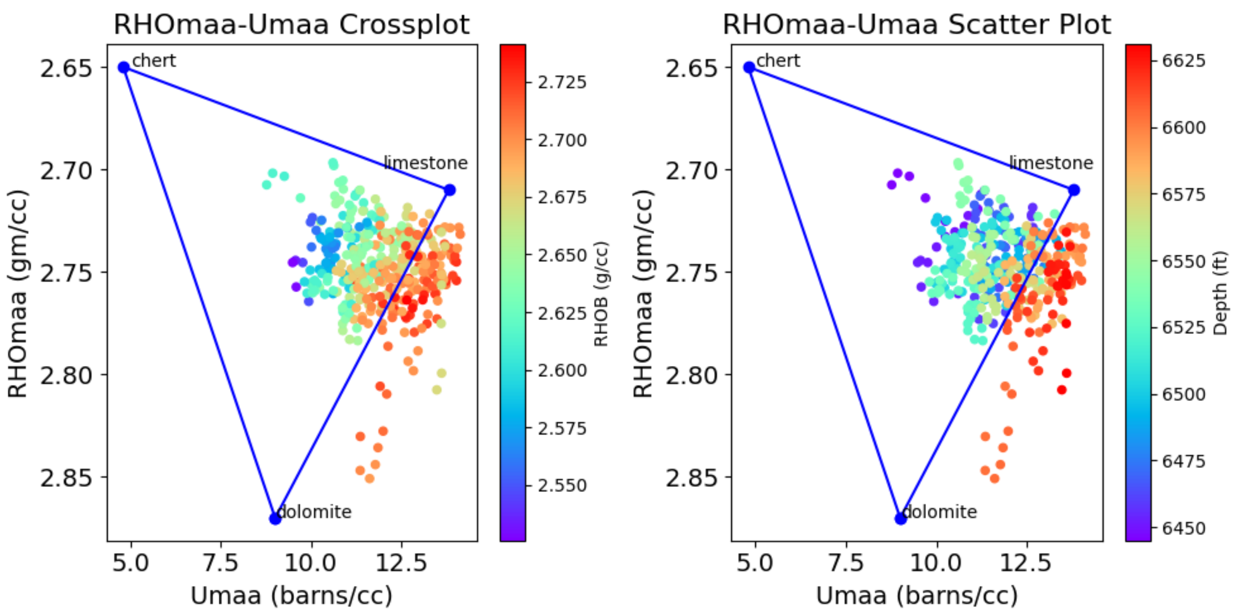

Figure B. 1: RHOmaa-Umaa cross-plot of Hardens1.

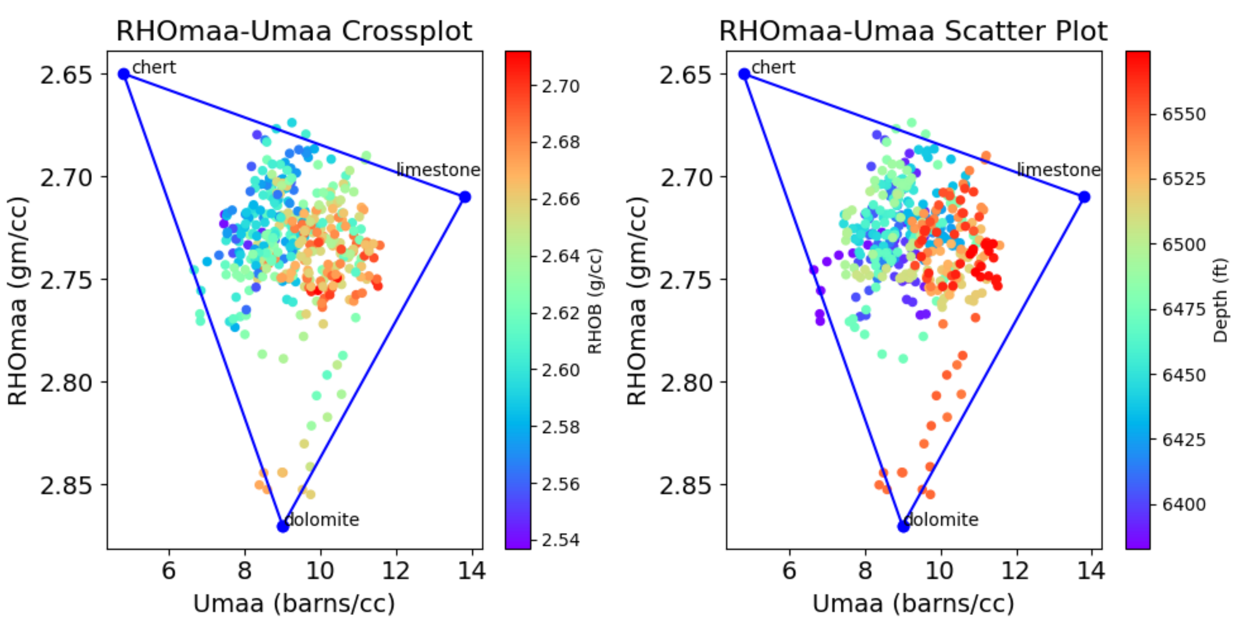

Figure B. 2: RHOmaa-Umaa cross-plot of Stephens1.

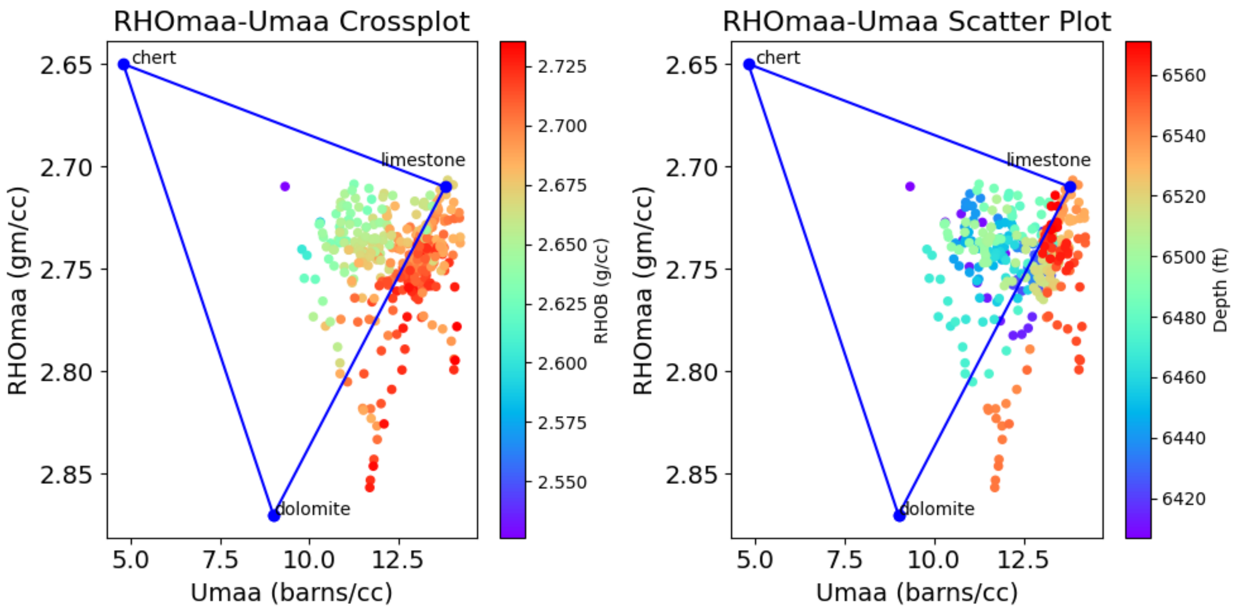

Figure B. 3: RHOmaa-Umaa cross-plot of Stephens3.

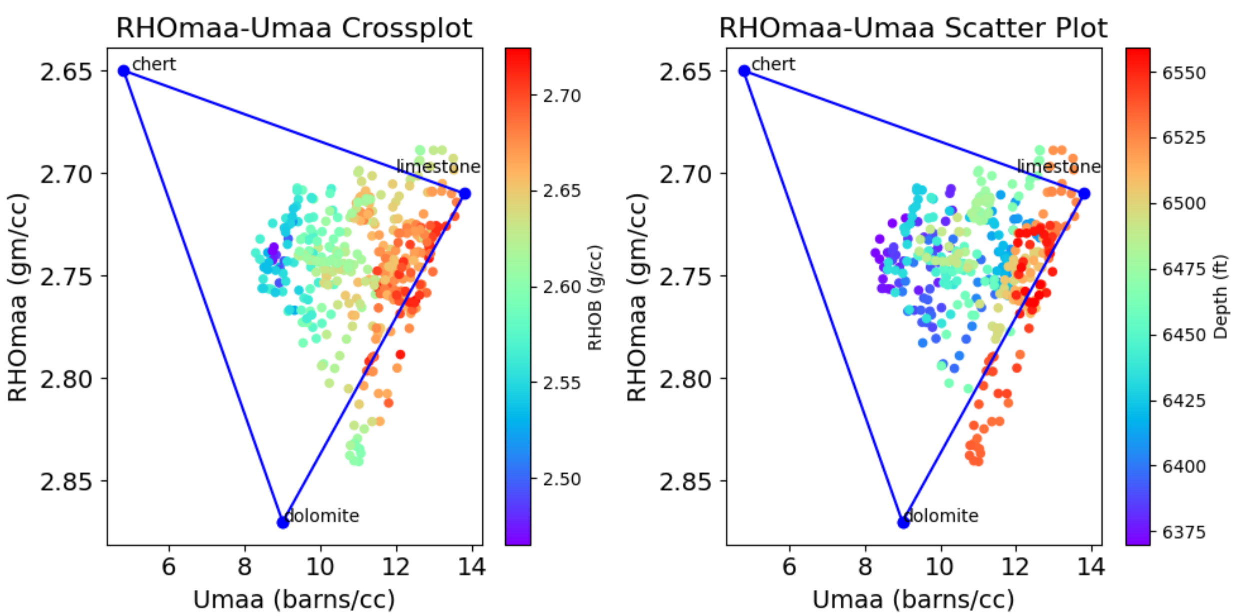

Figure B. 4: RHOmaa-Umaa cross-plot of Stephens4.

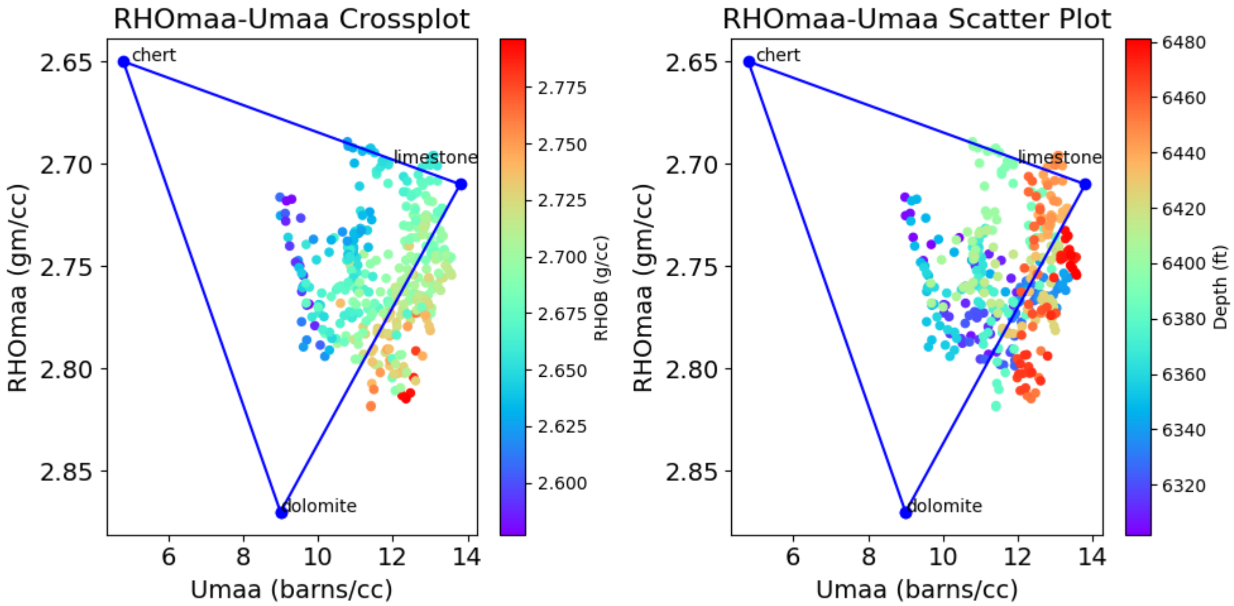

Figure B. 5: RHOmaa-Umaa cross-plot of Stephens5.

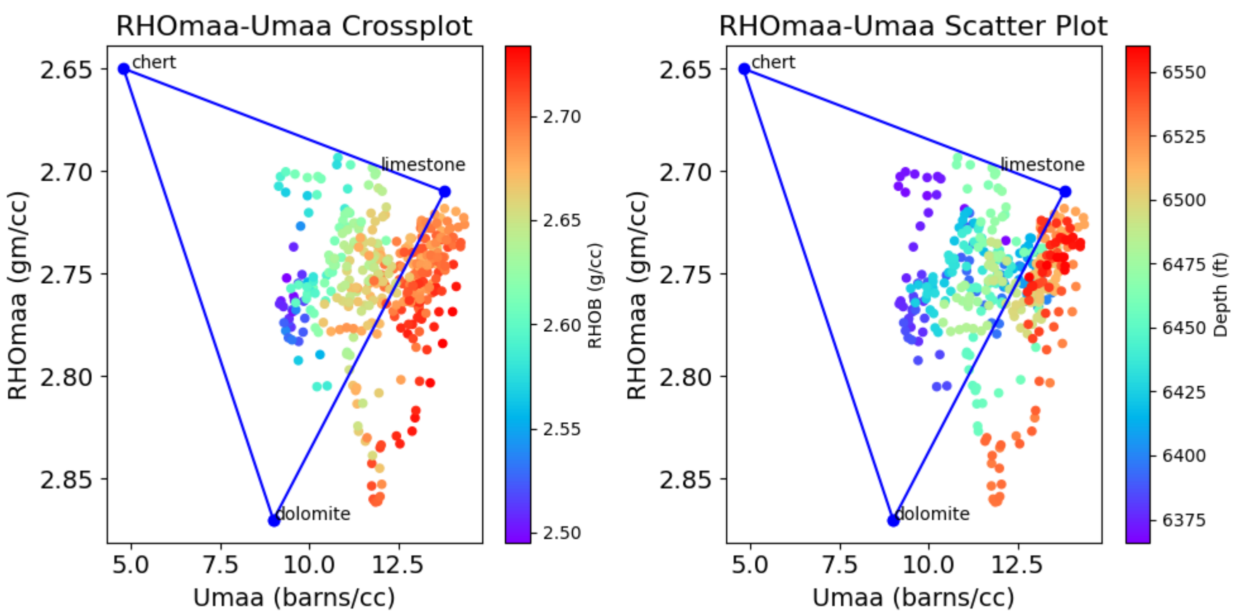

Figure B. 6: RHOmaa-Umaa cross-plot of Stephens7.

Appendix C - Synthetic wedge models

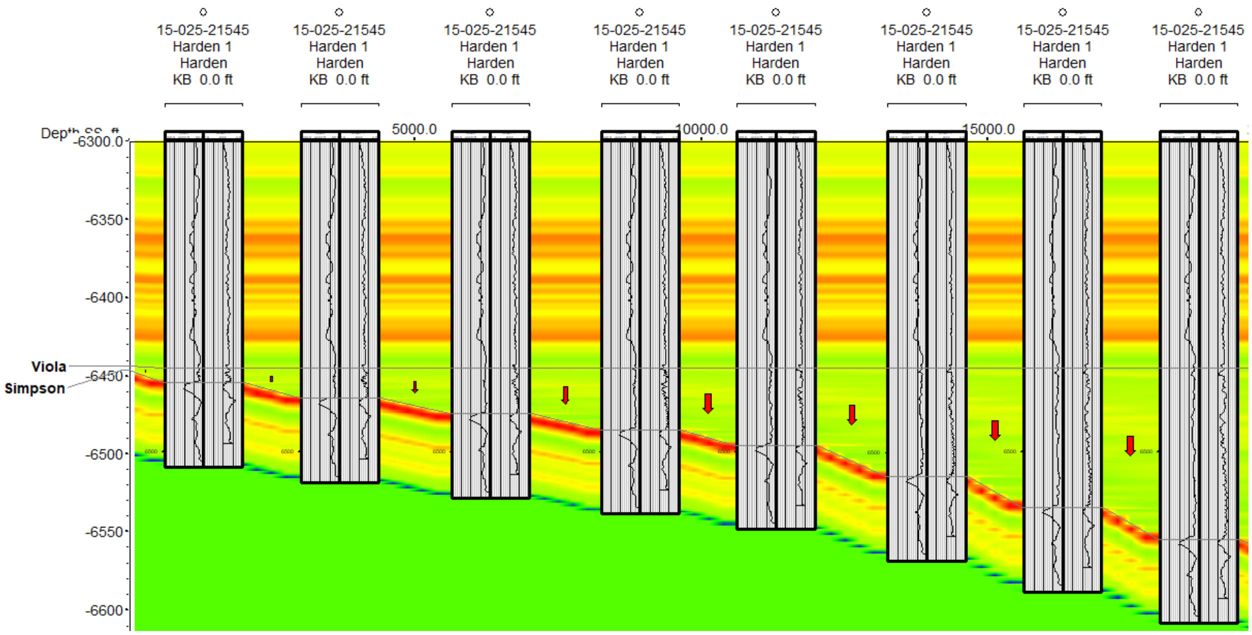

Figure C. 1: Wedge model configuration. Wells are duplicated to keep geology (velocity and density) constant while the thickness of the viola is varied.

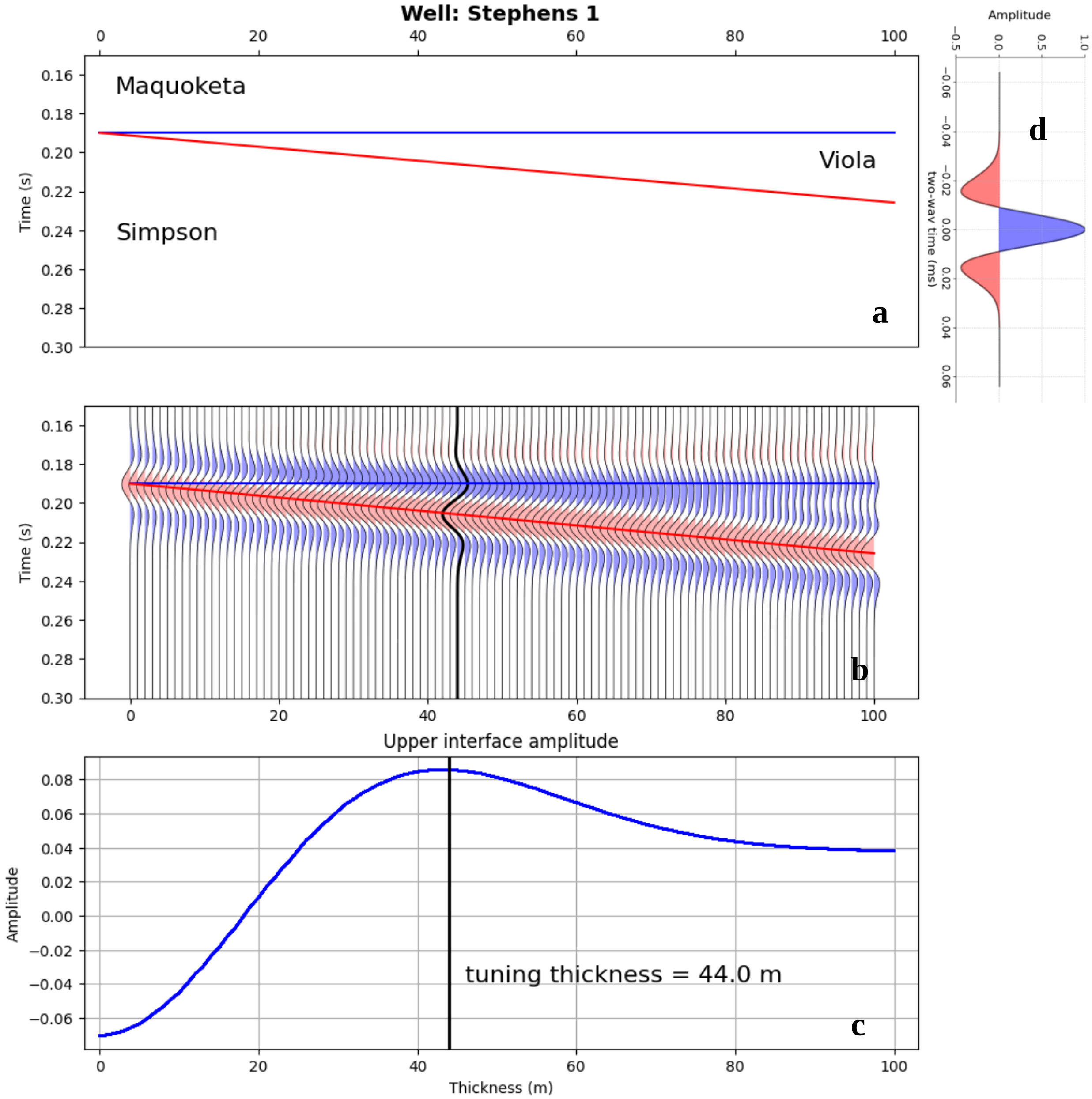

Figure C. 2: (a) A three-layer wedge model. (b) The constructive interference between the side lobes and main reflections produces brighter reflections, as seen in the zero-offset synthetic seismogram displayed in normal polarity. (c) The amplitude of the synthetic extracted along the top of the Viola reservoir. (d)The convolved Ricker wavelet of 25Hz.